HEAT TRANSFER CHARACTERISTICS OF A TWO-PASS

TRAPEZOIDAL CHANNEL AND A NOVEL HEAT PIPE

A Dissertation

by

SANG WON LEE

Submitted to the Office of Graduate Studies of
Texas A&M University
in partial fulfillment of the requirements for the degree of

DOCTOR OF PHILOSOPHY

August 2007

Major Subject: Mechanical Engineering

HEAT TRANSFER CHARACTERISTICS OF A TWO-PASS

TRAPEZOIDAL CHANNEL AND A NOVEL HEAT PIPE

A Dissertation

by

SANG WON LEE

Submitted to the Office of Graduate Studies of
Texas A&M University
in partial fulfillment of the requirements for the degree of

DOCTOR OF PHILOSOPHY

Approved by:

Co-Chairs of Committee,	S.C. Lau
	Ed Marotta
Committee Members,	J.C. Han
	N.K. Anand
	Y.A. Hassan
Head of Department,	Dennis O'Neal

August 2007

Major Subject: Mechanical Engineering

ABSTRACT

Heat Transfer Characteristics of a Two-pass Trapezoidal Channel

and a Novel Heat Pipe. (August 2007)

Sang Won Lee, B.En., Inha University, Korea; M.S., Texas A&M University

Co-Chairs of Advisory Committee: Dr. S. C. Lau
                                             Dr. Ed Marotta

The heat transfer characteristics of airflows in serpentine cooling channels in stator vanes of gas turbines and the novel QuTech® Heat Pipe (QTHP) for electronic cooling applications were studied. The cooling channels are modeled as smooth and roughened two-pass trapezoidal channels with a 180° turn over a range of Reynolds numbers between about 10,000 and 60,000. The naphthalene sublimation technique and the heat and mass transfer analogy were applied. The results showed that there was a very large variation of the local heat (mass) transfer distribution in the turn and downstream of the turn. The local heat (mass) transfer was high near the end wall and the downstream outer wall in the turn and was relatively low in two regions near the upstream outer wall and the downstream edge at the tip of the divider wall in the turn. The variation of the local heat (mass) transfer was larger with ribs on two opposite walls than with smooth walls. The regional average heat (mass) transfer was lower in the turn and higher in the entire channel with the flow entering the channel through the larger straight section than when the flow was reversed. The pressure drop across the turn was

higher with the flow entering the channel through the larger channel than when the flow was reversed.

Thermal performance of the QuTech[®] Heat Pipe was identified over a range of inclination angles between 90˚ and -90˚ and thermal mechanism of the QTHP was studied with GC-MS, ICP-OES, XRD, XPS, and DSC. This study resulted in the following findings: the performance of the QTHP was severely dependent on gravity; the QTHP utilizes water as working fluid; there were inorganic components such as Na, K, P, S, and Cr, etc.; and the vaporization temperature of the working fluid (mostly water) was lower than the boiling temperature of pure water. This was due to the presence of inorganic salt hydrates in the QTHP. It may be concluded that thermal performance of heat pipes increases with additional latent heat of fusion energy and energy required to release water molecules from salt hydrates.

DEDICATION

To my parents and *Jin Young*, Thank You

ACKNOWLEDGEMENTS

I would first like to thank my Lord and Savior Jesus Christ who led me to the present time and will lead me to the way that is His plan for me. May He receive all the honor and glory due Him.

I would like to express my appreciation to Dr. S. C. Lau for his guidance, encouragement and help throughout my graduate studies. I would like to thank Dr. Ed Marotta for his guidance and advice for the research, and thanks Dr. N. K. Anand, Dr. J. C. Han, and Dr. Y. A. Hassan for their advice and sharing their time for my research.

Special thanks to Dr. D. W. Goodman and Dr. A. Clearfield in the Chemistry Department. They provided great guidance and advice for my project. Without their help, I couldn't have finished the work. I would like to express special thanks to Dr. N. K. Anand throughout my graduate studies. Without his grace and support, I wouldn't have being writing the acknowledgements.

I am grateful to my parents, parents-in-law, and brother for their love, encouragement and prayers. Especially, I thank my wife, Jin Young, for her endless support, as well as my daughter, Jaini (Juyeon) and my son, Bennett (Sanghyup).

I would like to thank my friend, Michael Huh, for his encouragement and help to improve my English writing.

Finally, I also wish to thank the staff of the Department of Mechanical Engineering for their kindness and help provided during my studies at Texas A&M University.

TABLE OF CONTENTS

LIST OF FIGURES

LIST OF TABLES

NOMENCLATURE

A_c flow cross-sectional area at turn clearance, m^2

A_{HP} cross-sectional area based on inner wall diameter of heat pipe, m^2

A_s surface area, m^2

C_p specific heat of water, k*J/kgK*

D_h hydraulic diameter of flow cross section at turn clearance, m

f friction factor

f_0 reference friction factor for fully developed turbulent flow through smooth channel

h_m local mass transfer coefficient, m/s

$\overline{h}_m$ segmental or regional average mass transfer coefficient, m/s

k_{eff} effective thermal conductivity, *W*/mK

L streamwise distance between pressure taps, m

L_a length of adiabatic section of heat pipe, m

L_c length of condenser of heat pipe, m

L_e length of evaporator of heat pipe, m

L_{eff} effective length of heat pipe, m

L_i location of installed thermocouples along heat pipe, m

L_{Total} length of heat pipe, m

M. P.   melting point, °C

$\dot{m}$ air mass flow rate, kg/s

$\dot{M}_n$ rate of total mass transfer from upstream naphthalene surfaces, kg/s

$\dot{M}_n''$ local naphthalene mass flux, $kg/(m^2 \cdot s)$

Nu local Nusselt number

$\overline{Nu}$ segmental or regional average Nusselt number

Nu_0 reference Nusselt number for fully developed turbulent flow in smooth channel

p pressure, N/m^2

Pr Prandtl number

P_{input} supplied power to heaters, W

p_o absolute upstream pressure of the orifice, N/m^2

$p_{v,w}$ vapor pressure on naphthalene surface, N/m^2

P_w perimeter of flow cross section at turn clearance, m

$\dot{Q}_c$ rate of heat transfer to cooling jacket, W

$\dot{Q}_{Heat\,Loss}$ heat loss through six segments of test apparatus in axial and radial directions, W

$\dot{Q}_i$ heat loss through four segments of test apparatus in radial direction, W

$\dot{Q}_j$ heat loss through two segments of test apparatus in axial direction, W

$\dot{Q}_{net}$	net rate of heat transfer to evaporator, W
R	universal gas constant for air of 287, $J/kg \cdot K$
Re	Reynolds number
R_{NP}	universal gas constant for naphthalene of 64.87, $J/kg \cdot K$
Sc	Schmidt number
Sh	local Sherwood number
$\overline{Sh}$	segmental or regional average Sherwood number
Sh_0	reference Sherwood number for fully developed turbulent flow through smooth channel
T	temperature, K
T_{av}	average temperature of inside and outside temperatures of insulation, K
$T_{av,c}$	average of condenser temperatures, K
$T_{av,e}$	average of evaporator temperatures, K
T_{in}	inner insulation temperature of test apparatus, K
T_{out}	outer insulation temperature of test apparatus, K
T_{or}	orifice temperature, K
T_w	naphthalene surface wall temperature, K
$\dot{V}$	volumetric flow rate of air, m³/s
$\dot{V}_w$	volumetric flow rate of water, m³/s
$\overline{V}$	average velocity, m/s

Greek Symbols

ΔM_n total mass transfer from naphthalene surface to air, kg

Δp pressure drop across sharp turn, N/m^2

Δp_o pressure drop through orifice, N/m^2

Δt duration of experiment, s

$\Delta\left(T_e - T_c\right)$ average temperature difference between evaporator and condenser, ˚C

Δz local change of elevation on naphthalene surface, m

μ dynamic viscosity of air, $N{\cdot}s/m^2$

ρ density of air, kg/m^3

$\rho_{v,b}$ local bulk vapor density of naphthalene, kg/m^3

$\overline{\rho}_{v,b}$ average bulk vapor density of naphthalene, kg/m^3

ρ_s density of solid naphthalene, kg/m^3

$\rho_{v,w}$ vapor density of naphthalene on naphthalene surface, kg/m^3

ρ_w density of water, kg/m^3

σ mass diffusion coefficient of naphthalene vapor in air, m^2/s

CHAPTER I

INTRODUCTION

As technologies advance, researches on heat transfer are getting more important to achieve higher performance of devices. In particular, performance of gas turbine engines and CPUs has increased and their physical sizes have decreased. These smaller and more-efficient devices require their thermal energy to be dissipated faster and more efficiently. In order to dissipate thermal energy from the devices efficiently, knowledge on heat transfer related to the devices should be well defined. In cooling of airfoils of gas turbine engines, understanding of internal cooling schemes is required to achieve higher performance and thermal safety on their operation. Information on heat transfer distributions in the channels that model internal cooling geometries of gas turbine airfoils is essential to enhance the performance of internal cooling schemes. Similarly, in order to achieve higher performance and safe operation of CPUs, thermal energy dissipation devices such as heat pipes should be well understood and improved. With restrictions on space and heat sink materials of modern computers, passive and reliable devices that can dissipate thermal energy efficiently are essential. The purpose of this study is to obtain the detail thermal behavior of internal cooling channels that model gas turbine airfoils and a novel heat pipe that can be used in electronic applications.

―――――――――――

The model journal is the ASME Journal of Heat Transfer.

1.1 HEAT (MASS) TRANSFER DISTRIBUTIONS IN A TWO-PASS TRAPEZOIDAL CHANNEL WITH A 180-DEGREE TURN

Gas turbine engines are the most efficient among thermal engines. To increase the efficiency even further, it is critical to increase the inlet gas temperature thereby providing maximum useful thermal energy. Although state-of-the-art materials and thermal barrier coating technology have improved the performance of gas turbine blades, inlet gas temperatures are still limited. The combination of external and internal cooling of gas turbine airfoils has further increased the ability of the blade and vane to withstand high temperatures. By maximizing gas turbine blade cooling and minimizing the amount of fresh air drawn from the compressor, the gas turbine efficiency can be increased. In order to achieve higher efficiencies, knowledge of the cooling phenomena that occurs in gas turbine airfoils must be well defined.

Gas turbine airfoil cooling is categorized as either external or internal cooling. Film cooling and transpiration cooling technologies are used for external turbine blade surfaces, while impingement and forced convective cooling are widely used in internal cooling of turbine airfoils. Internal cooling can be sub-categorized into three different cooling regions, as shown in Fig. 1; a leading edge region with bleed holes that typically relies on impingement and forced convective cooling, a serpentine region that relies on forced convective cooling with sharp-turn induced flow reattachment, impingement and secondary flow, and a trailing edge region with bleed holes, that relies on forced convective cooling which incorporates short pin fin induced flow. Among the three
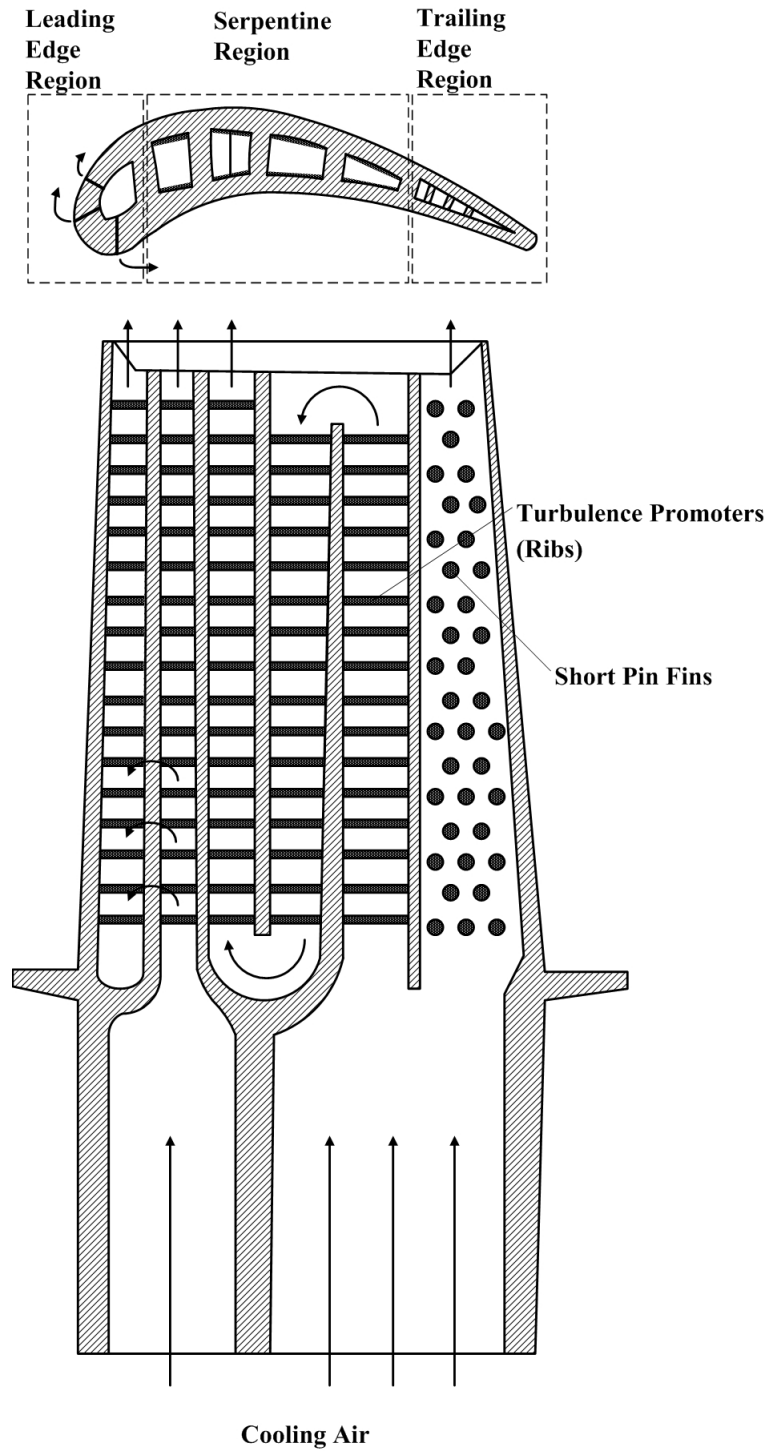
Fig. 1 Schematic of internal cooling regimes of a gas turbine airfoil

regions of internal cooling, serpentine region cooling relies on, as aforementioned, the enhanced convective heat transfer in the 180° sharp turn channel(s), where flow impingement, recirculation, and reattachment as well as additional secondary flow induced by the imbalance between centrifugal force and pressure force in turn region(s) on the flow region are taking place.

A literature survey shows that there have been a large number of studies on the heat transfer in stationary and rotating, straight and multi-pass channels, square and rectangular cross sections, and with rib-roughened walls. These studies have examined the effects of the aspect ratio of the channel, the geometry of the turn, the configuration of the ribs, and rotation, on the heat transfer distribution along the channel. The effects of rib configurations have been studied with transverse, angled (45˚, 60˚, 90˚, etc.), and discrete ribs and different angles of attack, height-to-hydraulic diameter ratios, pitch-to-height ratios, and pitch-to-hydraulic diameter ratios in square and rectangular cross sectional channels. The effects of coriolis and buoyancy due to rotation and the effects of channel orientation also have been studied in channels with square and rectangular cross sections. The results of these studies are useful in the design of serpentine cooling passages with turbulators in gas turbines. Many of these studies were discussed in two separate chapters in Han et al. [1]. In the case of turbulator-enhanced heat transfer for square and rectangular channels with no rotation, earlier studies include those by Burggraf [2], Han et al. [3], and Boyle [4]. Examples of more recent studies are Han et al. [5], Lau et al. [6], Acharya et al. [7], Ekkad and Han [8], and Rhee et al. [9]. In the case of heat transfer in rotating channels with sharp turns and turbulators, there are

earlier studies such as Johnson et al. [10 and 11] and more recent studies such as Park et al. [12 and 13], Lee et al. [14], Cho et al. [15], Liu et al. [16], Zhou and Acharya [17], and Ekkad et al. [18]. Burggraf [2] conducted heat transfer experiments in a square channel with smooth walls and two opposite rib-roughened walls. The channel was connected with three different kinds of entrance configurations: smooth long inlet, a short inlet with a screen that generated a uniform turbulence, and a 180º bend inlet channel. He concluded that heat transfer performance increases not only on the two rib-roughened walls but also on the two adjacent smooth walls, since neighboring turbulence promoters increase heat transfer. Han et al. [3] investigated the effects of rib height-to-pitch ratio, rib angle-of-attack, and rib height-to-hydraulic diameter on heat transfer enhancement and friction loss in a square channel. Boyle [4] studied the effect of three different 180˚ bend geometries, of a rectangular, semi-circular, and rounded corner bend. He also investigated the effect of rib height on local heat transfer in a relatively short length-to-hydraulic diameter square channel with thermocouples and foil heaters. The rib height-to-hydraulic-diameter ratio he considered were 0.6, 5, 10, and 15% at Reynolds numbers of 20,000~100,000 based on the hydraulic diameter of channels. He concluded that the three different 180˚ bend geometries had the same effect on heat transfer enhancement and the 5% rib height-to-hydraulic diameter ratio achieves highest heat transfer enhancement. Han et al. [5] studied local heat transfer distribution around a 180º turn in a two-pass square channel with smooth walls, and two opposing rib-roughened walls, by the naphthalene sublimation technique. They concluded that the flow separation and the secondary flow, that a 180º sharp turn induces, because heat transfer

enhancement after turn and the effect of ribs on two opposite walls along with those effects induced by 180º sharp turn further enhances heat transfer performance, compared to heat transfer enhancement on smooth walls. Lau et al. [6] studied the effects of V-shaped ribs on two opposite walls on heat transfer enhancement in a square channel, compared to the effects of transverse or full angled ribs on two opposite walls. They concluded that V-shaped ribs, of 45º or 60º angle, on two opposite walls show better heat transfer enhancement than transverse or full angled ribs, of 45º or 60º angle, on two opposite walls which have higher pressure drops. Ekkad and Han [8] conducted experiments to obtain the effects of the configurations of transverse, 60º full angled, 60º V-shaped, and 60º broken (discrete) V-shaped ribs on the local heat transfer distributions around a 180˚ sharp turn in a square channel at Reynolds numbers of 6,000~60,000 based on the hydraulic diameter of the channel with the transient liquid crystal

Trapezoidal-shaped internal cooling passages
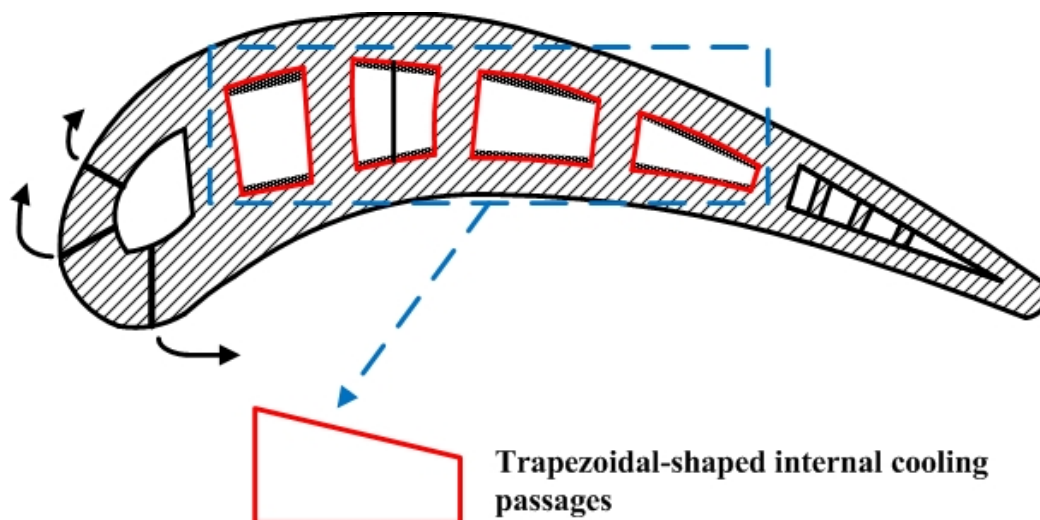
Fig. 2 Cutaway view of serpentine region cooling channels of turbine airfoils

technique. The results showed that 60º full angled, 60º V-shaped, and 60º broken V-shaped ribs have higher heat transfer enhancement than transverse ribs. Ekkad et al. [18] obtained the local heat transfer distributions at a sharp 180° turn in a two-pass square channel with smooth walls, rib turbulators on two opposite walls, and with bleed holes on two opposite walls.

Research attention has been focused on heat transfer enhancement in smooth and rib-roughened walls, square and rectangular cross-sections, single and multi-pass channels with and without rotation. Experimental and numerical studies have modeled the serpentine region of the gas turbine airfoil mostly with square or rectangular cross-sectioned channels, with and without multi-pass with 180° sharp turn(s). However, these shaped cooling passages often have irregular cross sections. Internal cooling passages of the serpentine region of turbine airfoils are rather trapezoidal-shaped channels as shown in Fig. 2. A few studies, such as Taslim et al. [19 and 20], Li et al. [21], and Moon et al. [22], have been conducted to investigate the effects of irregular geometries on heat transfer performance with and without turbulators in single and multi-pass internal cooling passages. Taslim et al. [19] modeled cooling passages near the trailing edge of gas turbine airfoils and studied the effects of tapered ribs in trapezoidal channels on the heat transfer and pressure drop with and without bleed holes. They found that there was a large spanwise variation of heat transfer coefficients due to the non-uniform spanwise geometrical shape of the ribs and channels. Taslim et al. [20] presented heat transfer results for twelve straight channels with square and trapezoidal cross sections, with full ribs on two opposite walls, and with and without half-length ribs on the other two walls.

They found that the half-length ribs significantly enhanced the heat transfer on the two walls with full ribs. Li et al. [21] reported local heat transfer distributions for flows through wide trapezoidal channels with holes along a straight and zigzag divider wall, and with ejection slots along one outer wall. Moon et al. [22] conducted transient heat transfer experiments using encapsulated thermochromic liquid crystals to obtain the local distributions of the heat transfer coefficient on all of the walls at the turn of a smooth two-pass channel with a trapezoidal cross section. They considered various rates of air flow through the channel. They found that the heat transfer was much higher on the walls in the turn region and downstream of the turn than on the walls upstream of the turn. The turn caused high heat transfer in several distinct regions on the end wall, the outlet outer wall, and on the two opposite primary walls in the turn and downstream of the turn. The flow separated at the tip of the divider wall and reattached on the outlet inner wall in a location only a short distance from the turn. The heat transfer was the lowest on the inlet outer wall. Heat transfer enhancement due to the turn was the highest in the lowest Reynolds number case. The trends of the local heat transfer distributions on the various walls at the turn were relatively insensitive to varying the flow rate. Although Taslim et al. [19 and 20] and Li et al. [21] investigated the effects of irregular geometries, i.e. trapezoidal cross sectional channels, on heat transfer performance with and without turbulators, the effects of irregular geometries on heat transfer performance with and without turbulators have not been studied in multi-pass channels.

In this study, cooling channels in turbine airfoils were modeled as a channel with two straight trapezoidal sections connected with a sharp 180° turn. The effect of the turn

on the distribution of the local heat transfer was studied for the cases of a channel with smooth walls, a channel with transverse ribs on one wall, and a channel with transverse ribs on two opposite walls. Naphthalene sublimation experiments were conducted to obtain the mass transfer distributions, and the heat and mass transfer analogy was used to convert the mass transfer distributions to heat transfer distributions. The results of this study should help gas turbine designers determine local temperature distributions in cooling passages in turbine airfoils and to identify regions with large temperature variations and high thermal stresses. The results will also enable engineers to develop numerical models to optimize these internal cooling passages to improve the thermal performance of gas turbines.

1.2 THERMAL CHARACTERISTICS AND MECHANISMS OF A NOVEL HEAT PIPE

Since the initial conceptual introduction of heat pipes and closed two-phase thermosyphons (gravity assisted wickless heat pipes) by Perkins and Buck [23], Gay [24], Gaugler [25] and Grover et al. [26], as mentioned in Peterson [27], numerous investigations have been conducted to understand the characteristics and limitations of these devices. Research efforts have helped to maximize performance of heat pipes and thermosyphons in various applicable fields such as airspace and aircraft cooling, heat exchangers, electronic cooling, and solar energy conversion. In the 1980s and early 1990s, special focus was placed on the research and development of heat pipes and closed two-phase thermosyphons in airspace and aircraft industries [28 and 29]. The reason heat pipes and closed two-phase thermosyphons have been widely used is that there are three representative advantages of heat pipes and closed two-phase thermosyphons when compared to heat transfer devices that utilize single-phase or conductive heat transport mechanism. These advantages are cited by Peterson [27] and Eastman [30]. First, heat pipes and closed two-phase thermosyphons have several orders of magnitude higher heat capacity than even the best solid conductors, depending on their size. This is because of the two-phase heat transport between a liquid and its vapor through latent of heat of vaporization. The two-phase heat transport mechanism provides higher heat transfer by several orders of magnitude when compared to other devices utilizing single-phase or conductive heat transport mechanism. Second, heat pipes and

closed two-phase thermosyphons can be used as isothermal devices with a very low penalty of temperature drop through the heat transport medium. A large amount of heat can be transported through very low temperature difference of less than several degrees. Third, the thermal response time of heat pipes and closed two-phase thermosyphons is much shorter than other heat transfer devices and is not dependent on their length. Research and development on heat pipes and closed two-phase thermosyphons has been actively implemented, because of the above mentioned superior advantages to conventional heat transfer devices.

Dobran [28] reviewed research and development on heat pipes that had been conducted in 1980s. Most research conducted in that decade was related to space applications where gravity can not play a dominant role on returning the working fluid to an evaporator. He selectively reviewed the developments in heat pipe internal geometry which helped to maximize the capillary force on the working fluid. The internal geometry helps to return the working fluid to the evaporator by maximizing the capillary force and minimizing contact of liquid flow with counter-current vapor flow. The geometries which have been developed are monogroove, tapered artery, trapezoidal axially grooved, dual slot, double wall, and dual pair artery wick. As mentioned earlier, those geometries focused on separation of liquid flow with counter-current vapor flow to minimize flooding or entrainment limit which is the usual limiting factor against operation of heat pipes that are used in space and aircraft applications where high operating temperatures and high heat transfer capacities are demanded.

Due to electronic technology advancement in the early 1990s, dissipation of generated heat has become very challenging. Dissipation of the generated heat is required to ensure reliable operation of the more advanced microelectronic devices. In order to meet these thermal dissipation requirements, interest in heat pipes and closed two-phase thermosyphons has increased. Palm and Tengblad [31] reviewed studies on heat pipes and closed two-phase thermosyphons (thermosyphon pipe, thermosyphon loop, and advanced thermosyphon loop with extended condenser and evaporator surfaces) applicable to cooling of electronics. They concluded that when possible in design respects, closed two-phase thermosyphon pipes or loops that utilize gravity to return working fluid to an evaporator need to be considered first. This is because of the higher thermal efficiency and capacity of the thermosyphon when compared to heat pipes. Nevertheless, heat pipes that use capillary force to return liquid should be considered where horizontal thermal transport is indispensable.

The thermal characteristics of heat pipes and closed two-phase thermosyphons are dependent on inclination angles, filling charge ratios (FR), geometries, and power densities (heat transport capacities). Hahne and Gross [32] showed that a closed two-phase thermosyphon has its maximum performance at 40° angle from its vertical position (evaporator at bottom and condenser at top). The performance is strongly dependent on whether the generated condensed liquid film inside wall in the condenser region is turbulent or laminar. They mentioned that laminar film inside wall should be avoided to achieve higher performance. Gurses et al [33] and Bilegan and Fetcu [34] also showed that the effect of inclination angle on performance of heat pipes is critical

with worst performance at the horizontal location. Park et al. [35] investigated the effect of the filling charge ratio (FR) of the working fluid on thermal performance in a closed two-phase thermosyphon. They found that an increase of the FR does not enhance the heat transfer in the evaporator. However, it enhances the heat transfer in the condenser, because heat transfer occurs from higher temperature working fluid to the lower part of condenser directly without vaporization when the FR is large. They also mentioned that the maximum heat transfer limit varies with different the FRs. When the FR is small, dry-out of two-phase closed thermosyphon occurs from the bottom of the evaporator. When it is large, dry-out occurs from the top of the evaporator by flooding limit. Noie [36] studied the thermal characteristics of a two-phase closed thermosyphon with the working fluid filling charge ratio ranging from 30 to 90% and a variation in length of the evaporator. He found that the length of the evaporator and the filling ratios are intrinsically related to each other. El-Genk and Saber [37] developed a 1-D steady state model that provides the operating range and limit of closed two-phase thermosyphon with specified working fluids, initial filling charge ratio, evaporator length, power input, vapor temperature, and tube diameter. They concluded that tube diameter, evaporator length, and vapor temperature are dominant factors on thermal performance of closed two-phase thermosyphon, rather than condenser or adiabatic section length.

Although heat pipes and closed two-phase thermosyphons, which utilize two-phase latent heat of vaporization, are superior to other types of heat transfer devices and improved during the past few decades, improvements with even more advanced technology will help to meet the higher thermal dissipation requirements. One possible

alternative to improve current heat pipes or closed two-phase thermosyphons is the QuTech[®,] Heat Pipe (QTHP).

The QTHP claims to be different from conventional heat pipes and closed two-phase thermosyphons with respect to thermal transport mechanism. Conventional heat pipes and closed two-phase thermosyphons utilize latent heat of vaporization of the working fluid to remove supplied thermal energy. The QTHP has three coated layers inside the tube, as mentioned in US Patent 6,132,823 [38]; the first layer is the 'anti-corrosion layer' that prevents etching or oxidizing of the inner surface of the tube. It consists of sodium, beryllium, manganese, aluminum, calcium, boron, and dichromate radical and has a thickness of 8~12 μm. The second layer is the 'active heat transfer layer' that prevents generation of hydrogen and oxygen and serves as the heat transfer medium by conduction. It consists of cobalt, manganese, beryllium, strontium, copper, titanium, potassium, aluminum, dichromate radical and has a thickness of 8~12 μm. The third layer is the 'black powder layer' that transfers heat or energy through oscillation and consists of potassium dichromate, sodium dichromate, silver dichromate, monocrystalline silicon, beryllium oxide, strontium dichromate, boron oxide, aluminum dichromate, and manganese dichromate, as shown in Fig. 3.

The focus of this study is to determine/quantify the thermal characteristics of the QTHP and identify the possible thermal transport mechanism of the QTHP by means of chemical and thermal analysis. Thermal performance of the QTHP was characterized at various inclination angles and power throughput to an evaporator of the QTHP. Its performance was compared against the performance of a conventional closed two-phase

copper-water thermosyphon. Chemical and thermal analyses were conducted to obtain chemical compositions and thermal characteristics by means of Gas Chromatograhy-Mass Spectrometry (GC-MS), Inductively Coupled Plasma-Optical Emission Spectrometer (ICP-OES), X-ray Photoelectron Spectroscopy (XPS), X-ray Diffraction (XRD), and Differential Scanning Calorimetry (DSC).

'Black Powder Layer'
'Active Heat Transfer Layer'
'Anti-corrosion Layer'

$8{\sim}12\mu m$
$8{\sim}12\mu m$
$8{\sim}12\mu m$

Copper Tube
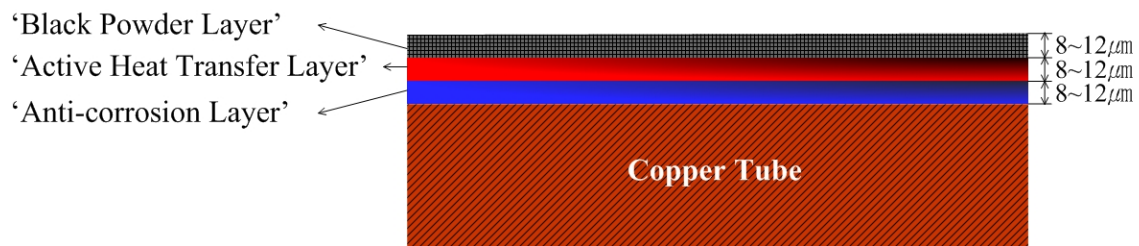
Fig. 3 Schematic of solid compounds that is claimed to have three solid layers inside surface of QuTech[®]'s Heat Pipe, as mentioned in US Patent 6,132,823 [38]

CHAPTER II

HEAT (MASS) TRANSFER DISTRIBUTIONS IN A TWO-PASS

TRAPEZOIDAL CHANNEL WITH A 180-DEGREE TURN

2.1 EXPERIMENTAL APPARATUS

A schematic of the test apparatus used in this study is shown in Fig. 4. The test

section (trapezoidal channel with 180° sharp turn) was connected to a 6.35-*cm* inner

diameter PVC pipe open flow loop. The flow loop consisted of a settling plenum

chamber, an orifice flow meter with a 3.81-*cm* hole-diameter orifice plate, an air-flow

control valve, and two centrifugal blowers connected in series. The test section was a

two-pass channel with two straight sections of different trapezoidal cross sections,

connected with a sharp 180° turn. The channel was constructed of 1.91-*cm* thick pine

wood. As shown in Fig. 5, the length of each straight section, or the distance between the

channel inlet, or exit, and the end wall at the turn, was 61.0 *cm* [see Fig. 5(a)], while the

width of each section was 3.81 *cm* and the thickness of the inner/divider wall between

the two sections is 1.91 cm [see Fig. 5(c)]. The width of the clearance at the turn, i.e. the

distance between the tip of the divider wall and the end wall, was also 3.81 *cm*. The top

and bottom walls of the test channel were both flat and were at an angle of 21.8° with

Pressures measured with inclinded manometer and calibrated pressure transducer

Orifice flow meter

Settling plenum

Air to flow meter

Air in

Gate valve

Blowers

Air out

Trapezoidal test channel with sharp turn

Naphthalene surface
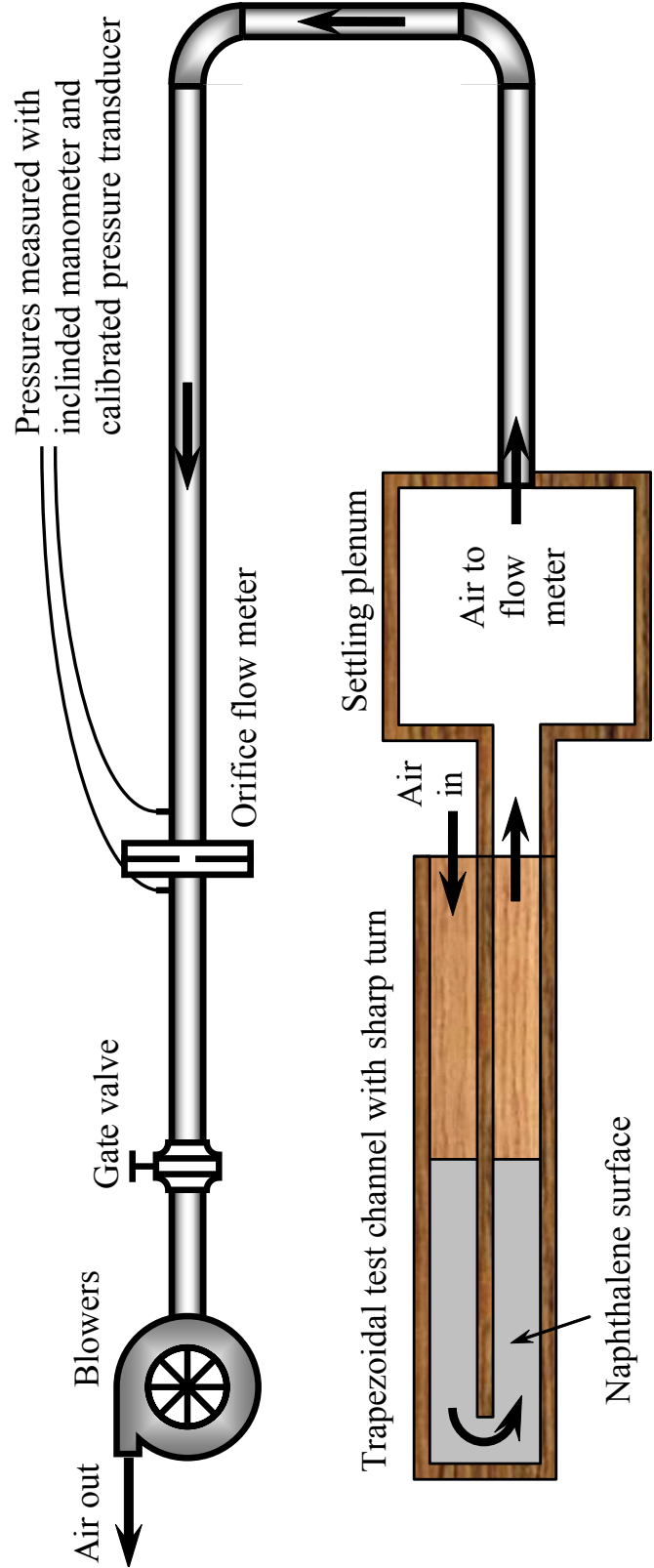
Fig. 4 Schematic of test apparatus
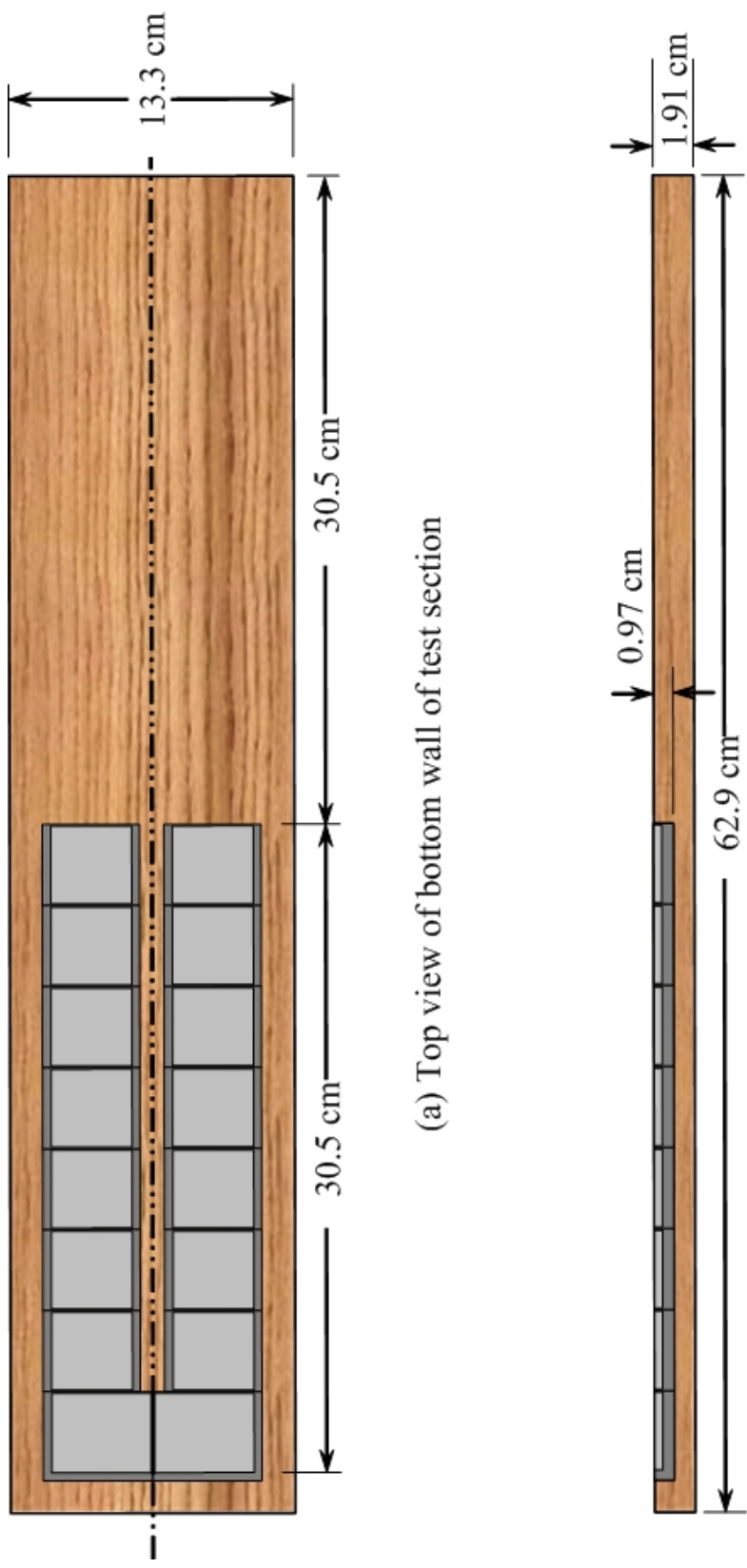
(a) Top view of bottom wall of test section

(b) Side view of bottom wall of test section

Fig. 5 Schematics of walls of trapezoidal test channel

3.81 cm

3.81 cm

1.91-cm thick
divider wall

Side walls

16 naphthalene cassettes

End wall
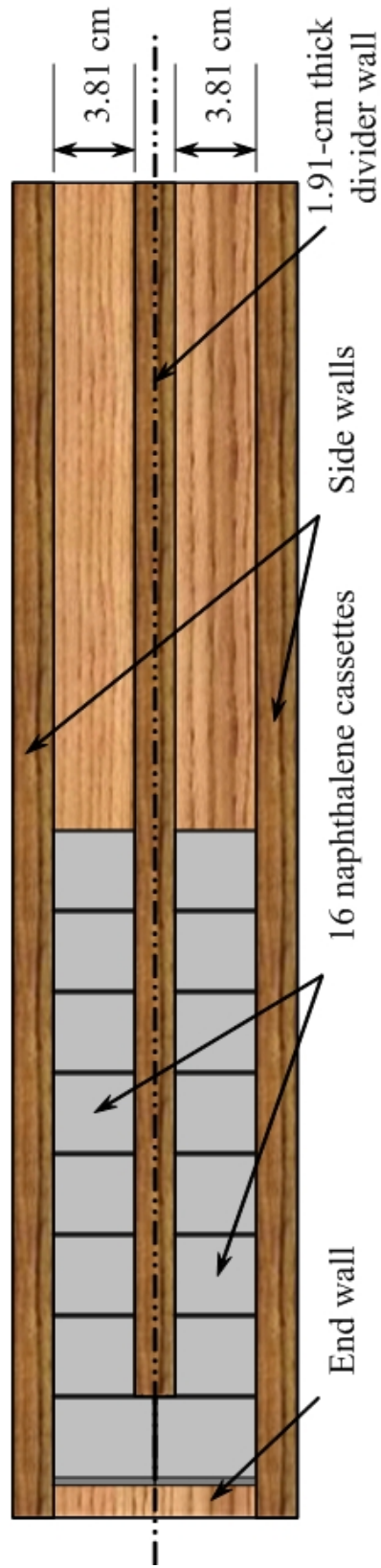
(c) Top view of test channel with top wall removed

Fig. 5 (continued)

Outer side wall

Top wall

7.62 cm

3.81 cm

Outer side wall

Divider wall

Bottom wall

(d) Cutaway view of cross section of test channel

U-shaped naphthalene cassette for turn region

(e) Top view of bottom wall of test channel with one-piece naphthalene cassette at turn region for local mass transfer measurements
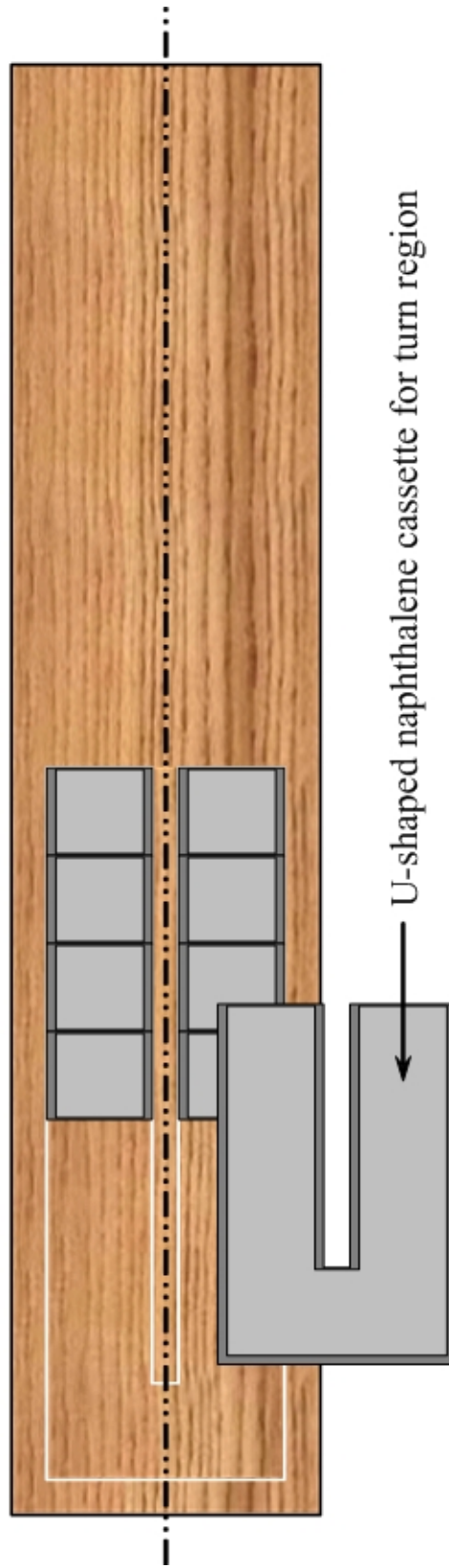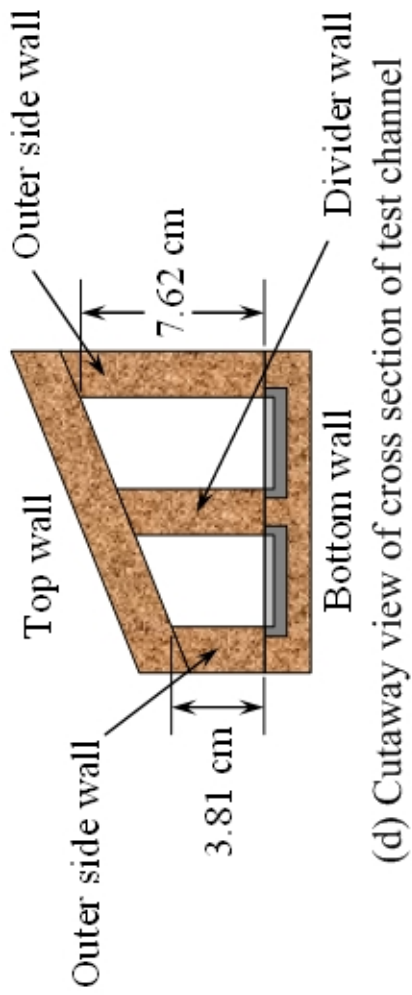
Fig. 5 (continued)

respect to each other, such that the heights of the outer and inner vertical walls of one straight section were 3.81 *cm* and 5.33 *cm*, and the heights of the inner and outer vertical walls for the other straight section were 6.10 *cm* and 7.62 *cm*, respectively, as shown in Fig. 5(d). All of these dimensions are for the inside surfaces of the channel walls.

As shown in Fig. 5(a), a 30.9-*cm* long U-shaped section on the inside surface of the bottom wall was hollowed out to a 0.97-*cm* depth to facilitate the installation of sixteen aluminum cassettes for the determination of the streamwise variation of the regional average mass transfer coefficient along the channel. Each of the sixteen cassettes was 0.97 *cm* thick and had a 0.38 *cm* deep cavity, as shown in Fig. 6. Fourteen square cassettes with sides of 3.81 *cm*, including two 0.76-*mm* thick rims that were not mass transfer active surfaces, were used in the straight portions of the two channels [see Fig 6(a)]. Whereas, two other cassettes at the turn region had a height of 4.76 *cm*, including a 0.76-*mm* thick rim, due to the 1.91-*cm* thick divider wall [see Fig. 5(c)] and a width of 3.81 *cm* [see Fig. 6(b) and 6(c)]. During the casting process, the cavity was filled with naphthalene, exposing a smooth, flat surface that was mass transfer active. The width of the naphthalene surfaces on the fourteen cassettes was 3.81 *cm*, which was the same as the width of each straight section of the test channel. The two other cassettes that made up the portion of the bottom wall at the turn with naphthalene surfaces measured 3.73 *cm* x 4.69 *cm*, excluding each 0.76-*mm* thick rim from width and height of cassettes. Once these sixteen cassettes were installed, the 30.5-*cm* long inner surface of the bottom wall was mass transfer active, except for the top of two 0.76-*mm* wide rims of each cassette, as mentioned earlier. The other two wider rims of each cassette,
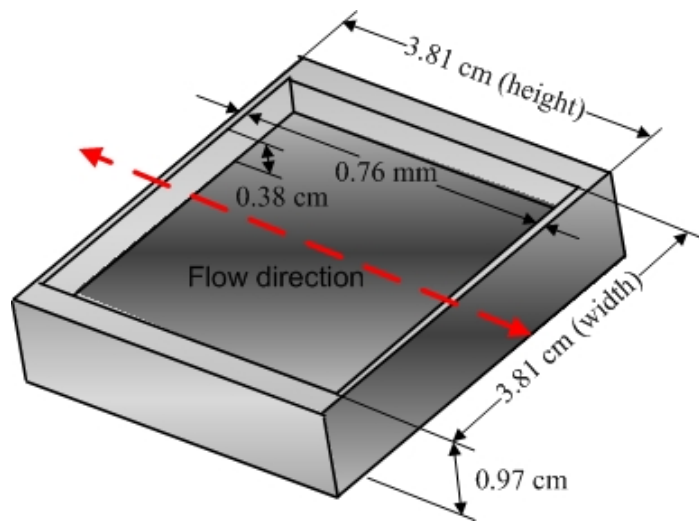
(a) Aluminum cassette along two straight channel of test section
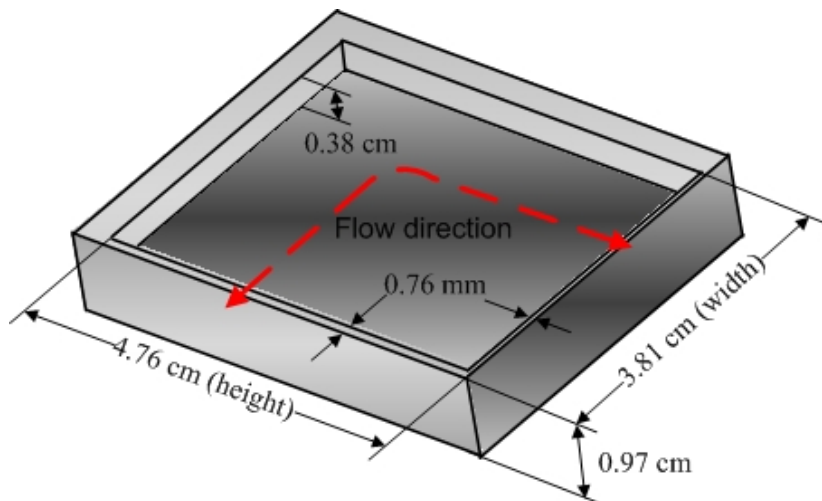
(b) Aluminum cassette at upper turn region of Fig. 5(a)

Fig. 6 Schematics of aluminum cassettes to contain mass transfer active surfaces along test channel
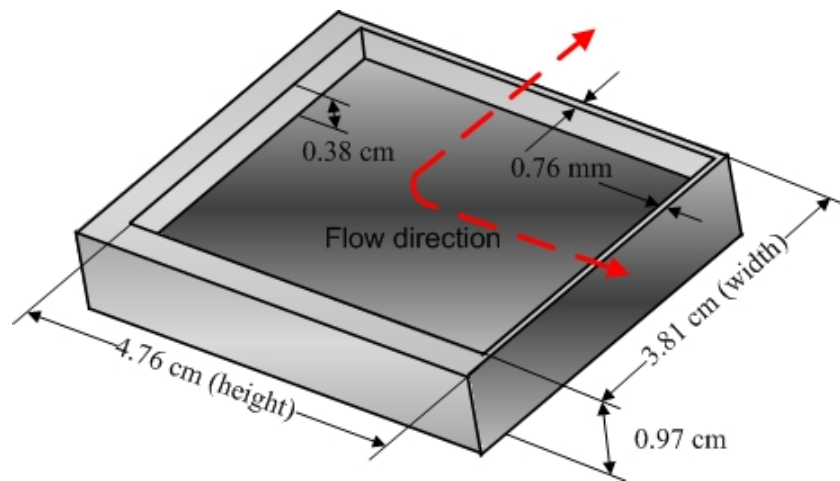
(c) Aluminum cassette at lower turn region of Fig 5(a)
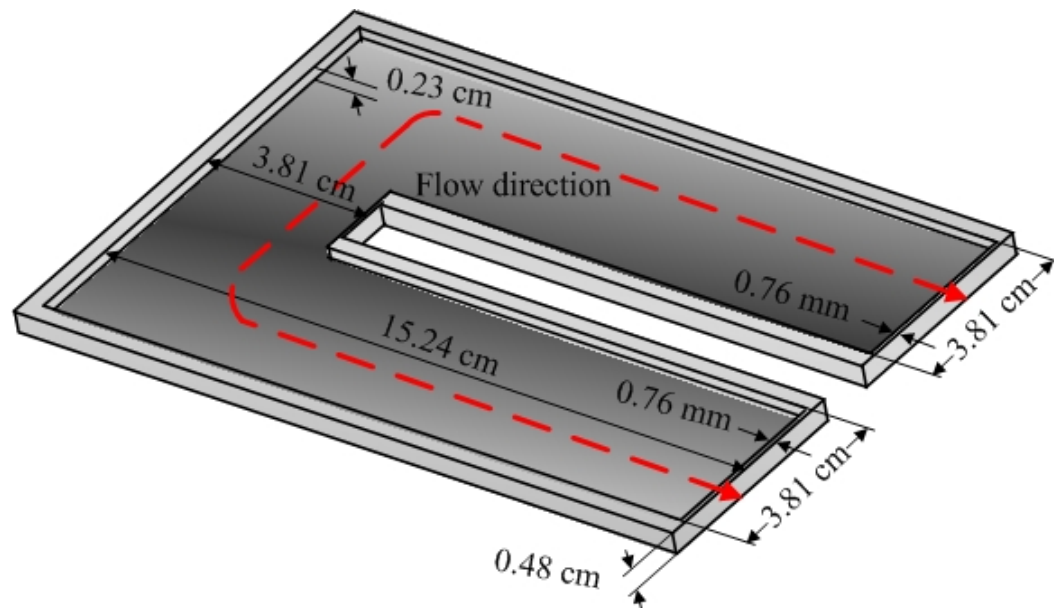
(d) Aluminum cassette at turn region for local mass transfer experiment of Fig 5(e)

Fig. 6 (continued)

with a thickness of 3.81 *mm*, were hidden underneath the divider wall, one of the two outer walls, or the end wall. The bottom wall, therefore, consisted of a 30.5-*cm* long mass transfer inactive entrance to ensure hydro-dynamically fully developed flow before the flow was exposed to mass transfer active surfaces. The entrance and outlet regions were connected with 30.5-*cm* long mass transfer active surfaces around the 180º sharp turn region.

To enable the measurement of the distribution of the local mass transfer at the turn, the eight cassettes closest to the turn were replaced with a U-shaped cassette [see Fig. 5(e)]. The U-shaped cassette had a width of 3.81 *cm* and a height of 15.24 *cm*, including a 0.76-*mm* thick rim at entrance and outlet, as shown in Fig. 6(d). Once this U-shaped cassette was installed on the bottom wall, the surface of the entire turn region of the bottom wall was mass transfer active for local mass transfer distribution experiments. For confidence of local mass transfer experiments, weighing of the U-shaped cassette was required for comparison with averaged mass transfer of all of measuring points of the U-shaped cassette. In order to weigh the U-shaped cassette, an electronic balance that had range up to 160.0 *g* was used. The U-shaped cassettes were machined to have a 0.48-*cm* thickness and 0.23-*cm* deep cavity [see Fig. 6(d)]. A 0.49-*cm* thickness U-shaped plate was placed underneath the U-shaped cassette so that it would fit into the 0.97-*cm* deep hollowed-out space of the bottom wall of the test channel.

Regionally averaged mass transfer coefficients were obtained with turbulence promoters (ribs). Two different cases were considered. The first case used ribs on the bottom wall only. The second case used ribs on both the top and bottom walls. Local
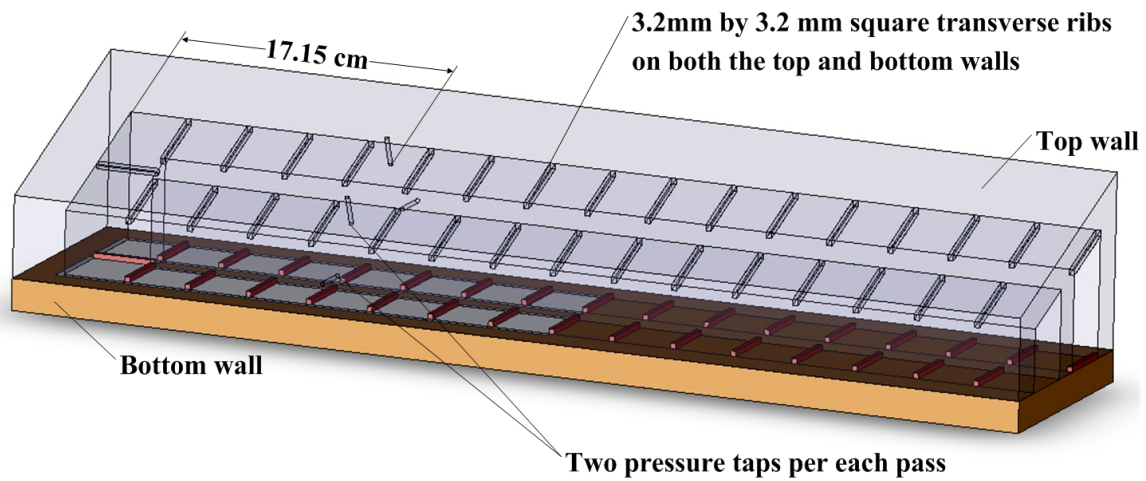
Fig. 7 Schematic of trapezoidal channel with 3.2 *mm* by 3.2 *mm* square transverse ribs and two pressure taps installed on both top and bottom walls and on top and side walls of each passage, respectively

mass transfer coefficients were obtained for only one case; ribs on the bottom and top wall. For all cases studied, the rib spacing was 3.81 *cm* as shown in Fig. 7.

These ribs were 3.2 *mm* x 3.2 *mm* square stripes of balsa wood. Thus, the distance between two consecutive ribs was equal to 12 times the height of the ribs. On each naphthalene cassette, the balsa wood strip was installed on top of the 0.76-*mm* thin rim along the downstream edge of the cassette to maximize mass transfer active surface area of each cassette.

To measure pressure drops and obtain friction factors through the turn of the channel, two pressure taps were installed at a distance of 17.15 *cm* from the end wall of each straight channel [see Fig. 7]. To insure proper measurements of gauge pressure

across the turn of the channel, each passage of the test channel had the two pressure taps, because of the trapezoidal shaped cross-section of the channel.

2.2 EXPERIMENTAL PROCEDURE

As was shown in Fig. 5(d), the test section has two trapezoidal straight sections with a divider wall in-between the two sections. The experiments first used the smaller trapezoidal section as the inlet with the larger section as the outlet. Afterwards, the larger trapezoidal duct was used as the inlet and the smaller duct served as the outlet. For each test configuration mentioned, four Reynolds numbers were considered. Regional average and local mass transfer coefficients are obtained for air flows through the test channel with smooth walls, and with transverse ribs on one wall and on two opposite walls. The analogy of heat and mass transfer is applied to convert the mass transfer coefficients to heat transfer coefficients.

The two-pass trapezoidal test channel was connected to a settling chamber (plenum) and then to an open air flow loop [see Fig. 4]. During an experiment, fresh air was drawn, by two centrifugal blowers connected in series, through the flow loop from the air-conditioned laboratory and the exhaust air that contained naphthalene vapor was ducted to the outside of the laboratory through a fume hood. The air mass flow rate was controlled with a valve and was calculated from measured pressure drop through an ASME sharp edge 3.81-*cm* hole-diameter orifice plate and absolute pressure upstream of

the orifice plate. The pressure drop was measured with an inclined manometer and the upstream pressure was measured with a calibrated Cole Parmer pressure transducer with a digital TRMS multi-meter. The temperature of the air at the entrance of the test section was measured with two 30 gage T-type thermocouples, which were carefully calibrated with a NIST calibrated thermometer and a constant temperature bath, and was monitored continuously with a data acquisition system over the duration of the experiment. The data acquisition system consisted of a National Instrument's PCI-6024E board, a SCXI-1102 conditioner, a TC-2095 terminal block, and a computer on which Labview 7.0 was installed.

To ensure that the naphthalene in all of the cassettes was in thermal equilibrium with the air in the air-conditioned laboratory, the cassettes were stored in sealed plastic bags in the laboratory for at least 12 hours before an experiment. After each experiment, the remaining naphthalene in all of the cassettes were melted and thrown away. All of the cassettes were cast with new melted naphthalene to ensure best results of regional average and local mass transfer experiments.

To obtain the pressure drop across the turn, two pressure taps were installed on the top wall and the outer side wall, respectively, in each of the two straight sections of the trapezoidal test channel, as mentioned earlier [see Fig. 7]. These pressure taps were located on the centerlines of the walls at a distance of 17.15 *cm* and 43.80 *cm* from the channel end wall and the channel inlet and exit, respectively. The difference in the static pressures at these two pairs of taps was measured with a Dwyer 1430 microtector electronic point gage that could measure up to a 5.08-*cm* water column with a resolution

of $\pm$ 6.35 $\times$ 10^{-3} *mm* or a calibrated Cole Parmer pressure transducer with a digital TRMS multi-meter that could measure up to a 25.40-*cm* water column with a resolution of $\pm$ 2.54 $\times$ 10^{-2} *cm*, depending on the range of the measured pressure drops through the turn of the trapezoidal channel.

To validate the experimental method, additional local and average mass transfer experiments were conducted for flow through a two-pass square channel. For these experiments, the test channel had the same bottom wall with the naphthalene cassettes as the trapezoidal channel, and the side walls, the divider wall, and end wall had a height of 3.81 *cm*, the same as the width of each straight section of the channel. Experiments were conducted to obtain the local mass transfer distributions on the bottom wall at the turn, and the streamwise variations of regional average mass transfer, for four different air flow rates. The local mass transfer distributions at the turn and the variations of regional average mass transfer obtained were compared with those reported by other researchers in the open literature.

2.2.1 Regional Average Heat (Mass) Transfer

Before each regional average mass transfer experiment was conducted, pre-determined air flow rate, which gave turn-clearance based Reynolds number of 9,400 ~ 57,200, was carefully adjusted with a valve to minimize preparation time of each

experiment and thus un-wanted mass transfer loss. To determine the variation of the sixteen regional average mass transfer coefficients along the two-pass test channel, the sixteen naphthalene cassettes were weighed and recorded five times for a statistical purpose, one at a time, with a Sartorious electronic balance that had a range up to 160.0 g with a resolution of 0.1 mg before and after the experiment. Each experiment was run for 15, 25, 35, and 60 minutes with corresponding turn clearance based Reynolds number of 57,200, 31,800, 16,800 and 9,400, respectively. Duration of each experiment was carefully chosen such that amounts of the sublimated naphthalene for each cassette were comparable to each other for four different Reynolds numbers to minimize uncertainties of the experiments. Installation and un-installation of the sixteen cassettes in the test section were executed carefully and promptly to minimize un-wanted mass transfer loss to ambient. Every step in each experiment including weighing of the sixteen cassettes before and after the experiment, installation and un-installation of the sixteen cassettes in the test section, assembly and disassembly of the test channel, and turning on and off blowers was timed to account for an amount of the un-wanted mass transfer during the experiment. The difference between the weights of each of sixteen cassettes gave an amount of the mass transfer from the naphthalene surface of a cassette to airflow during the experiment, which was reduced to regional average mass transfer distribution along the test channel. Auxiliary experiments were conducted, after each experiment was performed, to account for mass transfer loss that was sublimed during the start and end of the suction pump(s) operation and the preparation of the experiment.
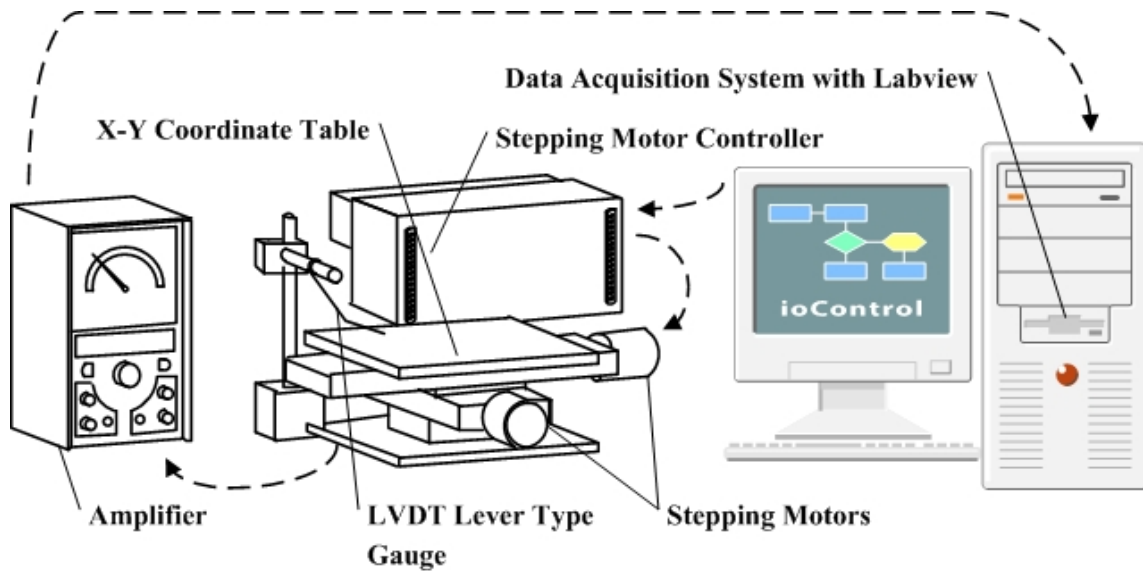
Fig. 8 Schematic of height measurement system: a Starrette LVDT Lever Type Gauge, an amplifier, a X-Y coordinate table with two stepping motors, a Velmex stepping motor controller, and a data acquisition system for local mass transfer experiments

2.2.2 Local Heat (Mass) Transfer

In order to measure height differences that were reduced to local mass transfer coefficient distributions on the U-shaped cassette, a Starrette electronic depth gauge was positioned and measured heights of pre-determined points on the U-shaped cassette by moving a X-Y coordinate table that the U-shaped cassette was placed on, as shown in Fig. 8. The electronic depth gauge had a lever type LVDT head with a range of ±0.2 *mm* and a resolution of 0.002 *mm*, and the X-Y coordinate table was controlled by two

Total measuring points=3,776

Δx=1.895 mm
Δy=1.905 mm

$N_{x,1}$=82

$N_{y,1}$=22

Region 1

$N_{y,2}$=8

$N_{x,2}$=21

Region 2

$N_{y,3}$=22

Region 3

Measuring path

$N_{x,3}$=82
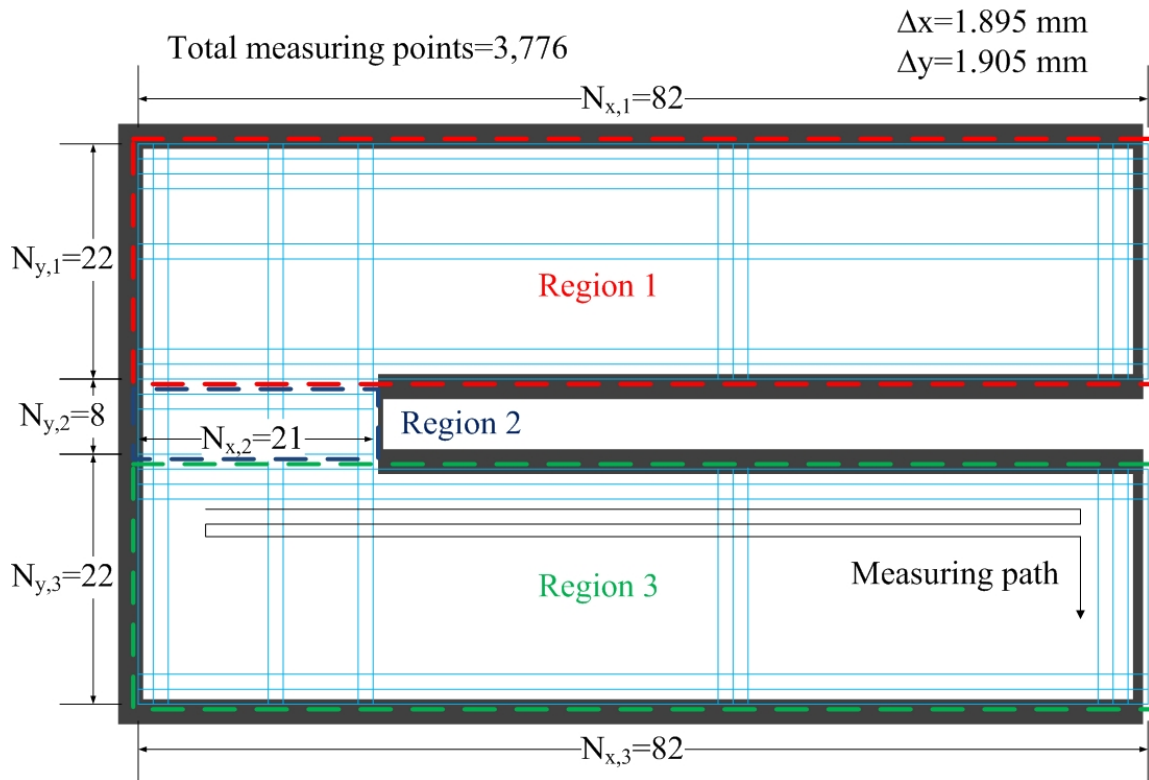
Fig. 9 Schematic of pre-determined 3,776 measuring points on U-shaped aluminum cassette for local mass transfer experiments

stepping motors and a Velmax NF90 stepping motor controller. The stepping motor moved 5.08×10^{-3} *mm* per step. The motor controller was controlled by a computer that Labview was installed on. The computer recorded height data from the electronic depth gauge. The U-shaped cassette was placed on the X-Y coordinate table, elevations on 3,776 points of region 1, 2, and 3 on the U-shaped cassette, including elevations on the top surface of the rim of the U-shaped cassette, were measured [see Fig. 9]. The

elevations on the top surface of the rim were measured to determine the location of the reference plane of the naphthalene surface in the calculations of the elevation changes at the grid points on the naphthalene surface. The changes of the elevations at the grid points were used to calculate the local mass transfer coefficients. In order to keep the same experimental conditions with the regional average mass transfer experiments, four cassettes upstream of the U-shaped cassette and four cassettes downstream of the U-shaped cassette were also prepared to be mass transfer active surface. Each experiment was run for 40, 60, 90, and 140 minutes, with corresponding Reynolds number of 57,200, 31,800, 16,800 and 9,400, respectively. Duration of each experiment was carefully adjusted so that an amount of mass transfer for each experiment was comparable to each other experiments at different Reynolds numbers.

As the regional average mass transfer experiments, auxiliary experiments were conducted, after each experiment was performed, to account for the un-wanted mass transfer amount that was included in the obtained local mass transfer results during startup and shutdown of blowers, weighing the cassette, and measuring elevations on the surfaces of the cassettes, etc.

2.3 DATA REDUCTION

Based on pre-determined channel turn-clearance based Reynolds numbers to be used for experiments, pressure drop through orifice and absolute upstream pressure of orifice were estimated. When experiments were conducted, measured pressure drop and absolute upstream pressure of orifice, with an inclined manometer and a Cole Parmer calibrated pressure transducer, respectively, were used to obtain air mass flow rate through orifice with the following equation

$$\dot{m} = \frac{\pi}{4} d_o^2 CY \left[\frac{2 p_o \Delta p_o}{R T_{or} (1 - \eta^4)} \right]^{\frac{1}{2}} \quad [{kg}/{s}] \tag{1}$$

where p_o was the absolute upstream pressure of the orifice, Δp_o was the pressure drop through orifice, T_{or} was the temperature at the orifice, d_o was the diameter of the orifice and was equal to 3.81 cm, η was the orifice-diameter-to-pipe-diameter ratio and was equal to 0.6, and R was the universal gas constant for air of 287 $[J/kg \cdot K]$. Discharge coefficient, C, was obtained from

$$C = 0.5959 + 0.0312 \eta^{2.1} + \frac{91.71 \eta^{2.5}}{Re_{dp}^{0.75}} - 0.01584 \eta^3 + \frac{0.0390 \eta^4}{1 - \eta^4} - 0.1840 \eta^8$$

$$\tag{2}$$

where pipe Reynolds number, Re_{dp}, was given by

$$Re_{dp} = \frac{4 \dot{m}}{\pi d_p \mu} \tag{3}$$

where d_p was the diameter of the pipe at the orifice and was equal to 6.35 *cm*.

Expansion coefficient, Y, was obtained with

$$Y = 1.0 - \frac{\left(0.41 + 0.35\eta^4\right)\Delta p_o}{1.4 p_o} \tag{4}$$

Once air mass flow rate was determined for each experiment, Reynolds number for flow through the test channel was obtained by

$$\text{Re} = \frac{\rho \overline{V} D_h}{\mu} = \frac{4\dot{m}}{\mu P_w} \tag{5}$$

where D_h and P_w were the hydraulic diameter and the perimeter of the rectangular flow cross section between the tip of the divider wall and the end wall. For the same air mass flow rate, the two Reynolds numbers based on the hydraulic diameters of the trapezoidal cross sections of the two straight sections of the test channel were 10.5% smaller and 13.5% larger than this Reynolds number based on the hydraulic diameter of the cross section at the turn clearance.

The segmental (or regional average) mass transfer coefficient was defined as

$$\overline{h}_m = \frac{\Delta M_n / \Delta t}{A_s \left(\rho_{v,w} - \overline{\rho}_{v,b}\right)} \quad \left[\frac{m}{s}\right] \tag{6}$$

where ΔM_n was the total mass transfer from the naphthalene surface of a cassette to the air, Δt was the duration of the experiment, over which air flowed steadily through the test channel. The vapor density of naphthalene at the wall, $\rho_{v,w}$, was evaluated using the ideal gas equation of state that was defined as

$$\rho_{v,w} = \frac{P_{v,w}}{R_{NP} T_w} \quad [\text{kg}/\text{m}^3]$$
(7)

where the vapor pressure-temperature correlation for naphthalene, by Ambrose et al. [39], was obtained using

$$T_w \log(P_{v,w}) = \frac{a_0}{2} + \sum_{s=1}^{3} a_s E_s(x)$$
(8)

where

$$E_1(x) = x$$
(8a)

$$E_2(x) = 2x^2 - 1$$
(8b)

$$E_3(x) = 4x^3 - 3x$$
(8c)

and

$$a_0 = 301.6247, \ a_1 = 791.4937, \ a_2 = -8.2536, \ a_3 = 0.4043$$
(8d)

where

$$x = \frac{(2T_w - 574)}{114}$$
(8e)

The average bulk vapor density of naphthalene, $\bar{\rho}_{v,b}$, was the average of the vapor densities at the upstream and downstream edges of the naphthalene surface being considered, and was calculated as

$$\bar{\rho}_{v,b} = \frac{1}{2}\left[\left(\frac{\dot{M}_n}{\dot{V}}\right)_{upstream} + \left(\frac{\dot{M}_n}{\dot{V}}\right)_{downstream}\right] \quad [\text{kg}/\text{m}^3]$$
(9)

where $\dot{M}_n$ was the rate of total mass transfer from the upstream naphthalene surfaces, and $\dot{V}$ was the air volumetric flow rate.

The local mass transfer coefficient was defined as

$$h_m = \frac{\dot{M}_n''}{\rho_{v,w} - \rho_{v,b}} = \frac{\rho_s \Delta z / \Delta t}{\rho_{v,w} - \rho_{v,b}} \quad [\text{m}/\text{s}]$$
(10)

where $\dot{M}''_n$ was the local naphthalene mass flux, ρ_s was the density of solid naphthalene, and Δz was the local change of elevation on the naphthalene surface. The local bulk vapor density, $\rho_{v,b}$, in Eq. (10) was the rate of total mass transfer from naphthalene surfaces upstream of the grid point divided by the air volumetric flow rate.

The segmental and local Sherwood numbers were defined, respectively, as

$$\overline{Sh} = \frac{\overline{h}_m D_h}{\sigma} \quad \text{and} \quad Sh = \frac{h_m D_h}{\sigma} \tag{11}$$

where σ was the mass diffusion coefficient for naphthalene vapor in the air, which was determined with a correlation given in Goldstein and Cho [40].

$$\sigma = 0.0681 \left(\frac{T}{298.16} \right)^{1.93} \left(\frac{1.013 \times 10^5}{p} \right) \times 10^{-4} \quad [m^2/s] \tag{12}$$

According to the analogy between heat transfer and mass transfer described in Eckert [41], regional average and local heat and mass transfer analogy were defined, respectively, as

$$\frac{\overline{Nu}}{Nu_0} = \frac{\overline{Sh}}{Sh_0} \quad \text{and} \quad \frac{Nu}{Nu_0} = \frac{Sh}{Sh_0} \tag{13}$$

where the reference Nusselt number and Sherwood number were based on the Dittus-Boelter correlations [42] for a fully developed turbulent flow at the same Reynolds number through a smooth channel.

$$Nu_0 = 0.023 \, \mathrm{Re}_{Dh}^{0.8} \, \mathrm{Pr}^{0.4} \tag{14}$$

$$Sh_0 = 0.023 \, \mathrm{Re}_{Dh}^{0.8} \, Sc^{0.4} \tag{15}$$

where Schmidt number, Sc, was obtained by

$$Sc = 2.28\left(\frac{T}{298.16}\right)^{-0.1526} \tag{16}$$

A friction factor based on pressure drop across turn was obtained using

$$f = \frac{(\Delta p/L)\, D_h}{\rho \bar{V}^2/2} = 2\rho\left(\frac{\Delta p}{L}\right)\left(\frac{A_c}{\dot{m}}\right)^2 D_h \tag{17}$$

where Δp was the pressure drop across the sharp turn, L was the streamwise distance between the locations of the pressure taps along the centerline of the test channel, and A_c was the channel flow cross-sectional area at the turn clearance. The experimental friction factor was normalized by the friction factor for fully developed turbulent flow at the same Reynolds number in a smooth channel, f_0, which was given in [42].

$$f_0 = \left[0.79\ln(\mathrm{Re}_{Dh}) - 1.64\right]^{-2} \tag{18}$$

The estimation of uncertainty values was based on a confidence level of 95% (or 20:1 odds) and the relative uncertainty analysis method of Coleman and Steele [43]. Also, in all uncertainty calculations, uncertainty values of 1.0% for all properties of air and 0.25 *mm* for all physical dimensions were used.

The uncertainty of the air mass flow rate was calculated from the uncertainties of the measured pressures at the orifice flow meter, and was found to be 2.9%. The maximum uncertainty of the calculated Reynolds number was 3.1%.

Using uncertainty values of 1.0% for the density of solid naphthalene and the uncertainty of the measured values of Δz, the uncertainty of the local mass transfer coefficient was estimated to be 10.9%. Similarly, using the uncertainty of the measured values of ΔM_n, the uncertainty of the average mass transfer coefficient was estimated to

be 7.7%. According to Goldstein and Cho [40], the diffusion coefficient of naphthalene vapor in air had an uncertainty of about 2.0%. With this value, the calculated values of the relative uncertainties for the local and average Sherwood numbers were 11.1% and 8.0%, respectively.

Using the maximum uncertainty values of 4.0% for the measured pressure drops and 2.9% for the air mass flow rate, the maximum value of the relative uncertainty of the friction factor was calculated to be 7.8%.

2.4 PRESENTATION AND DISCUSSION OF RESULTS

In this section, the distributions of the local and regional average mass transfer coefficient at the 180° turn and along the test channel are presented. The detailed distributions are based on the measurements of the local elevations at a grid of 3,776 points on the naphthalene surface (and on the top surface of the rim) of the U-shaped cassette on the bottom wall at the turn [see Fig. 5(e)]. The results are presented as contours of constant Sh/Sh_0 values, for air entering the test channel through the smaller trapezoidal straight section and through the larger trapezoidal straight section, for the test channel with all smooth walls and with transverse ribs on two opposite walls, and for four Reynolds numbers. The variations of the regional average mass transfer coefficient along the test channel are based on the weighing of the sixteen naphthalene cassettes

[see Fig. 5(c)]. The regional average results are presented as variations of $\overline{Sh}/Sh_0$ along sixteen segments of the bottom wall of the test channel, for air entering the test channel through the smaller straight section and through the larger straight section, for the test channel with all smooth walls, and with transverse ribs on the bottom wall only and on both the top and bottom walls, and for four Reynolds numbers. According to the heat and mass transfer analogy [Eq. (13)], the local and regional average distributions give the distributions of the respective Nusselt numbers for airflows through the two-pass trapezoidal channel relative to those for fully developed turbulent flows of air through a smooth straight channel at the same Reynolds numbers.

The results of this study are reported in this section for four nominal Reynolds numbers. The actual values of the Reynolds numbers deviate from the respectively nominal values by a maximum of ±2.9%.

The results of Sh/Sh_0 were validated with both the obtained $\overline{Sh}/Sh_0$ of the U-shaped naphthalene cassette by weighing the U-shaped cassette and the results of streamwise variations of $\overline{Sh}/Sh_0$ obtained with the sixteen naphthalene cassettes. The results of regional average and local mass transfer distributions were again validated with the well-known results of the turn in a square channel.

2.4.1 Validation of Results of Local Mass Transfer Distributions

To validate the results of local mass transfer distributions, $\overline{Sh}/Sh_0$ that were obtained by averaging Sh/Sh_0 of the total measured elevations on the mass transfer active surface of the U-shaped cassette were compared with $\overline{Sh}/Sh_0$ that were obtained from weighing the U-shaped cassette before and after the experiments. The estimated area-weighted $\overline{Sh}/Sh_0$ from Sh/Sh_0 were in very good agreement with $\overline{Sh}/Sh_0$ obtained from
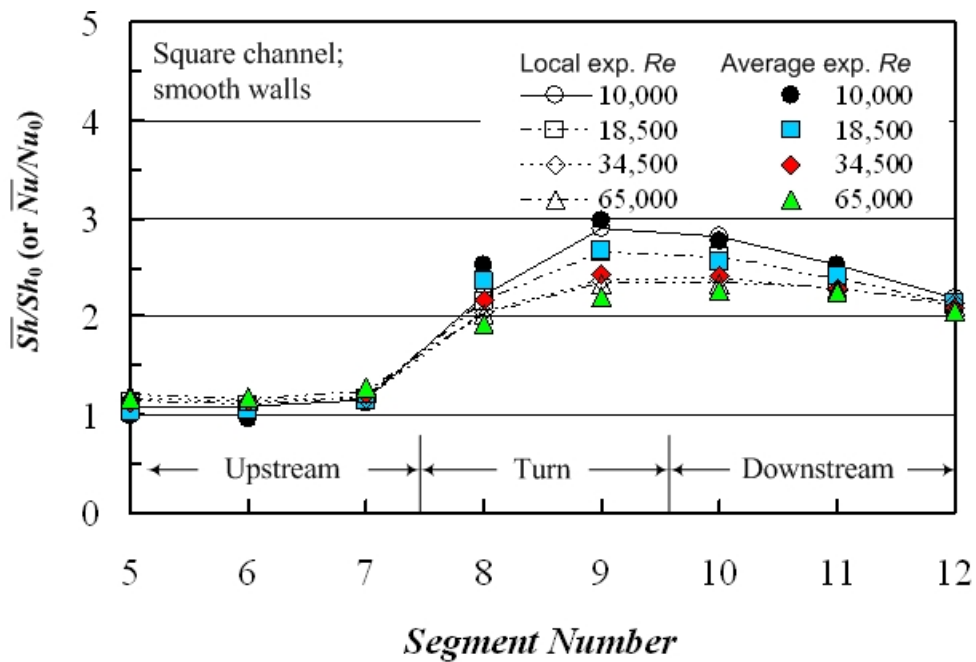
(a) Square channel with smooth walls

Fig. 10 Comparisons of the area-weighted regional averages of the local mass transfer coefficients with the results of the regional average mass transfer coefficients
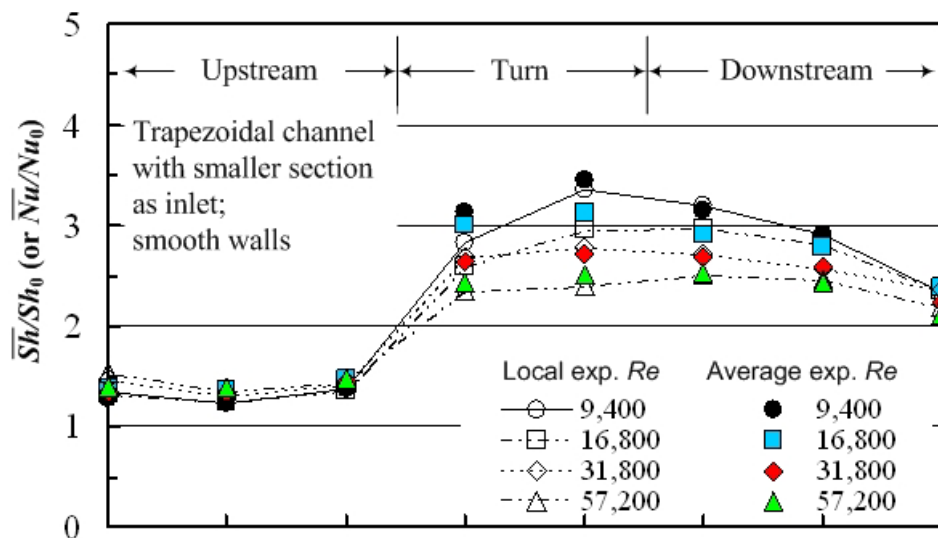
(b) Trapezoidal channel with smooth walls, air entering smaller straight section
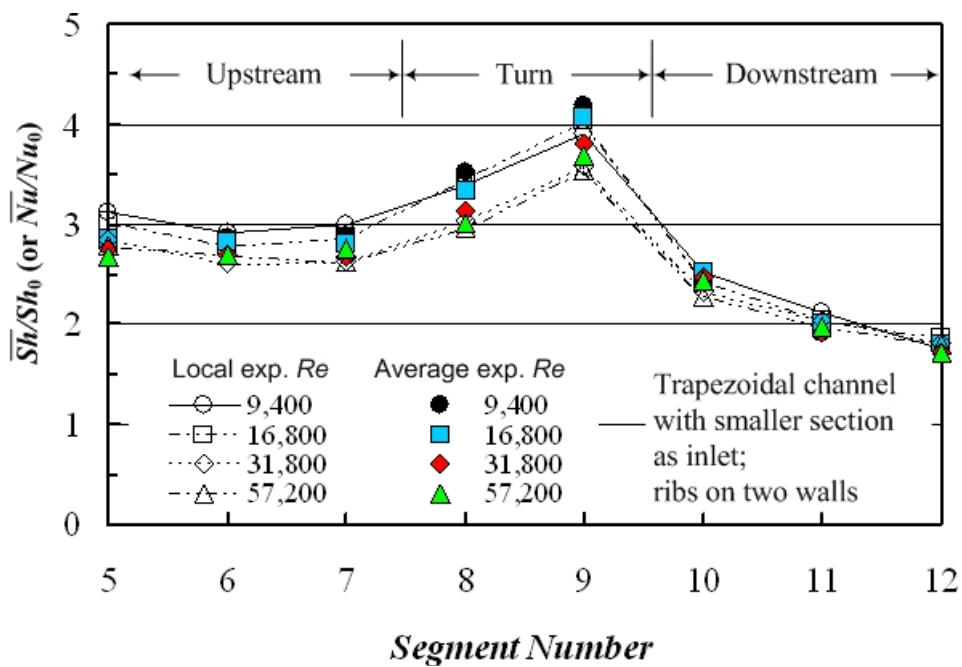
(c) Trapezoidal channel with ribs on two walls, air entering smaller straight section
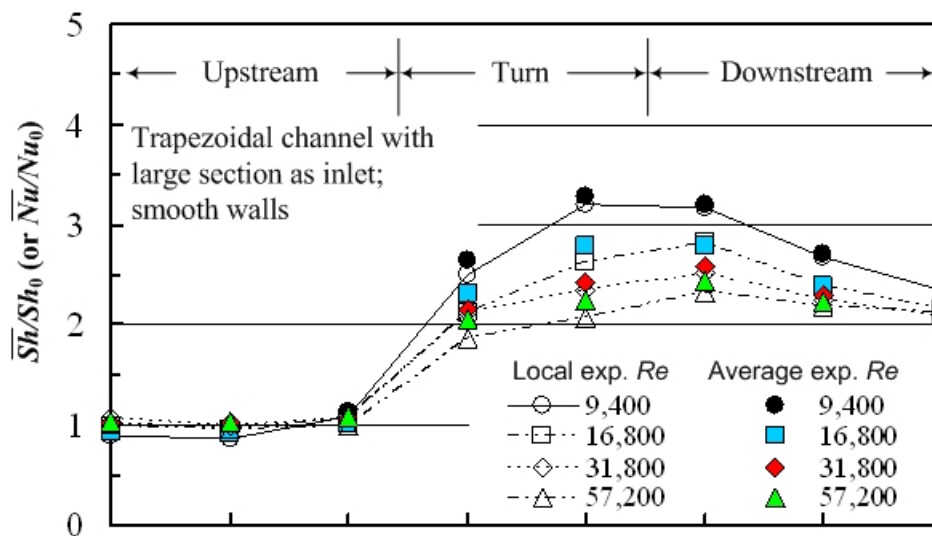
Fig. 10 (continued)

(d) Trapezoidal channel with smooth walls, air entering larger straight section
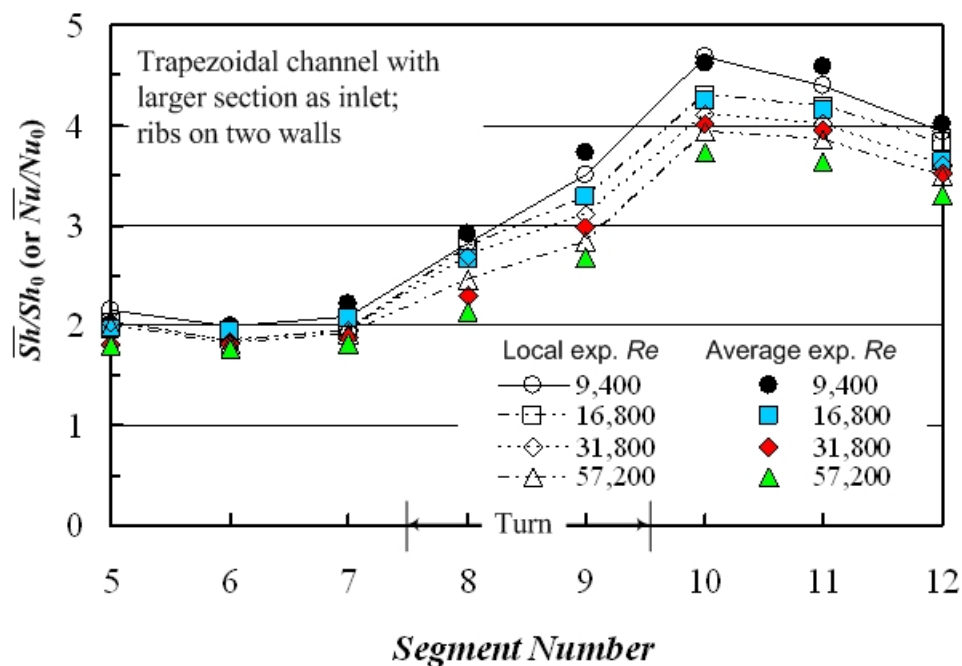
(e) Trapezoidal channel with ribs on two walls, air entering larger straight section

Fig. 10 (continued)

Table 1   Maximum and average errors of the sixteen area-weighted regional average mass transfer coefficients obtained from the results of the local mass transfer experiments compared with the sixteen regional average mass transfer results

Case	Square channel	Trapezoidal channel			
		Air through smaller section		Air through larger section	
Wall roughness	Smooth	Smooth	Ribs on two walls	Smooth	Ribs on two walls
Max. Error	13.0 %	13.7 %	11.0 %	9.3 %	17.5 %
Ave. Error	3.7 %	3.7 %	3.9 %	3.9 %	5.0 %

the weight measurement of the U-shaped cassette with a maximum error of 8.0%. With the confidence of the results of the local mass transfer experiments, point-by-point local mass transfer coefficients of one mass transfer active surface of the U-shaped cassette were averaged to have the eight streamwise regional average mass transfer coefficients that were consistent with the results of the regional average mass transfer experiments in size and locations, to be compared with the regional average mass transfer experiment results, as shown in Fig. 10. The area-weighted eight regional average mass transfer coefficients were also in good agreement with the results of the regional average mass transfer experiments. Table 1 shows maximum and average errors of the area-weighted eight regional average mass transfer coefficients obtained from the local mass transfer

experiments based on the regional average mass transfer experiment results. Although maximum errors were 17.5%, average errors of the eight averaged mass transfer coefficients of the local mass transfer experiments were in very good agreement with the results of the regional average mass transfer experiments with maximum error of 5.0%. The reason of the highest discrepancy with the results of the regional average mass transfer experiments may be discrepancy of the flow condition on the entrance of cassettes at the bottom wall of the test channel; discrepancy of very thin rim of the entrance region between the cassette for regional average mass transfer experiments and the U-shaped cassette for the local mass transfer experiments. Except the entrance region, the local mass transfer experiment results were in very good agreement with the regional average mass transfer results, as shown in Fig. 10.

Although experimental method of the local mass transfer results were validated with regional average mass transfer results, regional average and local mass transfer results should be also validated with the well-known results of square channels.

(a) $Re \cong 10,000$

(b) $Re \cong 18,500$
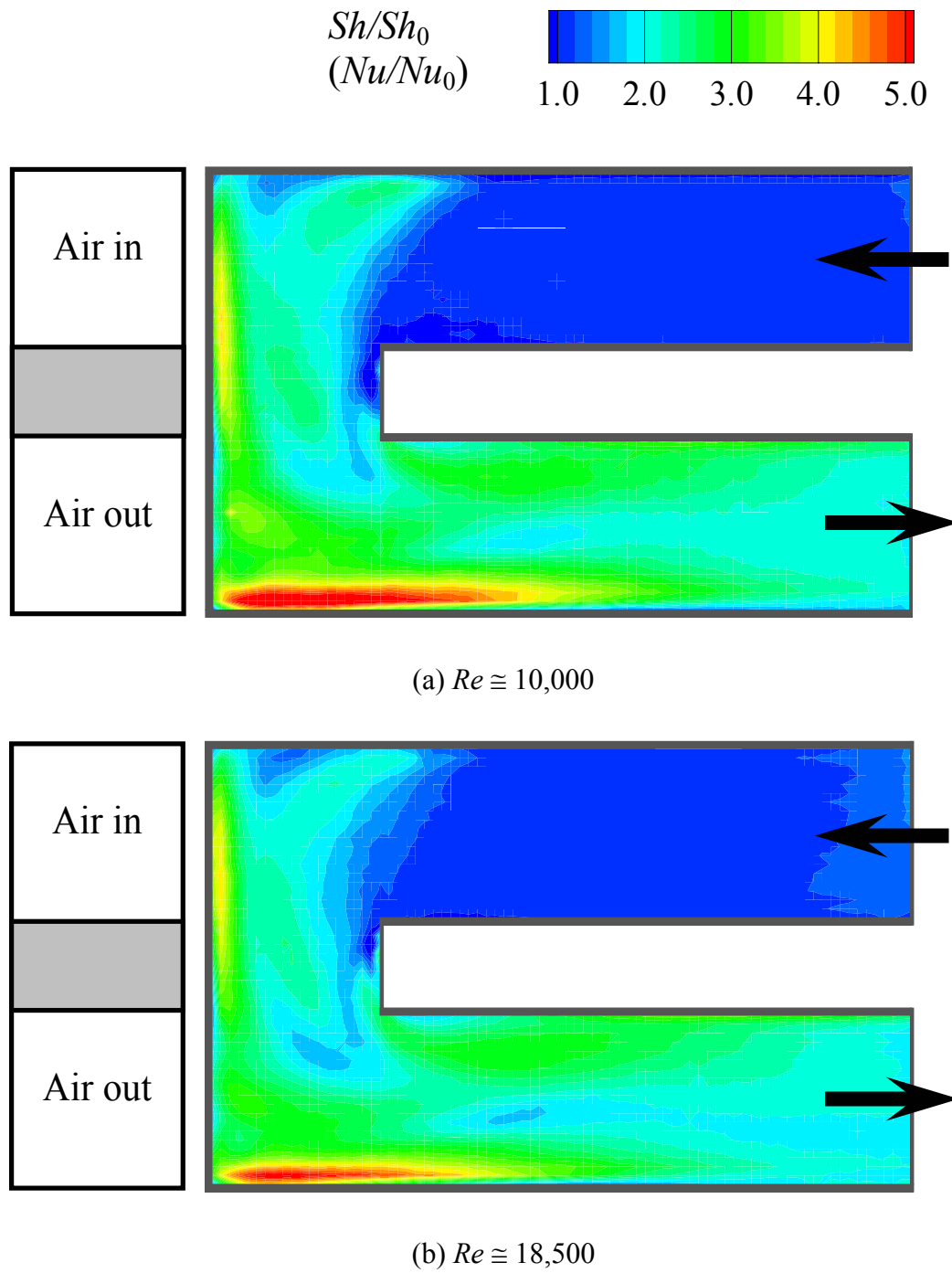
Fig. 11 Local mass transfer distributions at sharp turn in square channel with smooth walls
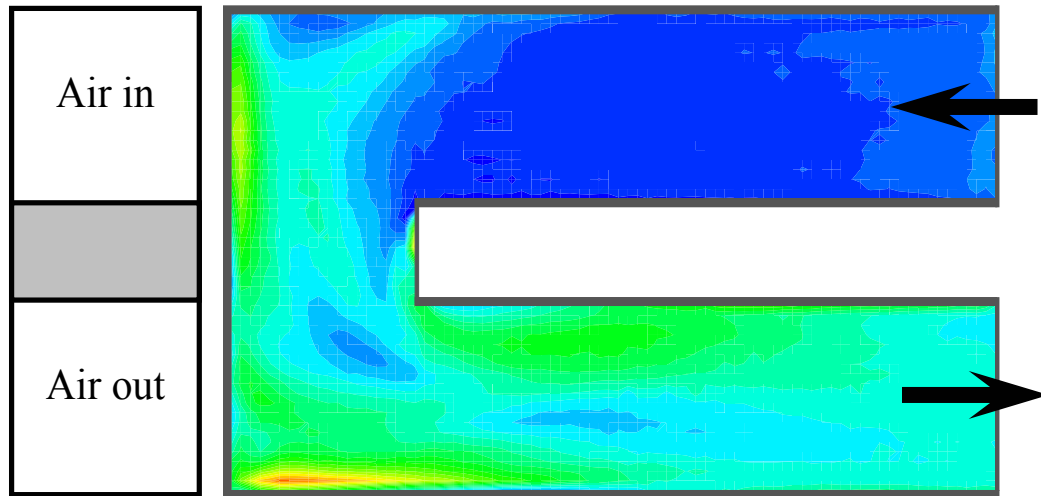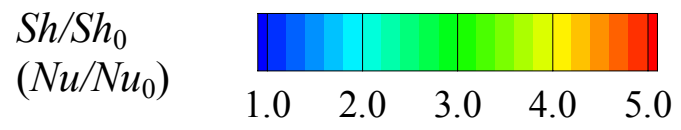
(c) $Re \cong 34,500$
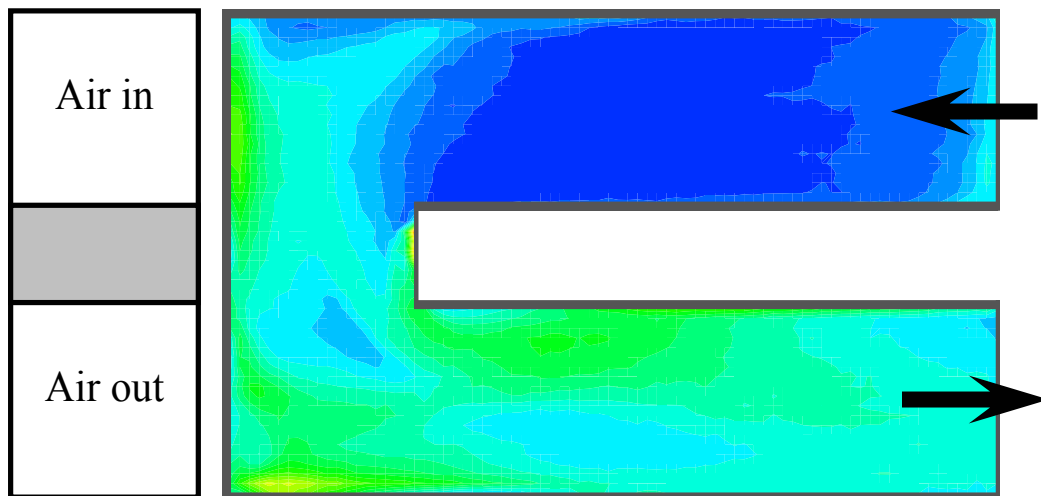
(d) $Re \cong 65,000$

Fig. 11 (continued)

2.4.2 Mass Transfer Distributions for Square Channel with Smooth Walls

As mentioned earlier, local and regional average mass transfer results were obtained for air flow through a two-pass 3.81-*cm* square channel to validate the experimental method. Fig. 11 gives the local mass transfer distributions at the turn on the bottom wall of the 3.81-*cm* square channel for four different Reynolds numbers between 10,000 and 65,000. As expected, the highest and lowest Sh/Sh_0 are obtained at lowest Reynolds number of 10,000 and 65,000, respectively. Because the Sh/Sh_0 distributions are quite similar to one another, the shape of the local mass transfer distribution at the turn is not significantly affected by varying the air mass flow rate. The Sherwood number ratio is low and is almost constant, with a value of about 1.0, near the end of the straight section upstream of the turn, and increases along the main flow direction in the turn, with higher values near the outer walls and lower values near the tip of the divider wall in the turn. The ratio remains quite high downstream of the turn, and then it decreases further downstream along the second straight section as the flow redevelops. The mass transfer is high at the base of the upstream half of the end wall as the flow is deflected from the end wall onto the bottom wall. When the flow is pushed by centrifugal forces at the turn toward the downstream outer wall and is then deflected onto the bottom wall, the mass transfer on the bottom wall is very high along the downstream outer wall. A low mass transfer region near the upstream outer wall in the turn is the result of flow recirculation, as the flow is deflected from the end wall and turns downstream around the tip of the divider wall.

The vigorous mixing at the turn increases the turbulence in the flow and causes the mass transfer to be high over a large portion of the bottom wall in the turn and downstream of the turn. A distinctive relatively low mass transfer region between the downstream inner and outer edges of the turn may be caused by the interaction between the separated flow from the upstream edge of the divider wall and the deflected flow from the end wall toward the bottom wall. A third region of relatively high mass transfer is observed near a rather small region of slightly lower mass transfer just downstream of the tip of the divider wall. This mass transfer distribution along the downstream side of
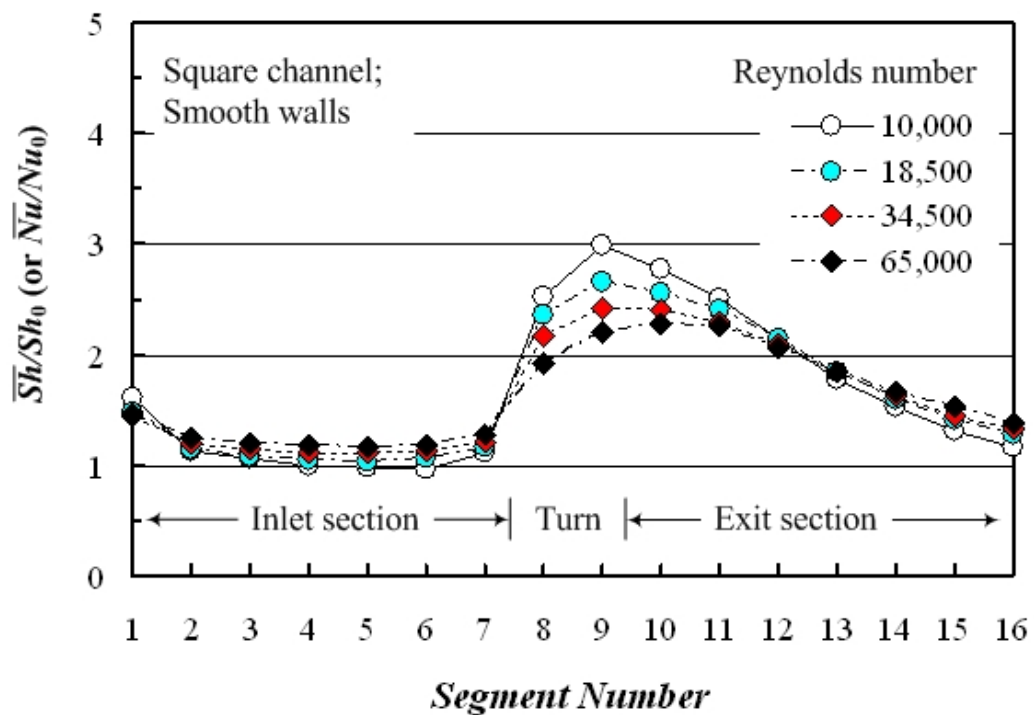
Fig. 12 Segmental mass transfer distributions along square channel with smooth walls

the divider wall may be the result of the separation of the flow at the downstream edge of the tip of the divider wall and the reattachment of the flow onto the downstream side of the divider wall and the bottom wall. Downstream of the turn, the Sh/Sh_0 value is higher near the inner and outer walls and is lower in the middle of the bottom wall. The Sh/Sh_0 distribution may suggest that there is a pair of counter-rotating vortices (of two different sizes that may change along the downstream straight section) over the bottom wall as the flow enters the downstream straight section of the channel.

The development of the flow in the upstream straight (inlet) section, the increase of the mass transfer in the turn, and the redevelopment of the flow in the downstream straight (exit) section are evident in the streamwise distributions of the segmental of regional average Sherwood number ratio given in Fig. 12. In the turn, the $\overline{Sh}/Sh_0$ values are larger on wall segment no. 9 than on wall segment no. 8, and the $\overline{Sh}/Sh_0$ values on both wall segments are larger when the Reynolds number is smaller. The Sh/Sh_0 and $\overline{Sh}/Sh_0$ distributions in Figs. 11 and 12 compare very well with and have all of the features of those at the 180° turns of square channels with smooth walls presented in [5] and [8].

2.4.3 Mass Transfer Distributions for Trapezoidal Channel with Smooth Walls

In Figs. 13 and 14, the local mass transfer distributions at the turn on the smooth bottom wall of the trapezoidal channel are presented, for air flow entering the smaller straight section and for air flow entering the larger straight section, respectively. In each figure, the four local mass transfer distributions are for $Re \approx$ 9,400, 16,800, 31,800, and 57,200. For either flow direction, the shape of the Sh/Sh_0 distribution at the turn is again not significantly affected by varying the air mass flow rate. Also, as in the square channel case, the Sh/Sh_0 value is low in the inlet section, is high near the end wall and the downstream outer wall in the turn, and is low in two regions near the upstream outer wall and the downstream edge of the divider wall in the turn.

Comparing Figs. 13 and 14, it is evident that the Sh/Sh_0 value upstream of the turn is higher for air flow entering the smaller trapezoidal straight section than for air flow entering the larger trapezoidal straight section. This is due to the higher velocities of the flow in the inlet section with the smaller flow cross sectional area. Note that the Reynolds number is based on the hydraulic diameter at the turn clearance. The higher velocities of the flow that enters the turn from the smaller inlet section cause the mass transfer on the bottom wall to be higher along the base of almost the entire end wall, as the flow with a larger momentum impinges onto the end wall. A close examination of corresponding Sh/Sh_0 distributions for the same Reynolds numbers shows that the mass transfer is higher everywhere on the upstream half of the bottom wall in the turn in the case of air flow entering the smaller inlet section. Even as the flow cross section
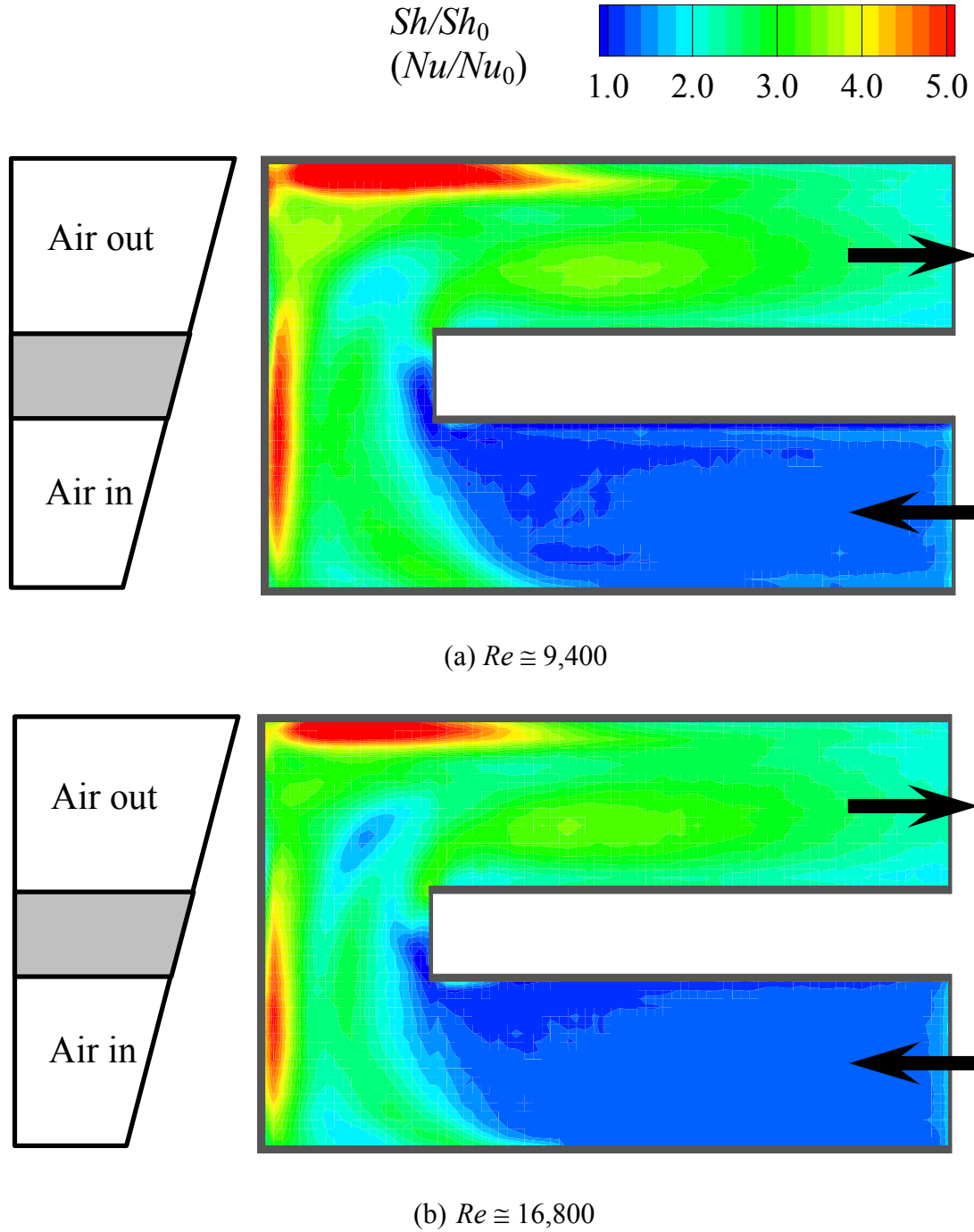
Sh/Sh_0
(Nu/Nu_0)

1.0   2.0   3.0   4.0   5.0

(a) $Re \cong 9,400$

(b) $Re \cong 16,800$

Fig. 13   Local mass transfer distributions at sharp turn in trapezoidal channel with smooth walls and air entering smaller straight section

Sh/Sh_0
(Nu/Nu_0)

1.0   2.0   3.0   4.0   5.0

Air out

Air in

(a) $Re \cong 31,800$

Air out

Air in

(c) $Re \cong 57,200$

Fig. 13 (continued)

Sh/Sh_0
(Nu/Nu_0)

1.0   2.0   3.0   4.0   5.0

Air in

Air out

(a) $Re \cong 9,400$

Air in

Air out

(d) $Re \cong 16,800$
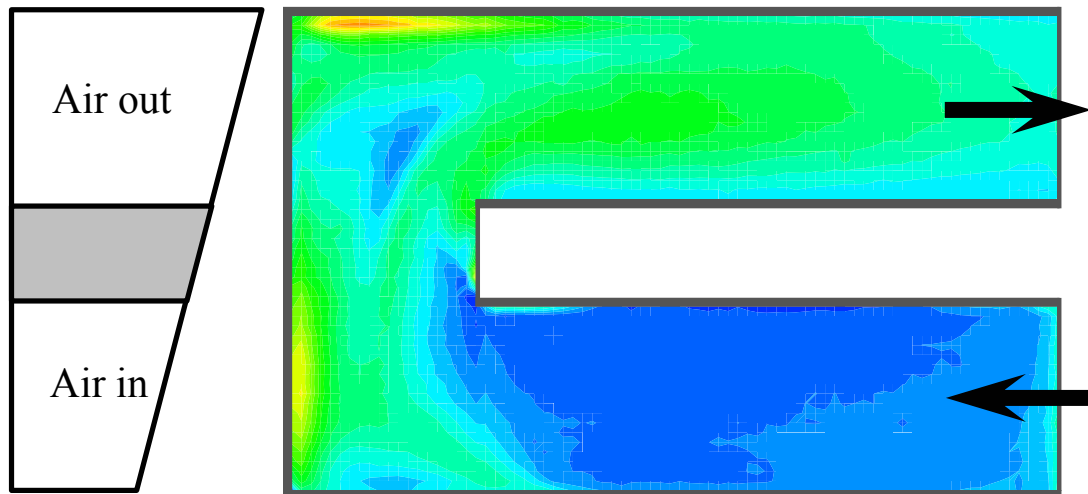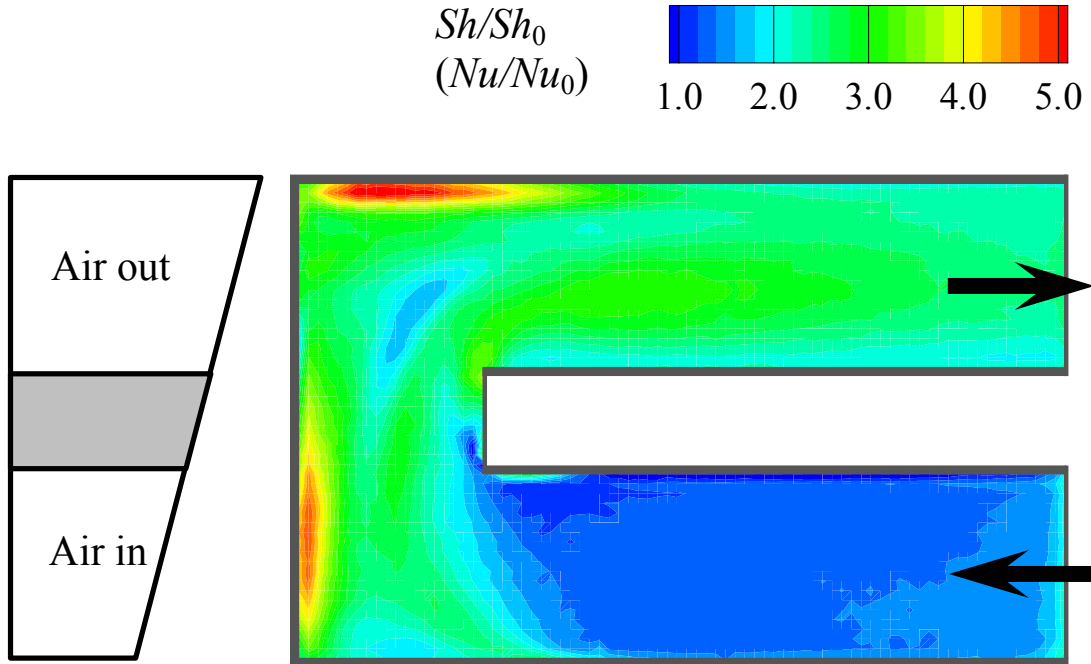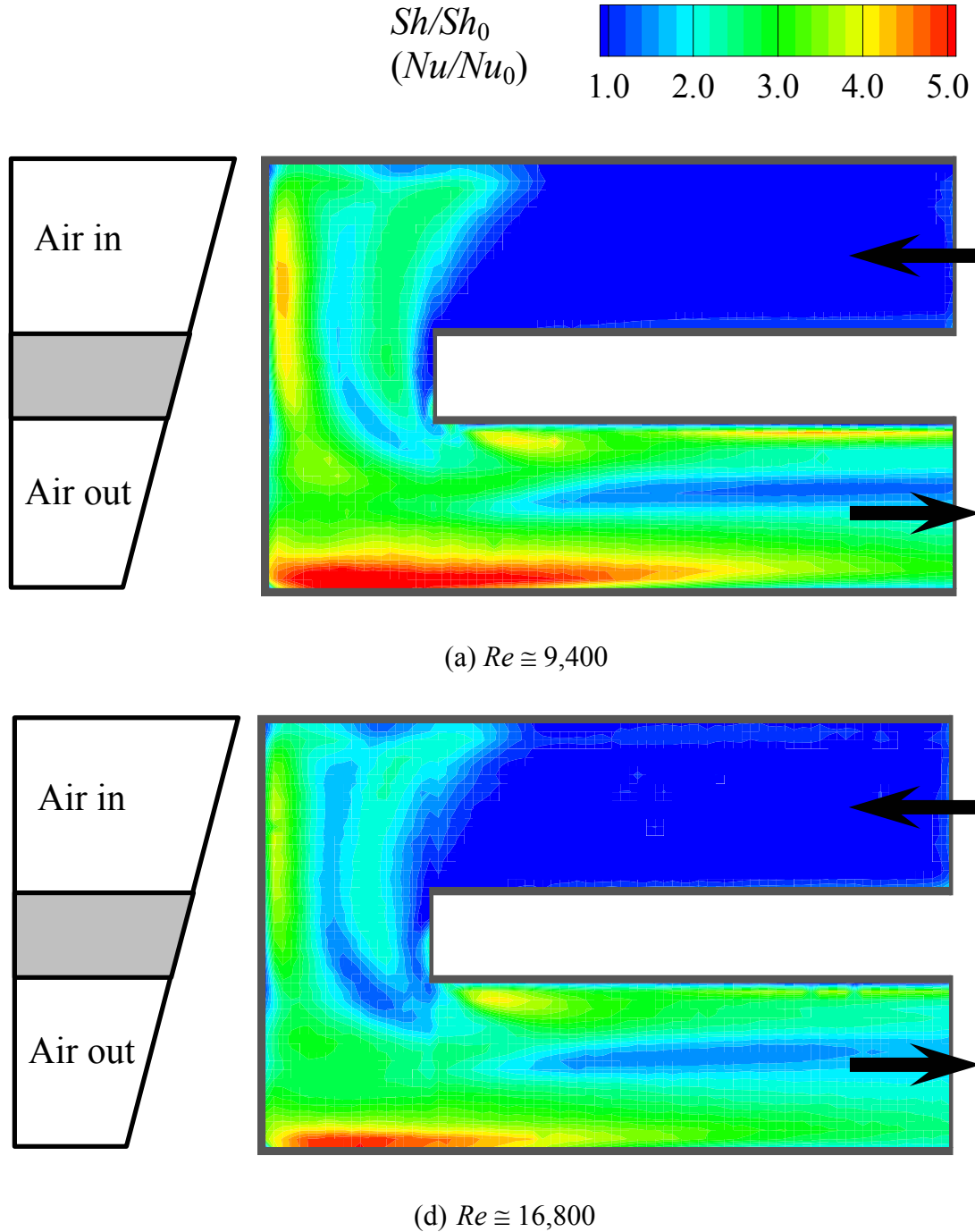
Fig. 14   Local mass transfer distributions at sharp turn in trapezoidal channel with smooth walls and air entering larger straight section

(a) $Re \cong 31,800$
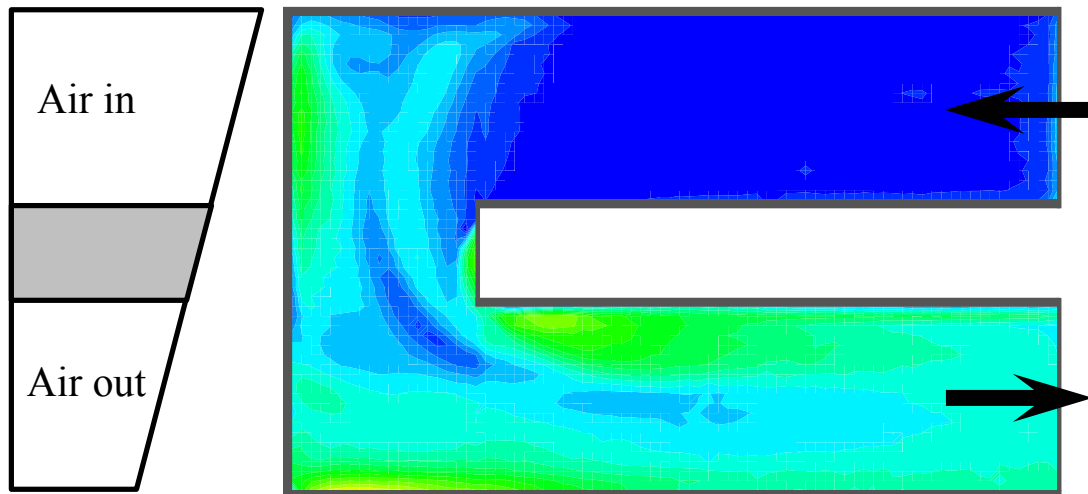
(e) $Re \cong 57,200$

Fig. 14 (continued)

increases in the turn, the larger momentum of the flow from the smaller inlet section and the increase of the turbulence in the turn still cause the mass transfer to be higher on the downstream half of the bottom wall in the turn than for the accelerating flow entering the turn from the larger inlet section. The differences in the Sh/Sh_0 values, however, are smaller on the downstream half of the bottom wall than on the upstream half.

Figure 13 shows that, downstream of the turn in the larger exit section, the mass transfer remains quite high on the bottom wall, with the mass transfer decreasing along the outer wall and the lowest Sh/Sh_0 values along the downstream side of the divider wall. After a length of about three times the channel width downstream of the turn, the Sh/Sh_0 value decreases to about 2.0.

In the case of the flow entering the larger inlet section, the mass transfer is higher near the downstream outer wall in the turn than near the end wall. As shown in Fig. 14, the difference between the Sh/Sh_0 values in these two high mass transfer regions is larger when the Reynolds number is smaller. The flow enters the turn from the larger inlet section with relatively low velocities, and accelerates around the turn as the flow cross section is reduced in the turn. Downstream of the turn in the smaller exit section, the mass transfer is lower in the middle of the bottom wall than along the outer wall and along the downstream side of the divider wall. The Sh/Sh_0 distributions downstream of the turn are similar to those for the square channel, except that the accelerating flow in the turn appears to strengthen a pair of counter-rotating vortices over the bottom wall, causing the high Sh/Sh_0 values along the two side walls and very low values (as low as about 1.4 for $Re \cong 9,400$) in the middle of the bottom wall.
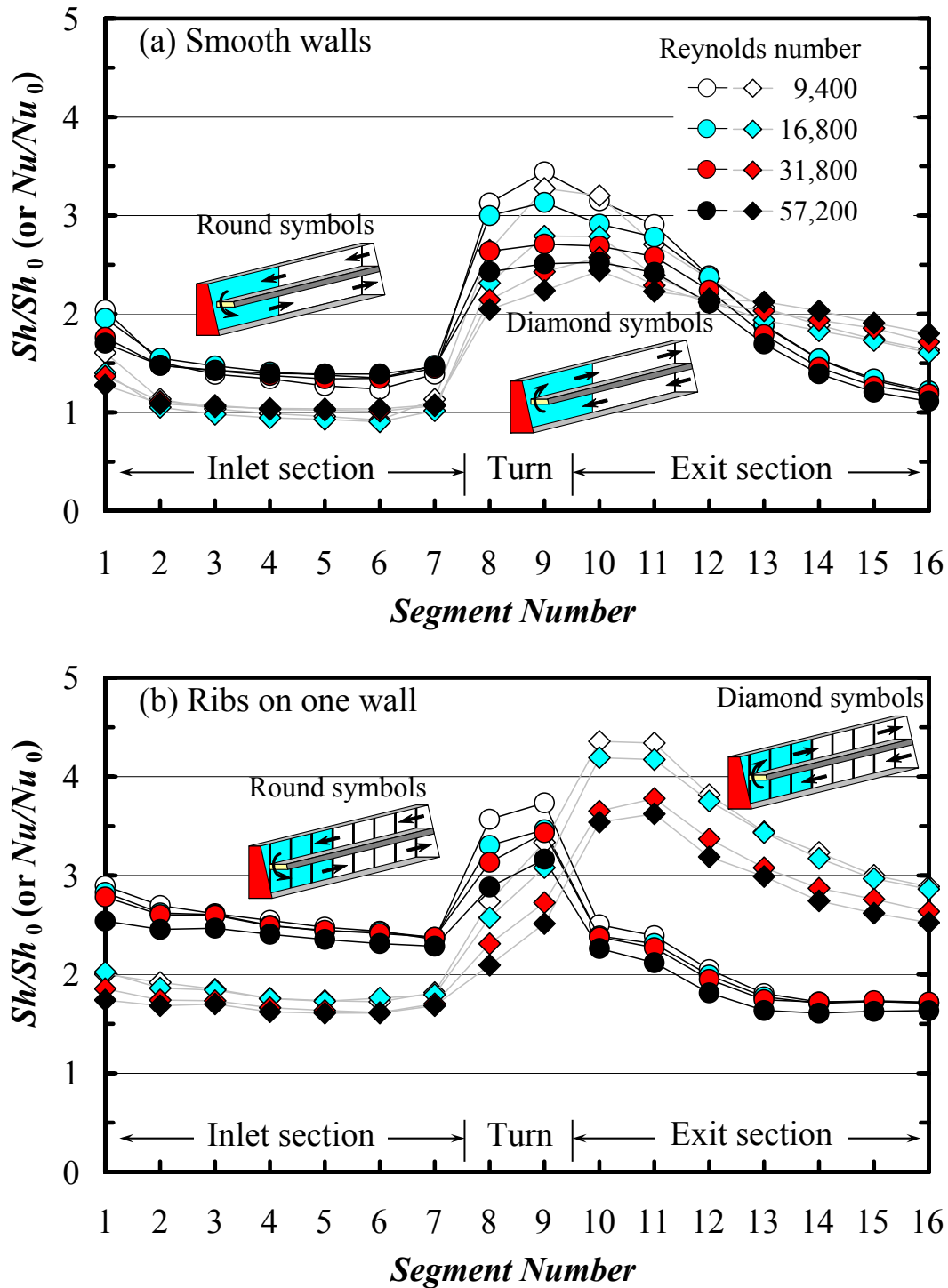
Fig. 15 Segmental mass transfer distributions along trapezoidal channel:

(a) with smooth walls, (b) with ribs on one wall, and (c) with ribs on two opposite walls
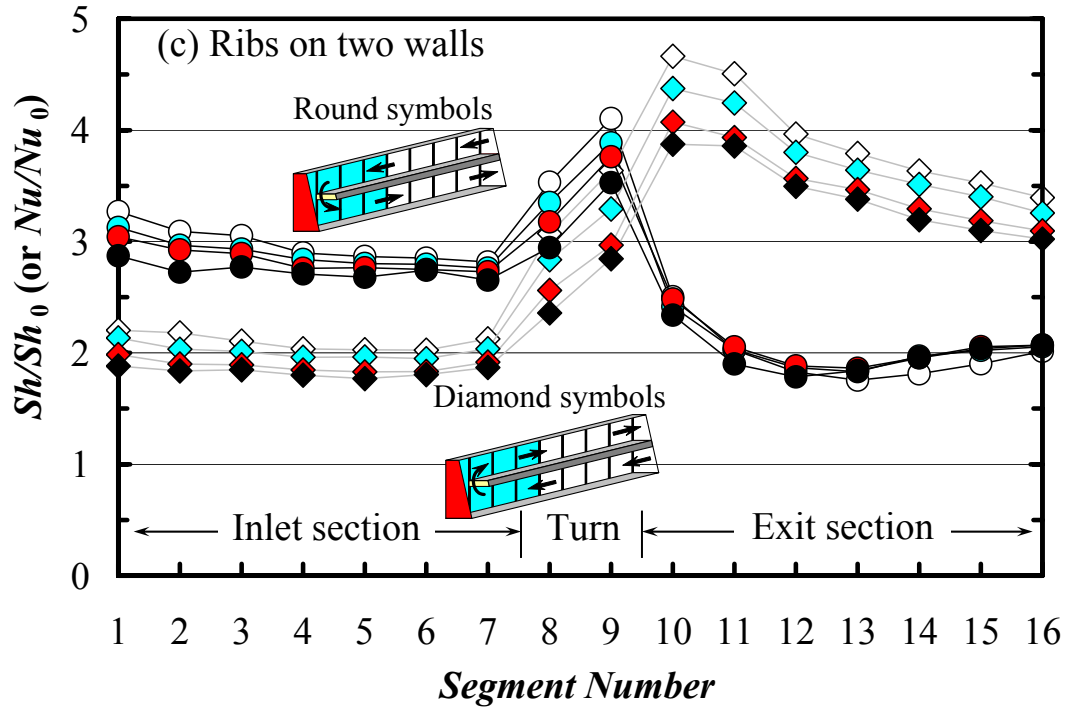
Fig. 15 (continued)

Figure 15 compares the streamwise distributions of the regional average Sherwood number ratio along the trapezoidal channel for air flow entering the smaller straight section (round symbols in the figure) and those for air flow entering the larger straight section (diamond symbols). For the trapezoidal channel with smooth walls [Fig. 15(a)], the $\overline{Sh}/Sh_0$ distributions are higher in the smaller inlet section, but are lower far downstream of the turn in the larger exit section. In the turn, the $\overline{Sh}/Sh_0$ value is higher on wall segment no. 9 than on wall segment no. 8, higher in the smaller inlet section case

than in the larger inlet case, and is higher when the Reynolds number is smaller (lighter symbols for smaller Reynolds numbers and darker symbols for larger Reynolds numbers). Downstream of the turn, $\overline{Sh}/Sh_0$ decreases along the streamwise direction, with slightly higher values on wall segments 10 and 11 for air flow entering the smaller straight section, but $\overline{Sh}/Sh_0$ decreases with a steeper slope because the velocities of the flow are smaller in the larger downstream straight section. The regional average mass transfer is the highest on the downstream wall segment (segment no. 9) in the turn, except when $Re \cong 57,200$, in which case $\overline{Sh}/Sh_0$ is the highest on segment no.10, as Fig. 15(a) shows that the peaks of the $\overline{Sh}/Sh_0$ distributions occur at segment no. 9 or no. 10.

2.4.4 Mass Transfer Distributions for Trapezoidal Channel with Ribs on One Wall or on Two Opposite Walls

For two sets of experiments, regional average mass transfer was determined on sixteen segments of the bottom wall with transverse ribs on the bottom, and with or without aligned transverse ribs on the top wall, as shown in Fig. 7. As described earlier, these ribs were 3.2 *mm* by 3.2 *mm* square balsa wood stripes, they were installed along the downstream edges of the sixteen naphthalene cassettes, and their surfaces exposed to the air flow were mass transfer inactive. Figs. 15(b) and 15(c) compare the $\overline{Sh}/Sh_0$

distributions for air flow entering the smaller straight section (round symbols) and those for air flow entering the larger straight section (diamond symbols), with ribs on the bottom wall only and with ribs on both the top and bottom walls, respectively. With the ribs periodically interrupting the boundary layers on the bottom wall, the $\overline{Sh}/Sh_0$ value is larger than 1.0 everywhere along the two straight sections of the trapezoidal channel.

In the channel with ribs on the bottom wall only, Fig. 15(b) shows that the $\overline{Sh}/Sh_0$ value is about 2.4 in the smaller inlet section, and about 1.7 in the larger inlet section immediately upstream of the turn. As in the channel with smooth walls, the mass transfer in the turn is higher in the smaller inlet case than in the larger inlet case. For both flow directions, the $\overline{Sh}/Sh_0$ values in the turn are again higher on the downstream wall segment (segment no. 9) than on the upstream wall segment (segment no. 8). Downstream of the turn in the larger exit section, as the flow redevelops, $\overline{Sh}/Sh_0$ decreases with an increasing (less negative) slope until it reaches a value of about 1.7, which is about the same as the $\overline{Sh}/Sh_0$ value in the larger inlet section immediately upstream of the turn. Downstream of the turn in the smaller exit section, $\overline{Sh}/Sh_0$ increases to values between 3.5 and 4.4, much higher than those in the turn, on wall segment nos. 10 and 11, before it decreases to values between 2.5 and 2.9 at the channel exit.

Sh/Sh_0
(Nu/Nu_0)

1.0   2.5   4.0   5.5   7.0
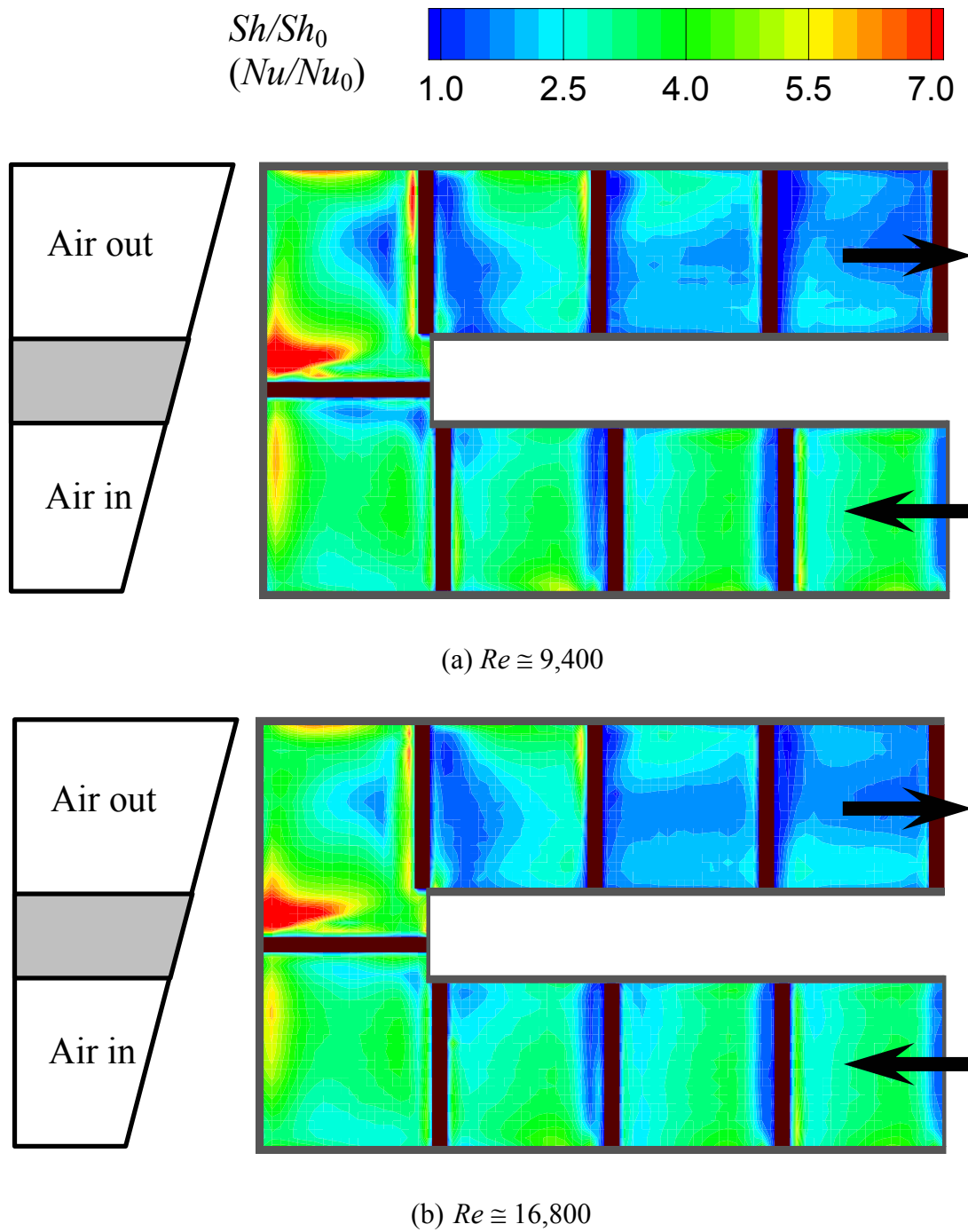
(a) $Re \cong 9{,}400$

(b) $Re \cong 16{,}800$

Fig. 16 Local mass transfer distributions at sharp turn in trapezoidal channel with ribs on two walls and air entering smaller straight section
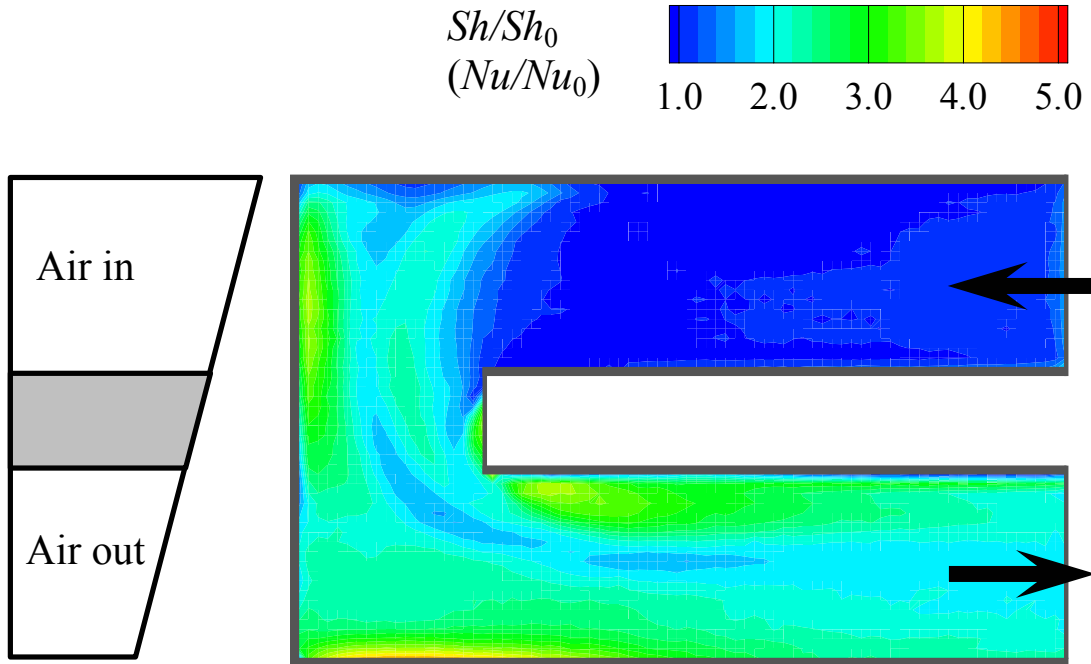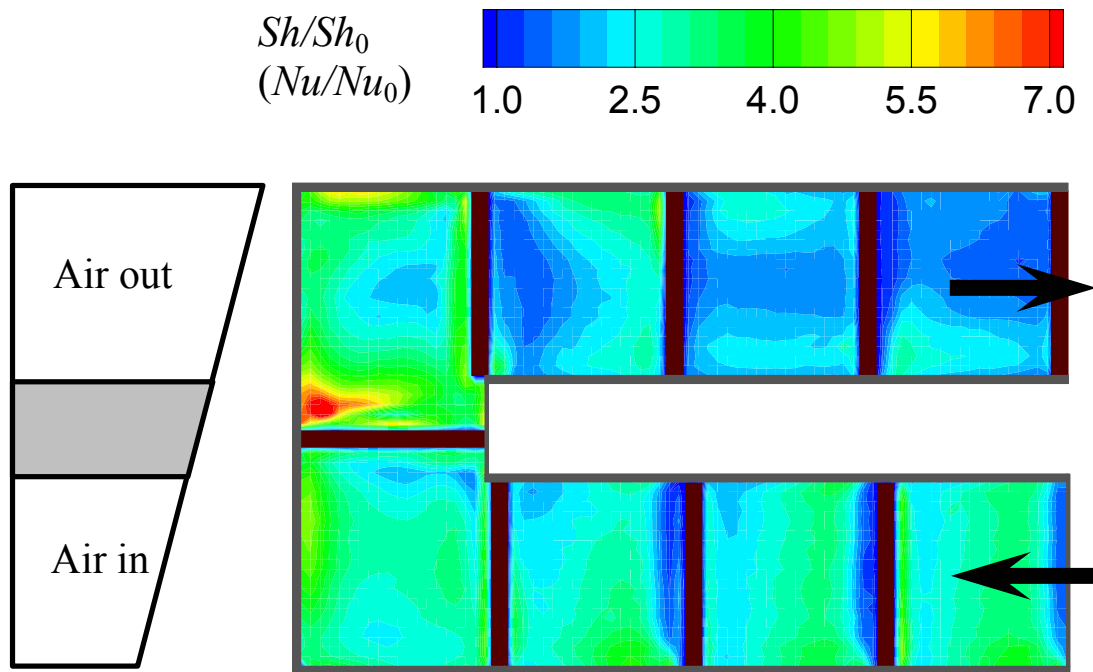
(c) $Re \cong 31,800$
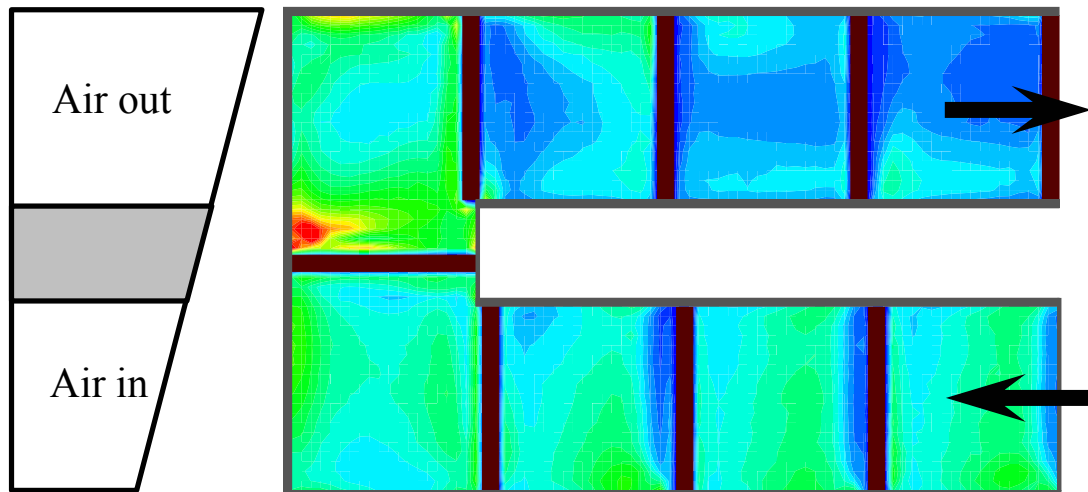
(d) $Re \cong 57,200$

Fig. 16 (continued)

Sh/Sh_0
(Nu/Nu_0)

1.0   2.5   4.0   5.5   7.0

Air in

Air out

(a) $Re \cong 9,400$

Air in

Air out
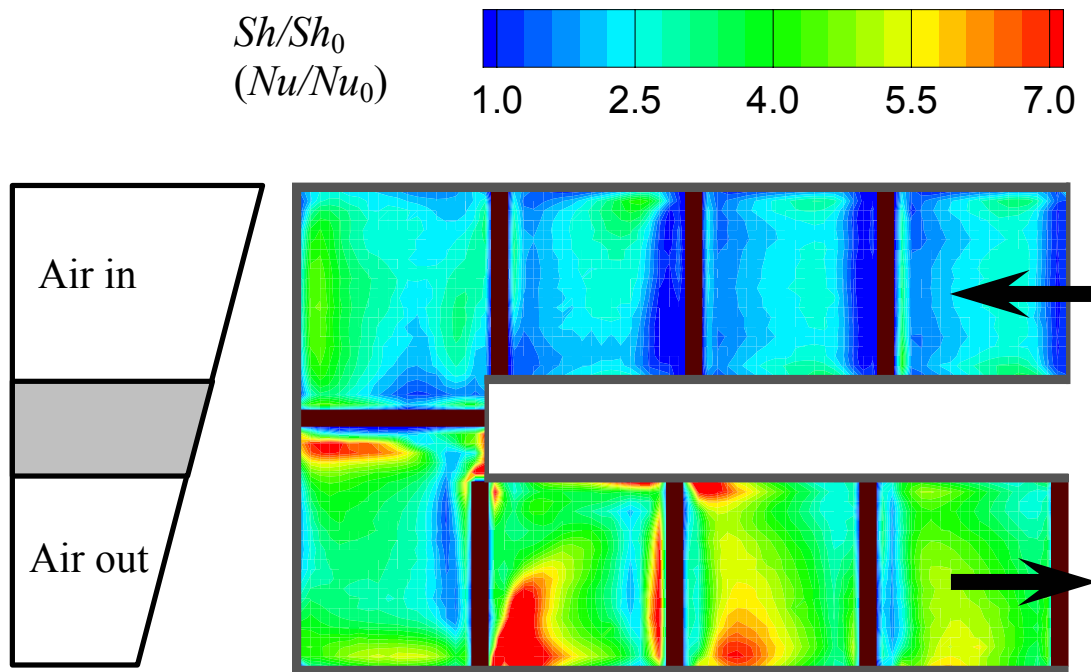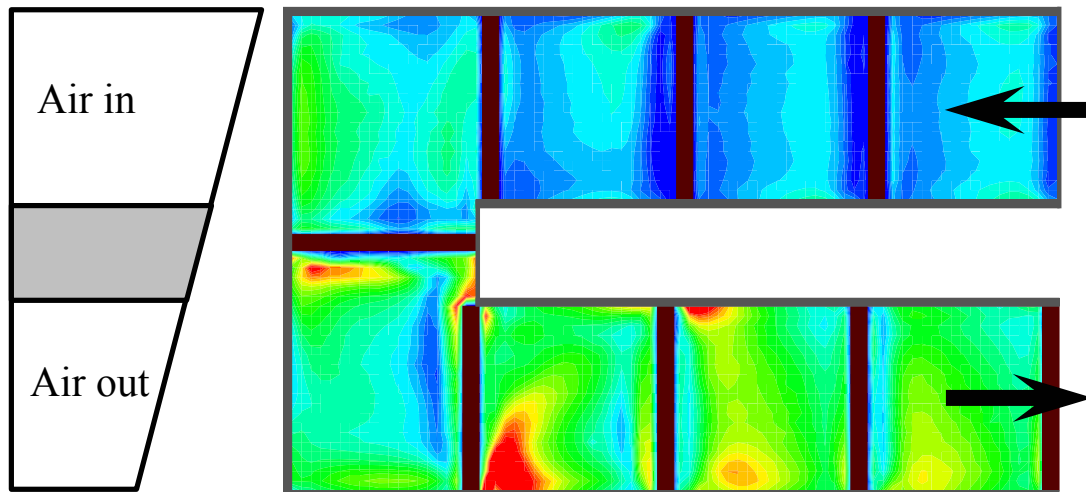
(a) $Re \cong 16,800$

Fig. 17 Local mass transfer distributions at sharp turn in trapezoidal channel with ribs on two walls and air entering larger straight section
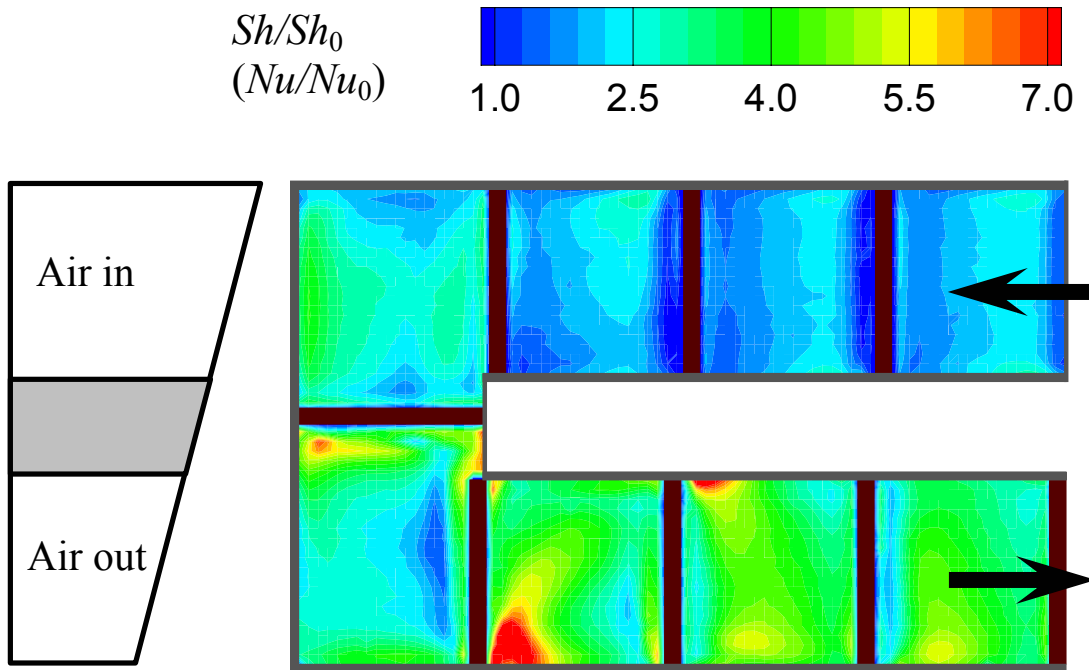
Sh/Sh_0
(Nu/Nu_0)

(c) $Re \cong 31{,}800$
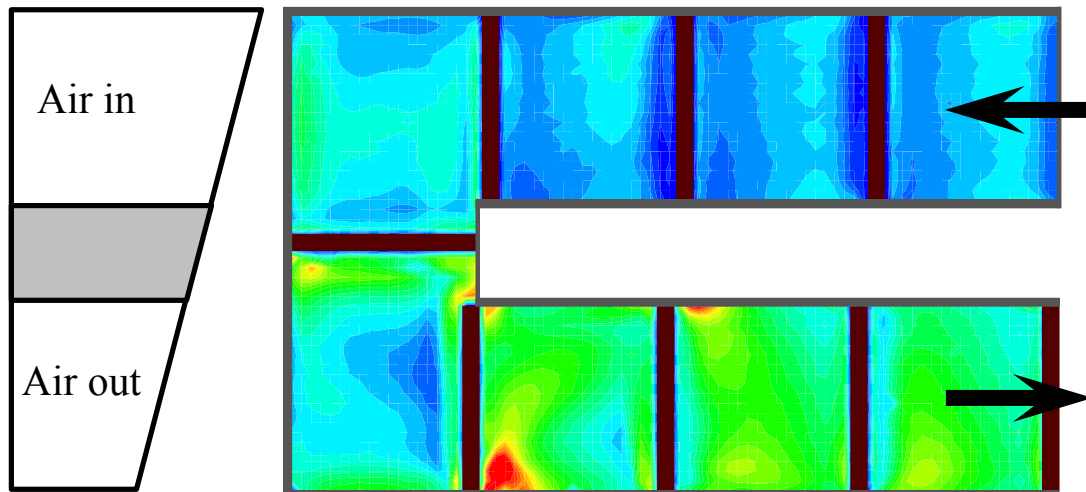
(d) $Re \cong 57{,}200$

Fig. 17 (continued)

The $\overline{Sh}/Sh_0$ distributions along the channel with ribs on both the top and bottom walls are similar to, but are higher than, those along the channel with ribs on the bottom wall only. Fig. 15(c) shows that the $\overline{Sh}/Sh_0$ value is about 2.7 in the smaller inlet section, and about 2.0 in the larger inlet section immediately upstream of the turn of the channel with ribs on both the top and bottom walls. Again, the mass transfer in the turn is higher in the case of the smaller inlet section than in the case of the larger inlet section, with higher mass transfer in the downstream half of the turn than in the upstream half of the turn in both cases. Downstream of the turn in the larger exit section, $\overline{Sh}/Sh_0$ decreases abruptly to values between 1.8 and 2.0, while downstream of the turn in the smaller exit section, $\overline{Sh}/Sh_0$ increases to values as high as almost 4.7 before it decreases to values between 3.0 and 3.4 at the channel exit.

In Figs. 16 and 17, the local mass transfer distributions at the turn on the bottom wall of the trapezoidal channel with ribs on both the top and bottom walls are presented, for air flow entering the smaller straight section and for air flow entering the larger straight section, respectively. These distributions are based on the local elevation measurements on the U-shaped naphthalene cassette [see Fig. 5(e) and 9] with balsa wood stripes attached to the naphthalene surface at the same locations where balsa wood stripes were attached to the eight individual cassettes near the turn for regional mass transfer measurements. In each of the two figures, the four Sh/Sh_0 distributions for $Re \approx$ 9,400, 16,800, 31,800, and 57,200 are similar, with lower values when the Reynolds number is higher. Also, the ribs cause large variations of the local mass transfer, as they

periodically interrupt the boundary layers on the bottom wall. Note that the Sh/Sh_0

distributions on the ribbed wall are presented in Figs. 16 and 17 with a scale that is

different from that for the distributions on the smooth bottom wall in Figs. 13 and 14.

For flows in both directions, the streamwise Sh/Sh_0 variations between

consecutive ribs in the inlet section are larger than the spanwise variations. Upstream of

the turn, as the flow reattaches onto the bottom wall downstream of the ribs, the Sh/Sh_0

value is higher than 3.1 to 3.4 over the reattachment regions in the smaller inlet section,

and is higher than 2.2 to 2.5 in the larger inlet section, depending on the Reynolds

number. In the turn, there are very large mass transfer variations, with the largest Sh/Sh_0

values near the end wall just downstream of the rib in the turn and small Sh/Sh_0 values

upstream of the rib in the turn and upstream of the first rib in the exit section. The local

Sherwood number ratio is also large along the upstream half of the end wall and near the

downstream outer wall, and is small along the upstream outer wall, as in the smooth wall

cases. The interactions of secondary flows in the turn with ribs on two opposite walls

cause very large variations of the local mass transfer and the various individual regions

of high and low mass transfer in the turn.

Comparing Figs. 16 and 17, it can be seen that the Sh/Sh_0 value upstream of the

turn is higher in the smaller inlet section than in the larger inlet section, because of the

higher velocities of the flow in the inlet section with the smaller flow cross sectional

area. Unlike in the smooth wall case, the Sh/Sh_0 values are much lower in the larger exit

section than in the turn (Fig. 16), as the air flows over the bottom wall with ribs at lower

velocities in the larger exit section. In the smooth wall case, the increase of the

turbulence in the flow keeps the *Sh/Sh*$_0$ values relatively high in the larger exit section [see Fig. 13]. Figure 15 shows that the regional average mass transfer downstream of the turn is higher in the larger exit section with smooth walls than in the larger exit section with ribs on the top and bottom walls. The $\overline{Sh}/Sh_0$ values are between 2.1 and 3.2 in the smooth wall case and between 1.8 and 2.5 in the ribbed wall case. However, Fig. 15 also shows that $\overline{Sh}/Sh_0$ is about 2.0 further downstream in the larger ribbed exit section, while $\overline{Sh}/Sh_0$ continues to decrease along the larger smooth exit section and reaches a value of just over 1.0 at the channel exit.

For air flow entering the larger upstream straight section (Fig. 17), the mass transfer is clearly the highest downstream of the turn, as the flow that leaves the turn with very high turbulence enters the smaller exit section. Individual regions of very high *Sh/Sh*$_0$ values are evident along the outer wall and along the downstream side of the divider wall. The *Sh/Sh*$_0$ distributions between consecutive ribs in the smaller exit section are very different from the almost two-dimensional distributions resulting from the periodic separated and reattached flow over the ribs on the bottom wall in the inlet section. The local distributions in the smaller exit section with ribs given in Fig. 17 are consistent with the corresponding regional average distributions presented in Fig. 15(c), which shows that $\overline{Sh}/Sh_0$ is much larger on wall segment nos. 10, 11, and 12 downstream of the turn than on wall segment nos. 8 and 9 in the turn.

2.4.5 Average Mass Transfer Results in Trapezoidal Channel with Smooth, Ribs on One Wall, and Ribs on Two Walls

In the trapezoidal channel, with smooth, ribs on one wall, and ribs on two walls, and with air entering smaller and larger straight section of the channel, average Sherwood number ratios of the entire mass transfer active surfaces of the sixteen cassettes and of the turn-region mass transfer active surfaces of the eight cassettes near the end wall were compared in Fig. 18. $\overline{Sh}/Sh_0$ of the sixteen entire-region and the eight turn-region mass transfer active surfaces decrease, as Reynolds number increases from 9,400 to 57,200, whether the trapezoidal channel has smooth walls, ribs on one wall, or ribs on two walls and with air entering smaller and larger straight section of the channel. Tables 2 and 3 tabulate average Sherwood number ratios of the sixteen segments and the eight turn-region segments in the trapezoidal channel with smooth walls, ribs on one wall, and ribs on two walls and with air entering smaller and larger straight section of the channel, respectively. In the trapezoidal channel with smooth walls, $\overline{Sh}/Sh_0$ with air entering smaller straight section of the channel has higher values of 1.75 ~ 1.99 and 2.06 ~ 2.42 than $\overline{Sh}/Sh_0$ values, with air entering larger straight section of the channel, of 1.68 ~ 1.87 and 1.80 ~ 2.20 for the sixteen and the eight turn-region cassettes, respectively. In the trapezoidal channel with ribs on one wall, $\overline{Sh}/Sh_0$ values, with air entering larger straight section of the channel, are 1.40 ~ 1.58 and 1.36 ~ 1.48 times higher than $\overline{Sh}/Sh_0$ values with smooth walls. The $\overline{Sh}/Sh_0$ values, with air entering the
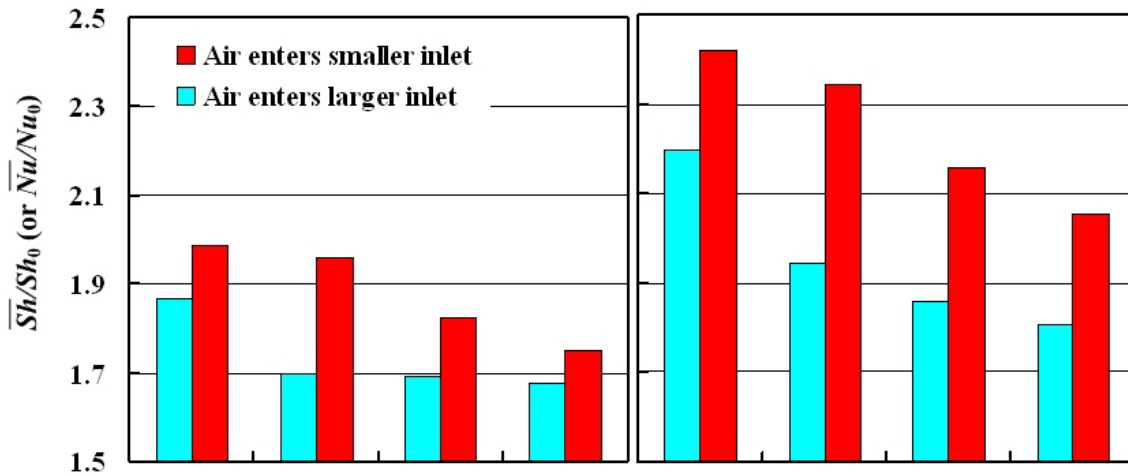
(a) Smooth walls
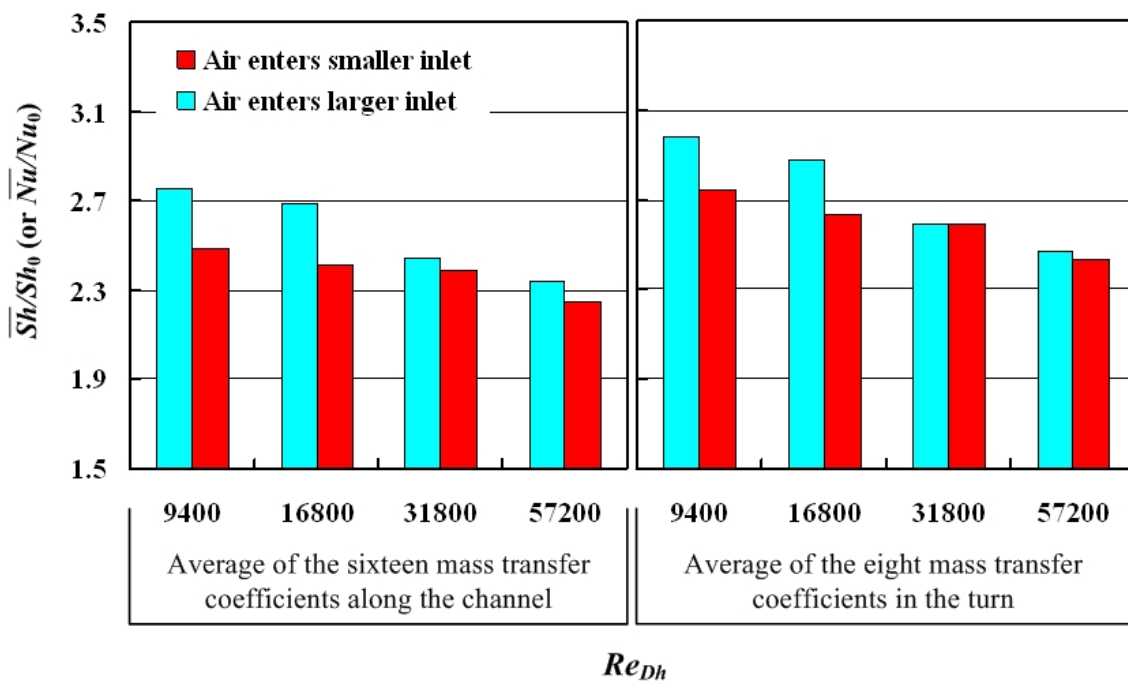
(b) Ribs on one wall

Fig. 18 Averages of regional average mass transfer coefficient ratios of the sixteen and eight mass transfer active surfaces in the trapezoidal channel with (a) smooth walls, (b) ribs on one wall, and (c) ribs on two walls
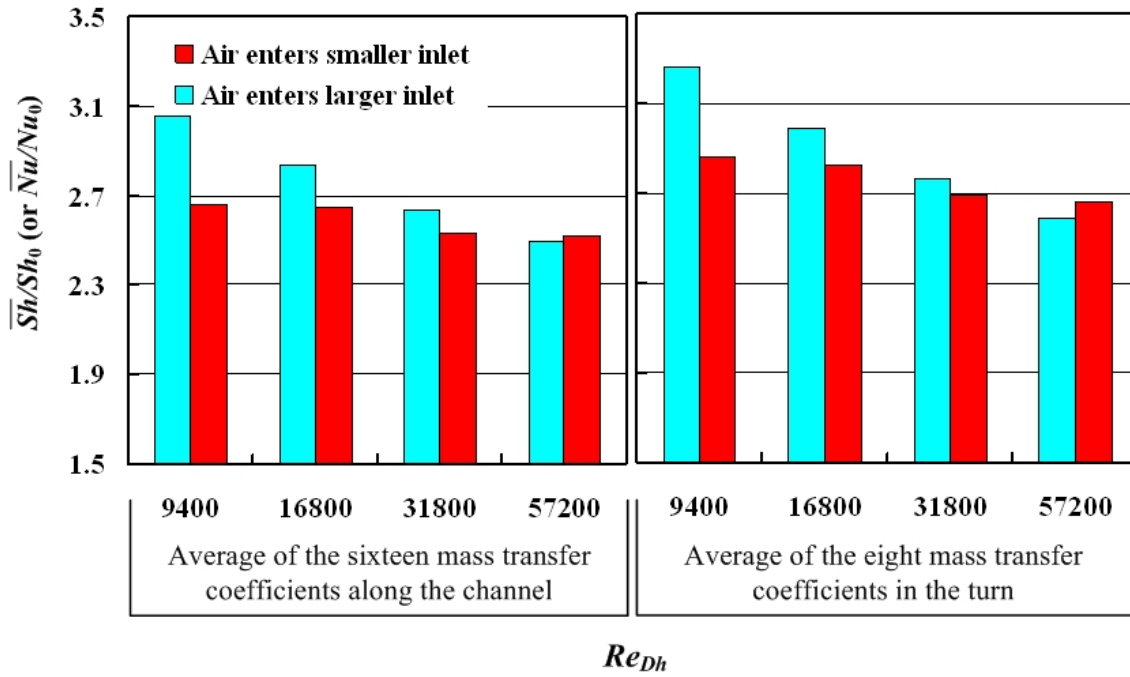
(c) ribs on two walls

Fig. 18 (continued)

smaller straight section of the channel, are 1.23 ~ 1.31 and 1.12 ~ 1.20 times higher than

$\overline{Sh}/Sh_0$ values with smooth walls for the sixteen cassettes and the eight turn region

cassettes, respectively, at Reynolds numbers of 9,400 ~ 57,200. In the trapezoidal

channel with ribs on two walls, $\overline{Sh}/Sh_0$ values, with air entering the larger straight

section of the channel, are 1.49 ~ 1.67 and 1.44 ~ 1.54 times higher than $\overline{Sh}/Sh_0$ values

Table 2 Average mass transfer coefficient ratios of the sixteen and the eight turn-region mass transfer active surfaces in the trapezoidal channel with smooth walls, ribs on one wall, and ribs on two walls and with air entering smaller straight section of the channel

Re_{Dh}	Smooth walls		Ribs on one wall		Ribs on two walls	
	$\overline{Sh}/Sh_0$		$\overline{Sh}/Sh_0$		$\overline{Sh}/Sh_0$	
	Sixteen segments	Eight segments near the turn	Sixteen segments	Eight segments near the turn	Sixteen segments	Eight segments near the turn
9,400	1.99	2.42	2.49	2.75	2.66	2.86
16,800	1.96	2.35	2.42	2.64	2.65	2.83
31,800	1.82	2.16	2.39	2.59	2.53	2.70
57,200	1.75	2.06	2.25	2.44	2.52	2.66

Table 3 Average mass transfer coefficient ratios of the sixteen and the eight turn-region mass transfer active surfaces in the trapezoidal channel with smooth walls, ribs on one wall, and ribs on two walls and with air entering larger straight section of the channel

Re_{Dh}	Smooth walls		Ribs on one wall		Ribs on two walls	
	$\overline{Sh}/Sh_0$		$\overline{Sh}/Sh_0$		$\overline{Sh}/Sh_0$	
	Sixteen segments	Eight segments near the turn	Sixteen segments	Eight segments near the turn	Sixteen segments	Eight segments near the turn
9,400	1.87	2.20	2.76	2.99	3.06	3.26
16,800	1.70	1.95	2.69	2.88	2.84	2.99
31,800	1.69	1.86	2.45	2.59	2.64	2.77
57,200	1.68	1.80	2.34	2.47	2.50	2.59

with smooth walls. The $\overline{Sh}/Sh_0$ values, with air entering smaller straight section of the channel, are 1.34 ~ 1.44 and 1.18 ~ 1.29 times higher than $\overline{Sh}/Sh_0$ values with smooth walls for the sixteen cassettes and the eight turn region cassettes, respectively, at Reynolds numbers of 9,400 ~ 57,200. The effect of ribs on $\overline{Sh}/Sh_0$ is higher when air enters the larger straight section of the trapezoidal channel than when air enters smaller straight section of the channel. Acceleration of flow, due to decrease of cross section of the channel at the turn, might help more vigorous mixing and breaking of the boundary layer of the flow with existence of ribs on one wall or two walls, compared with deceleration of flow at turn in the trapezoidal channel with ribs on one wall or two walls. Whether ribs are installed on one wall or two walls and with air entering larger or smaller straight section of the channel, the enhancement of $\overline{Sh}/Sh_0$ at the turn region is lower than the enhancement of $\overline{Sh}/Sh_0$ at the straight section of the channel. Existence of vigorous mixing at the turn region might not be much affected by the additional turbulence promoters (ribs) on one wall and two walls in the trapezoidal channel, compared with the effect of ribs on the enhancement in the straight section of the channel.

2.4.6 Pressure Drop across the Turn in Trapezoidal Channel

The pressure drop across the turn was defined as the difference between the static pressures at two streamwise stations near the turn in the two straight sections of the trapezoidal test channel [see Fig. 7]. These stations were at a distance of 43.8 *cm* from the inlet and exit, respectively. The distance between the two stations [L in Eq. (17)], measured along the centerline of the test channel around the turn, was 36.2 *cm*. The pressure drop results are presented in this section in terms of a friction factor ratio, *f/f*$_0$, which gives the average pressure gradient around the turn relative to that for fully developed turbulent flow at the same Reynolds number in a smooth straight channel with a hydraulic diameter equal to that of the cross section at the turn clearance. A minor loss coefficient for the turn may be calculated from the friction factor as $f \cdot (L/D_h)$.

In Fig. 19, the pressure drops across the turn are presented for flows at four different flow rates through a square channel with smooth walls, and trapezoidal channels with smooth walls, ribs on one wall, and ribs on two opposite walls, and with flows in opposite directions --- flow entering the channel through the smaller straight section or through the larger straight section. The results show that the friction factor ratio increases with increasing Reynolds number in all of the cases studied. The turn in the trapezoidal channel with smooth walls, with air flow in either direction, causes a higher pressure drop than the turn in the square channel with smooth walls. The *f/f*$_0$ value ranges from 9.4 to 15.4 for the trapezoidal channel with a larger inlet section, and from 6.5 to 10.2 for the trapezoidal channel with a smaller inlet section, as Reynolds
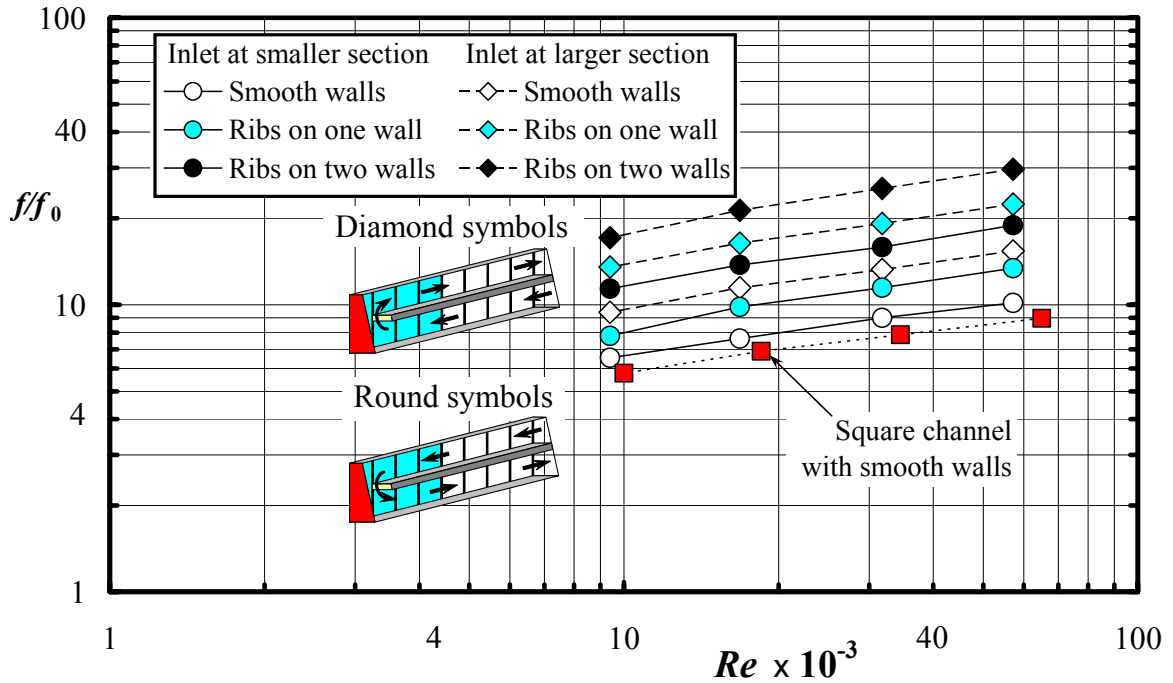
Fig. 19 Overall pressure drops across sharp turns in square and trapezoidal channels

number is increased from about 10,000 to 60,000. Thus, the acceleration of the flow around the turn as the flow cross section decreases appears to cause about 50% higher pressure drop than when the flow direction is reversed. As expected, ribs on one wall cause an additional pressure drop across the turn, and ribs on two walls increases the pressures drop across the turn more than ribs on one wall only. In the case of a trapezoidal channel with the air flow entering the larger straight section of the channel and ribs on two opposite walls, the pressure drop across the turn is the highest, with f/f_0 values ranging from 17.1 to 29.7, which are 50 to 60% higher than the corresponding values in the case with the flow direction reversed.

CHAPTER III

THERMAL CHARACTERISTICS AND MECHANISMS

OF A NOVEL HEAT PIPE

3.1 THERMAL CHARACTERISTICS OF A NOVEL HEAT PIPE

3.1.1 Experimental Apparatus

A schematic of the test apparatus to characterize thermal performance of the QuTech® Heat Pipe (QTHP) is shown in Fig. 20. The test apparatus consisted of a test section, a Cole Parmer constant temperature bath, and a data acquisition system. The test section consisted of a copper rod, four heaters, a cooling jacket, and the QTHP. The QTHP was made of a copper tube with an inside diameter of 0.54 *cm*, a wall thickness of 0.30 *mm*, and a length of 30.48 *cm*. The evaporator section consisted of an oxygen-free copper cylinder with an outside diameter of 3.81-*cm* and length of 5.72-*cm*. Four OMEGA CIR cartridge heaters, with a 0.64-*cm* diameter and 3.81-*cm* length, were embedded into the copper rod and were controlled with a single Variac transformer. The QTHP was embedded at the center of the copper rod at a depth of 5.08-*cm*. In the condenser section, a 6.35-*cm* inner diameter Teflon PTFE water cooling jacket was connected to the Cole Parmer constant temperature bath through an OMEGA rotameter that measured volumetric flow rates of cooling fluid. The cooling fluid used during the

experiments was distilled water. The water cooling jacket contained nine 6.35-*cm* diameter copper baffles that were threaded onto a 2.54-*cm* diameter and 11.43-*cm* length copper rod. Similar to the evaporator region, the QTHP was embedded into the cooling jacket, as shown in Fig. 21 and 22. The nine threaded copper baffles and threaded copper
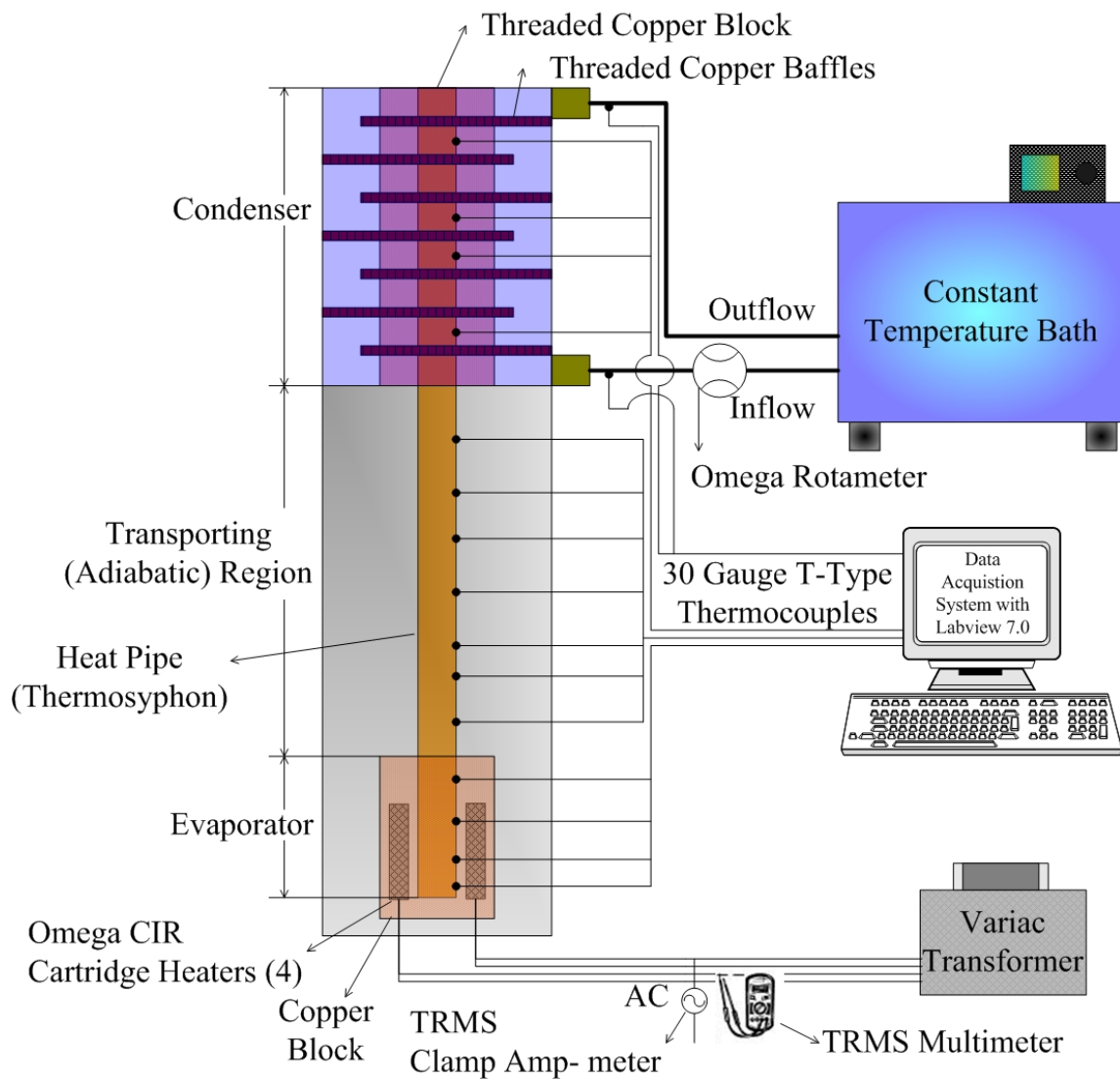
Fig. 20 Schematic of test apparatus: a test section, a constant temperature bath, and a data acquisition system

Copper rod to embed a condenser of heat pipe

Copper baffles (9) to circulate cooling fluid

Coolant out

Heat pipe

Coolant in
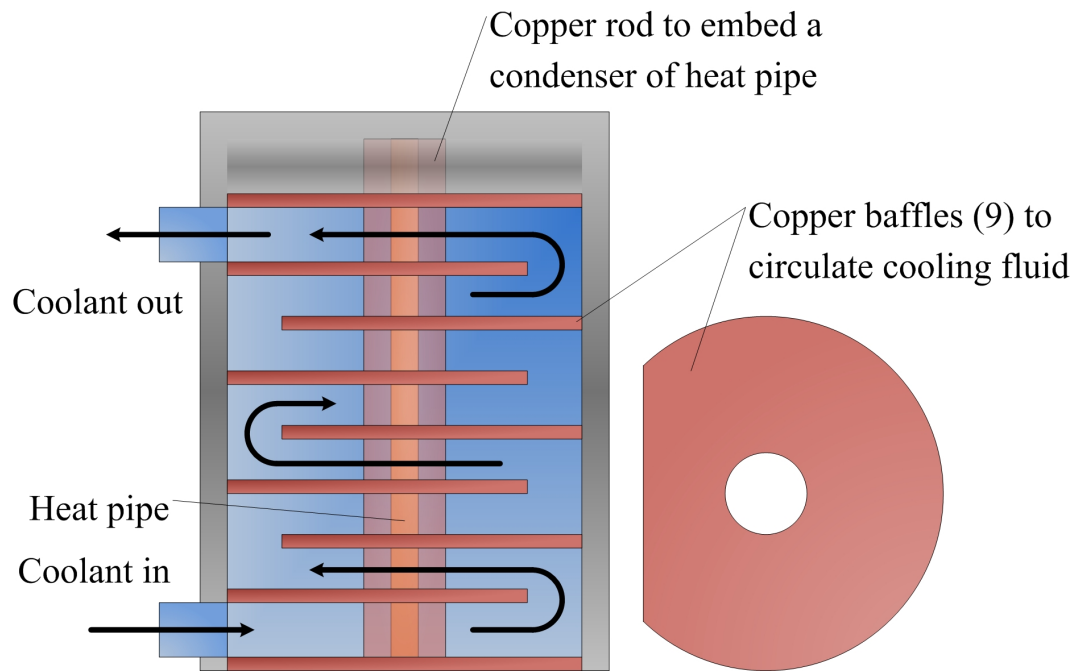
Fig. 21 Schematic of nine threaded copper baffles that were fit into threaded copper rod inside the cooling jacket

rod efficiently transferred heat from the QTHP to the cooling water by increasing contact surface areas of the QTHP on the coolant and circulating the coolant for a longer time, as shown in Fig. 21.

Fifteen 30 gauge T-type thermocouples were used to obtain temperature distributions along the QTHP. These were installed on the surface of the QTHP with high temperature resistant Kepton adhesive tape in order to prevent detachment of the thermocouples from the hot surface of the QTHP during thermal performance tests. Fig. 22 shows the location of the fifteen thermocouples along the QTHP; First four (1T ~ 4T), next seven (5T ~ 11T) in middle, and last four thermocouples (12T ~ 15T).
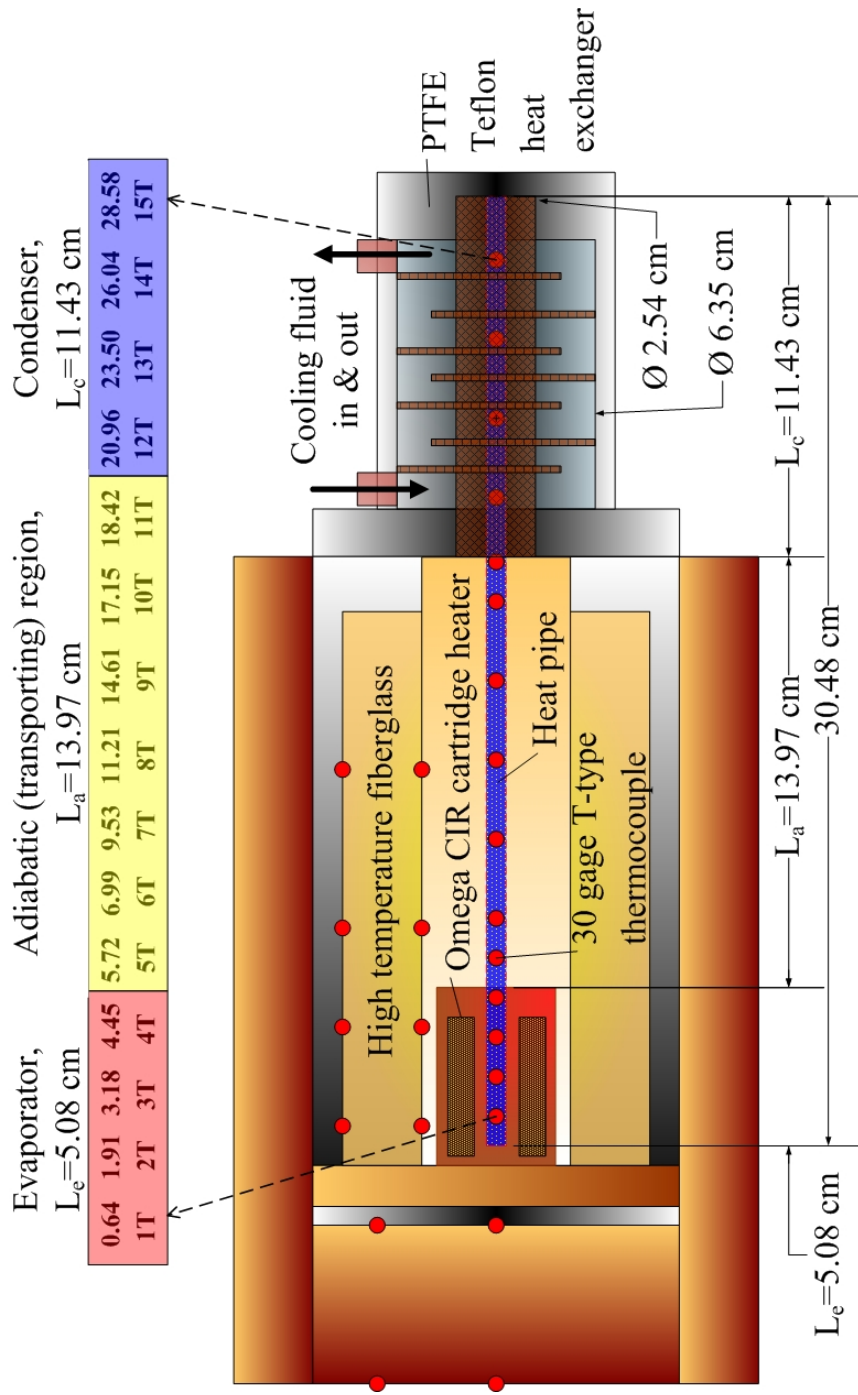
Fig. 22 Schematic of test section and locations of fifteen 30 gauge T-type thermocouples installed on Qu Tech® Heat Pipe (unit in *cm*)

These measured the surface temperatures of the evaporator, transport zone (adiabatic zone), and condenser of the QTHP, respectively. Each four thermocouples in the evaporator and condenser of the QTHP were installed on the surface of the QTHP through each four holes in the copper rod of the evaporator and threaded copper rod of the condenser [see Fig. 20]. Seven thermocouples in the adiabatic zone were installed on the surface of the QTHP with high temperature resistant Kepton adhesive tape, as mentioned earlier. Temperatures were recorded on the data acquisition system that consisted of a National Instrument's PCI-6024E board, a SCXI-1102 conditioner, a TC-2095 terminal block, and a computer on which Labview 7.0 was installed. Every 30 gauge T-type thermocouple used in the tests was carefully calibrated with a NIST calibrated thermometer, the data acquisition system, and the Cole Parmer constant temperature bath.

The evaporator and transporting zones were insulated with high temperature fiberglass insulation. The first layer had an inner diameter of 1.59-*cm* and a thickness of 1.27-*cm*. The second layer of insulation had an inner diameter of 4.76-*cm* and a thickness of 2.54-*cm*. A Teflon PTFE enclosure that had a 9.86-*cm* inner diameter and a wall thickness of 0.79-*cm* covered the evaporator and condenser regions to prevent possible bending and/or shift of the QTHP. Finally, a 5.08-*cm* thick fiberglass blanket covered the evaporator and adiabatic regions of the test section to further ensure minimal heat loss.

Twelve 30 gauge T-type thermocouples were located on the fiberglass insulation of the evaporator and adiabatic regions to estimate heat loss to ambient [see Fig. 22].

The temperature of the cooling water entering the cooling jacket was measured with a thermocouple that was installed in the inlet hose. A second thermocouple was installed in the exit hose in order to determine the temperature increase of the cooling water. The volumetric flow rate of the cooling water was measured at the inlet with a rotameter. With these measurements, the net rate of heat transfer from the QTHP to the cooling water was verified. [see Fig. 20].
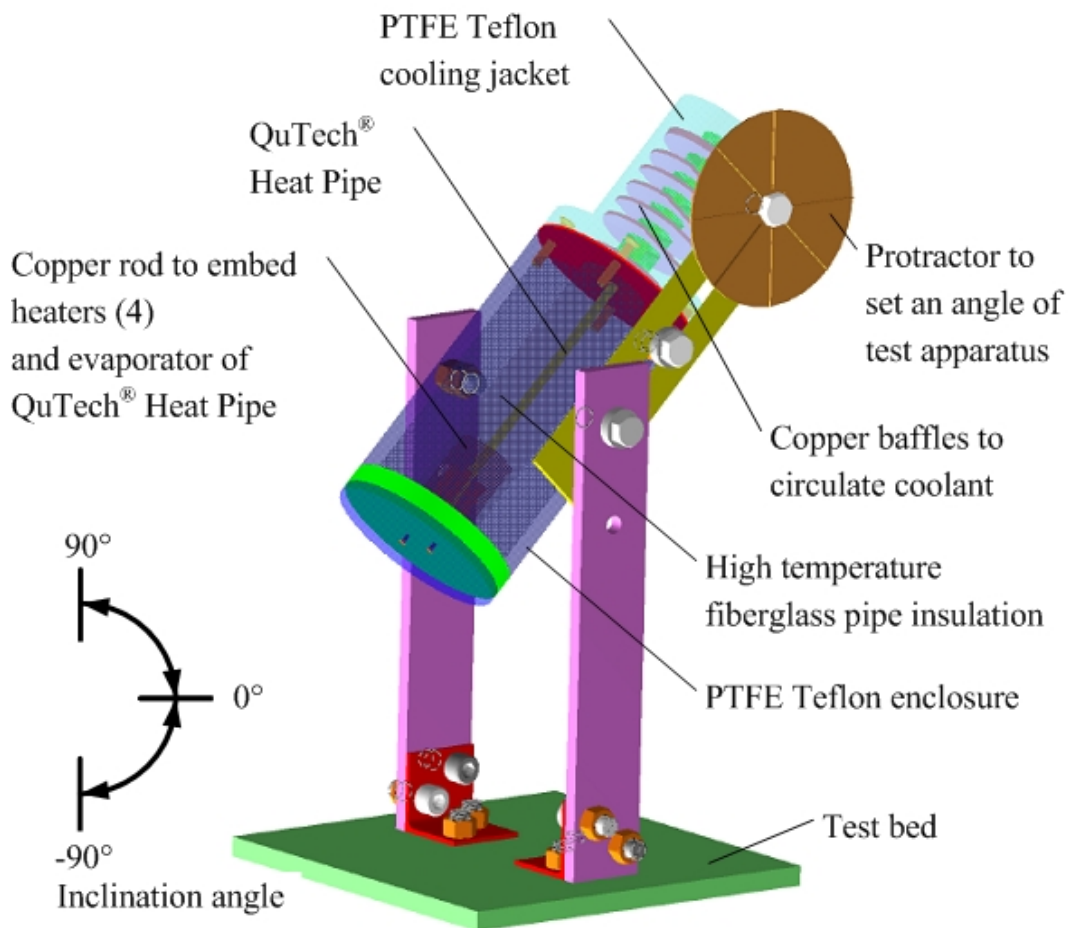
Fig. 23 Schematic of test apparatus and test bed to set an inclination angle of QuTech[®] Heat Pipe

Since the cooling jacket was maintained at 20°C, heat loss/gain through the cooling jacket was assumed to be negligible to the air-conditioned laboratory that was maintained at 21 ~ 22°C. To prevent even a small amount of heat loss or gain through the cooling jacket, pipe insulation tape was applied on the cooling jacket.

A test bed held the test apparatus at various inclination angles from a positive (lower position of the evaporator of the QTHP) vertical angle of 90° to a negative (higher position of the evaporator of the QTHP) angle of -90°, as shown in Fig. 23. Inclination angles were measured with an installed protractor and a string with a weight that represented an angle of 90° by gravitational force on the weight.

3.1.2 Experimental Procedure

Prior to turning the heaters on, the Cole Parmer constant temperature bath was commenced to prevent possible damage on the QTHP due to a sudden heat. To ensure that a steady state condition of the QTHP was reached power was applied to the four heaters with the variac transformer for appropriately two and one-half hours prior to recording any temperatures. Voltage and current to the heaters were measured with a digital TRMS multi-meter and clamp amp-meter. Once temperatures, voltage, current, and coolant volumetric flow rate were recorded, the input power to the QTHP was increased to reach the next test condition. As the temperatures on the surface of the

QTHP reached higher values, the power was increased at smaller increments. When a sudden increase in temperatures on the surface of the evaporator of the QTHP was noticed, the QTHP was considered to have reached its dry-out condition. The dry-out condition is the failure of heat transport from the evaporator to the condenser. Input power to the heaters was the shut down to prevent surface temperatures of the QTHP from climbing even further.

The rate of heat removal from the condenser of the QTHP to the coolant water was obtained from the net rate of heat transfer to the evaporator of the QTHP (input power to the heaters minus the estimated heat loss to ambient through the insulations). This was compared to an energy balance performed with knowledge of the coolant water volumetric flow rate, inlet temperature and outlet temperature as previously described. The estimated heat losses were less than 2%, however as the QTHP reached the near dry-out condition, the heat losses increased. [see section 3.1.3]. Once the heat removal rate from the condenser was verified, a volumetric flow rate of $4.1 \times 10^{-5} \ m^3/s$ was set to ensure full heat removal from the condenser over the range of applicable input powers.

To quantify the gravitational effect on the performance of the QTHP, the test apparatus was inclined at five different inclination angles of 90˚, 45˚, 0˚, -45˚, and -90˚ [see Fig. 23]. The maximum performance of the QTHP was measured at each different inclination angle.

3.1.3 Data Reduction

Power supplied to the four cartridge heaters was determined as

$$P_{input} = V \times I \quad [W] \tag{19}$$

where V is the voltage, and I is the current. These values were measured with a digital TRMS multi-meter and a clam amp-meter, respectively.

Net rate of heat transfer to the evaporator of the QTHP was obtained by

$$\dot{Q}_{net} = P_{input} - \dot{Q}_{Heat\,Loss} \quad [W] \tag{20}$$
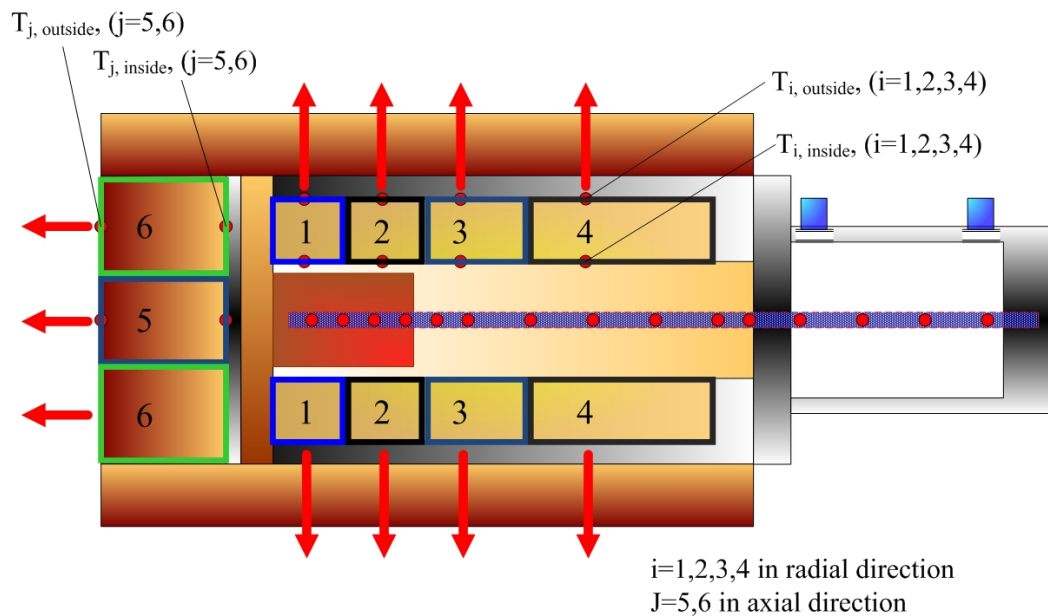
Fig. 24 Schematic of segments to estimate heat losses and locations of twelve 30 gauge T-type thermocouples [see Eq. (21)]

where the heat loss to the surroundings through the insulation, $\dot{Q}_{Heat\,Loss}$, was estimated from the twelve 30 gauge T-type thermocouples that were installed on the high-temperature fiberglass insulation, as shown in Fig. 24. The temperatures used to calculate the heat loss in the radial direction were recorded at segments one through four. Segments five and six provided the temperatures for determining the heat loss in the axial direction. The total heat loss was quantified as the combination of the axial and radial direction heat loss as the following equation shows.

$$\dot{Q}_{Heat\,Loss} = \sum_{i=1}^{4}\dot{Q}_i + \sum_{j=5}^{6}\dot{Q}_j \quad [W] \tag{21}$$

The heat loss through the fiberglass insulation in radial direction was obtained by

$$\dot{Q}_i = \frac{2\pi k_{ins,i} l_{ins,i}\left(T_{in}-T_{out}\right)_i}{\ln\left(r_{out}\Big/r_{in}\right)} \quad [W] \quad ,k_{ins,i}=k_{ins,i}(T_{av,i}),\, i=1,2,3,4 \tag{22}$$

where $l_{ins,i}$, and r_{in} and r_{out} indicated the width of each segment, and inner and outer diameter of the fiberglass insulation, respectively. Heat losses through the fiberglass insulation in the axial direction were obtained by

$$\dot{Q}_j = k_{ins,j} A_{ins,j} \frac{\left(T_{in}-T_{out}\right)_j}{\Delta z_j} \quad [W] \quad ,k_{ins,j}=k_{ins,j}(T_{av,j}),\, j=5,6 \tag{23}$$

where $A_{ins,j}$ and Δz_j indicated the cross sectional area of each segment and the distance of the fiberglass insulation in-between each of the two thermocouples, respectively. Thermal conductivities of the fiberglass insulation, k_{ins}, were obtained by averaging the temperatures from the two thermocouples in each segment.

To verify the rate of heat removal from the condenser, the rate of heat transfer to the cooling jacket from the QTHP (see Fig. 20) was obtained by

$$\dot{Q}_c = \rho_w \dot{V}_w C_p (T_o - T_i) \quad [W] \tag{24}$$

where T_0 and T_i were the outlet and inlet temperatures of the cooling jacket, respectively. ρ_w was the density of the water at the average temperatures of T_0 and T_i. $\dot{V}_w$ was the volumetric flow rate that was measured with the Omega rotameter. The rate of heat removal from the condenser was used to check the net rate of heat transfer to the evaporator as follows:

$$\dot{Q}_{net} \cong \dot{Q}_c \quad [W] \tag{25}$$

The effective thermal conductivity of the QTHP was evaluated from Fourier's Law as

$$k_{eff} = \dot{Q}_{net} \frac{L_{eff}}{A_{HP}(T_{av,e} - T_{av,c})} \quad [W/mK] \tag{26}$$

where the effective length was computed as

$$L_{eff} = \frac{L_e}{2} + L_a + \frac{L_c}{2} \quad [m] \tag{27}$$

where L_e, L_a, and L_c were the lengths of the evaporator, adiabatic section, and condenser, respectively, as shown in Fig. 22. $T_{av,e}$ and $T_{av,c}$ are the average temperatures of each of the four measured temperatures of the evaporator and condenser, respectively. A_{HP} is the cross-sectional area based on the inner diameter of the QTHP.

Heat loss estimations were verified with a known thermal conductivity material of oxygen-free solid copper rod with a 6.35-*mm* diameter and 30.48-*cm* length. The

documented thermal conductivity is 391*W/mK*. The rate of axial heat transfer through the solid copper rod was obtained as follows:

$$\dot{Q}_{CopperRod} = kA_{Cu} \frac{(T_5 - T_{11})}{(z_{11} - z_5)} \quad [W] \tag{28}$$

where, T_5 and T_{11} , and z_{11} and z_5 were measured temperatures from the thermocouples that were noted as 5T and 11T, and axial distance of the thermocouples from the bottom of the evaporator of the QTHP, respectively [see Fig. 22]. Thus, the estimated total heat transfer rate to the heaters was obtained by

$$\dot{Q}_{Total} = \dot{Q}_{Copper\,Rod} + \dot{Q}_{Heat\,Loss} \quad [W] \tag{29}$$

The measured power supplied to the four heaters was used as a true value to check the estimated heat losses, as follows

$$P_{input} \cong \dot{Q}_{Total} \quad [W] \tag{30}$$

Relative errors on the estimated total rate of heat transfer from the four heaters, $\dot{Q}_{Total}$, based on $\dot{Q}_{Copper\,Rod}$ and $\dot{Q}_{Heat\,Loss}$ to the surroundings were obtained by

$$RE(\dot{Q}_{total}) = \frac{P_{input} - \dot{Q}_{Total}}{P_{input}} \tag{31}$$

Fig. 25 shows that temperature distributions along the sold copper rod with two input powers of 10.39 and 20.91W. Temperature distributions were linear except for the evaporator and condenser regions, as expected. Table 4 details heat loss estimations with an error of less than 1.54 % based on two input powers of 10.39 and 20.91 W. The copper rod has relatively low thermal transport capacity, compared to heat pipes and thermosyphons.

The estimation of uncertainty values was based on a confidence level of 95% (or 20:1 odds) and the relative uncertainty analysis method of Coleman and Steele [43]. Also, in all uncertainty calculations, uncertainty values of 1.0% for thermal conductivities of the fiberglass insulation materials and 0.25 *mm* for all physical dimensions were used.
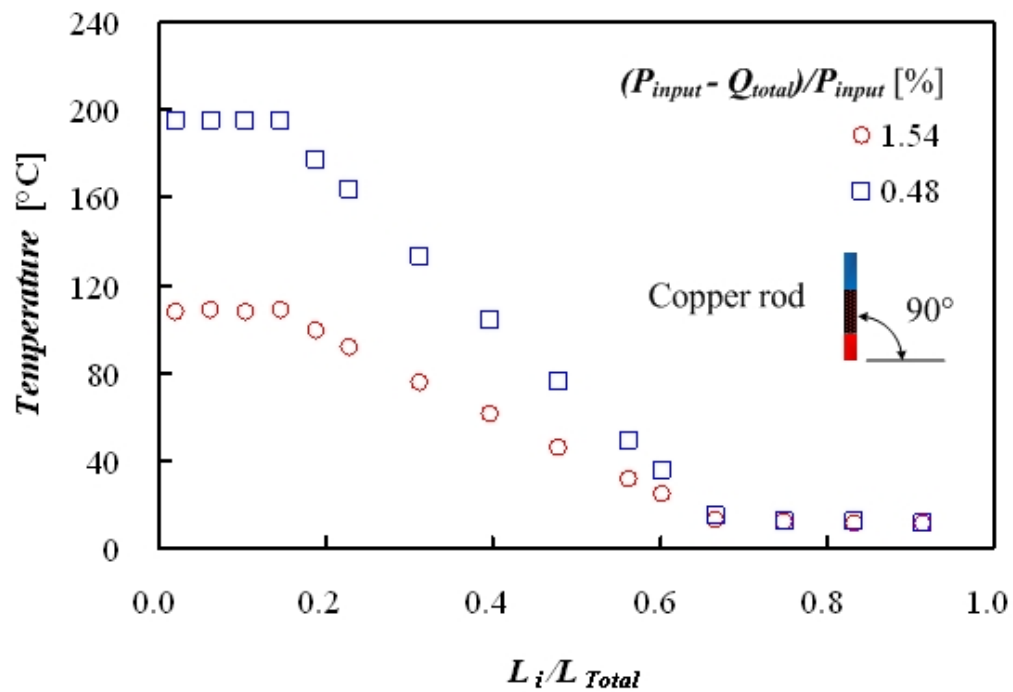
Fig. 25 Temperature distributions along 6.35-*mm* diameter solid copper rod in the test apparatus to verify heat loss estimations

Table 4   Heat loss verification with 6.35-*mm* diameter solid copper rod in the test apparatus

P_{input}	$Q_{Heat\ Loss}$	$Q_{copper\ rod}$	Q_{Total}	$RE(\dot{Q}_{net})$
10.39 W	2.96 W	7.27 W	10.23 W	1.54 %
20.91 W	6.95 W	13.86 W	20.81 W	0.48 %

The uncertainties of the measured voltage and current were 1.0 and 2.5%, respectively. The uncertainty of the input power was 2.7%. The uncertainty of the net rate of heat transfer to the evaporator was also 2.7%. Using the maximum uncertainty values of 2.7% for the net rate of heat transfer to the evaporator and 5.6% for the measured temperatures, the maximum value of the relative uncertainty of the effective thermal conductivity was calculated to be 8.1%.

3.1.4 Presentation and Discussion of Results

The Noren[®] closed two-phase copper-water thermosyphon (CWT), which is a conventional thermosyphon, was thermally characterized and was compared to the performance of the QTHP. The comparisons were conducted at various input powers (temperature differences between the evaporator and condenser) and inclination angles. The CWT had a water filling charge ratio (FR) of 0.82. The dimensions of the CWT were similar to those of the QTHP expect that the outside diameter was 9.4% larger.
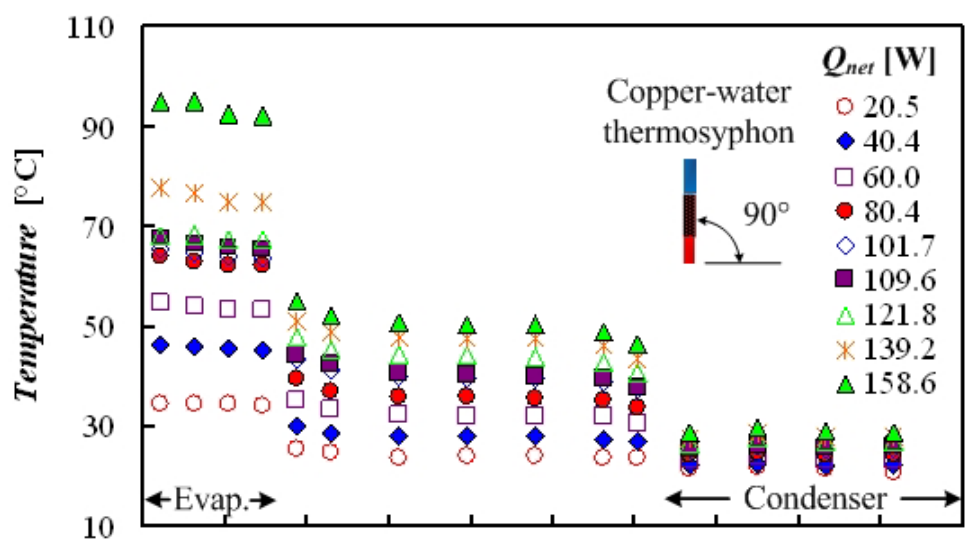
(a) An inclination angle of 90˚
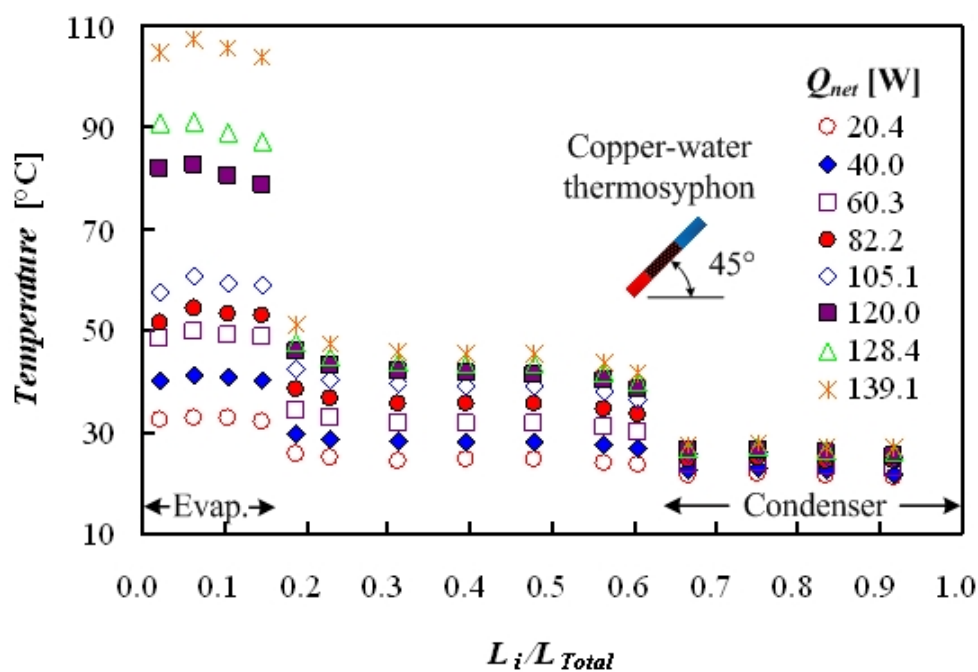
(b) An inclination angle of 45˚

Fig. 26   Temperature distributions along Noren® closed two-phase copper-water thermosyphon at various net rates of heat transfer to the evaporator and inclination angles of 90˚, 45˚, and 0˚
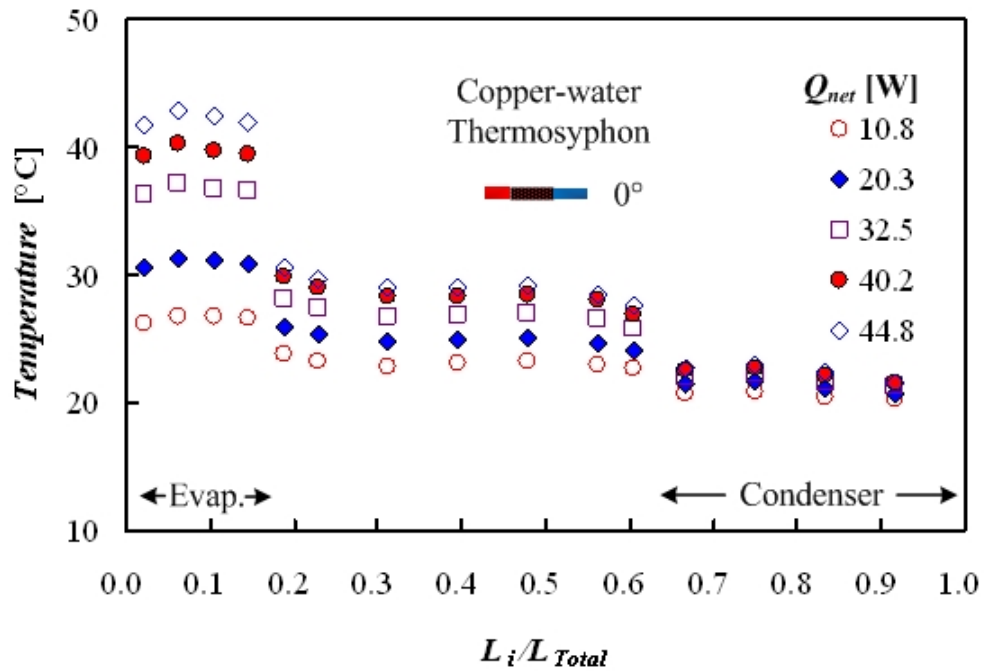
(c) An inclination angle of 0°

Fig. 26 (continued)

Fig. 26 shows the temperature distributions along the CWT at various net rates of heat transfer to the evaporator at inclination angles of 90˚, 45˚, and 0˚. Unlike the temperature distributions along the solid copper rod (Fig. 25), the temperature distributions along the adiabatic section of the CWT (L_i/L_{Total} = 0.19 ~ 0.6) are uniform which indicates that heat transport is occurring through phase change of the working fluid, rather than by conduction through the copper tube. When the CWT reaches its
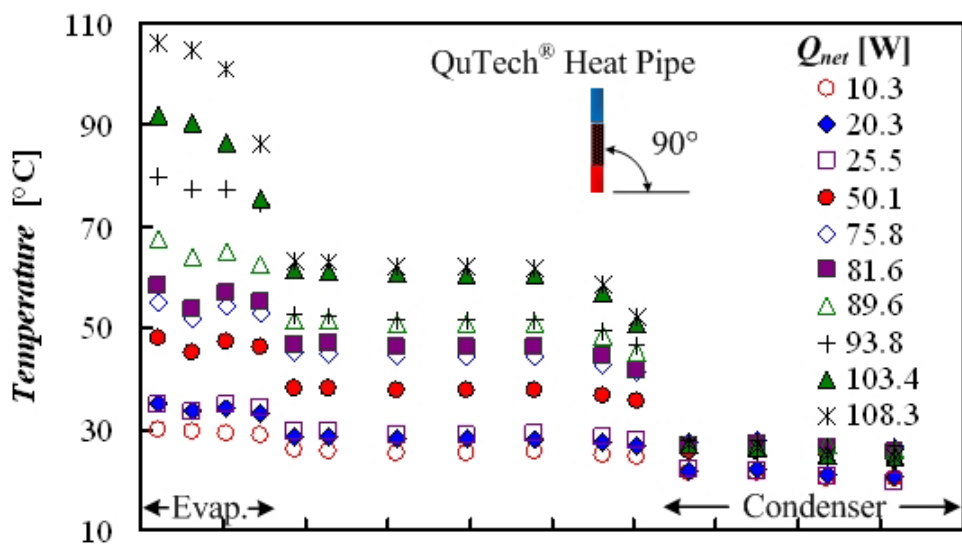
(a) An inclination angle of 90˚
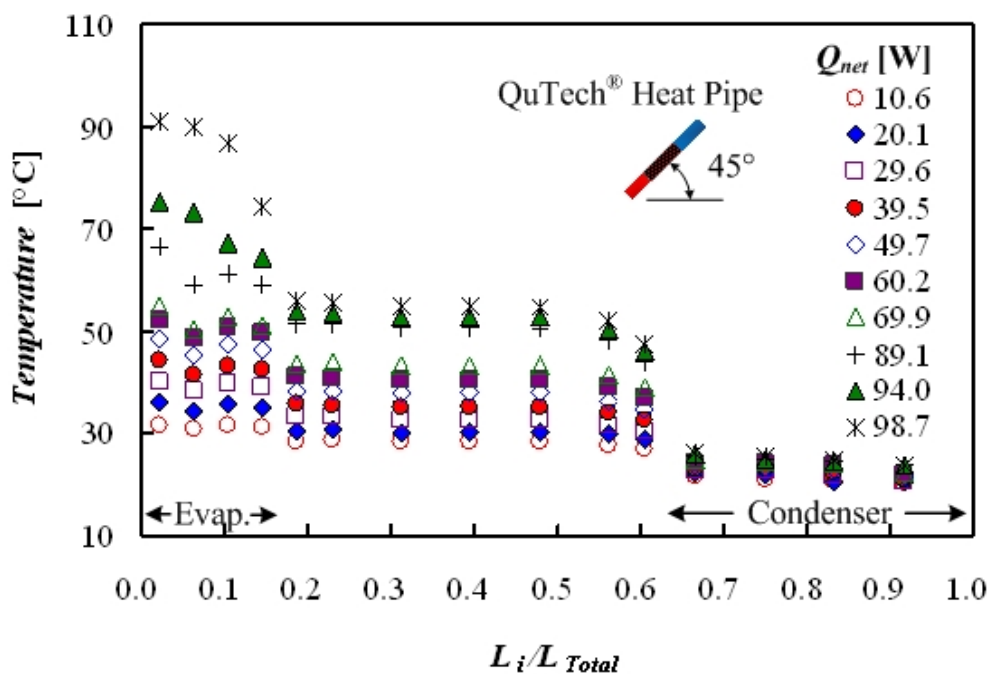
(b) An inclination angle of 45˚

Fig. 27 Temperature distributions along QuTech® Heat Pipe at various net rates of heat transfer to the evaporator and inclination angles of 90˚, 45˚, and 0˚, -45˚, and -90˚
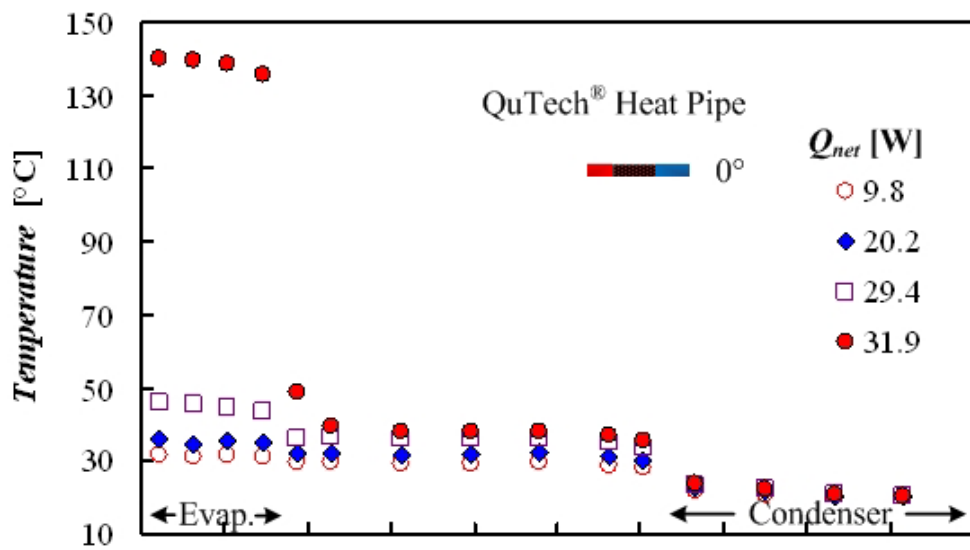
(c) An inclination angle of 0˚
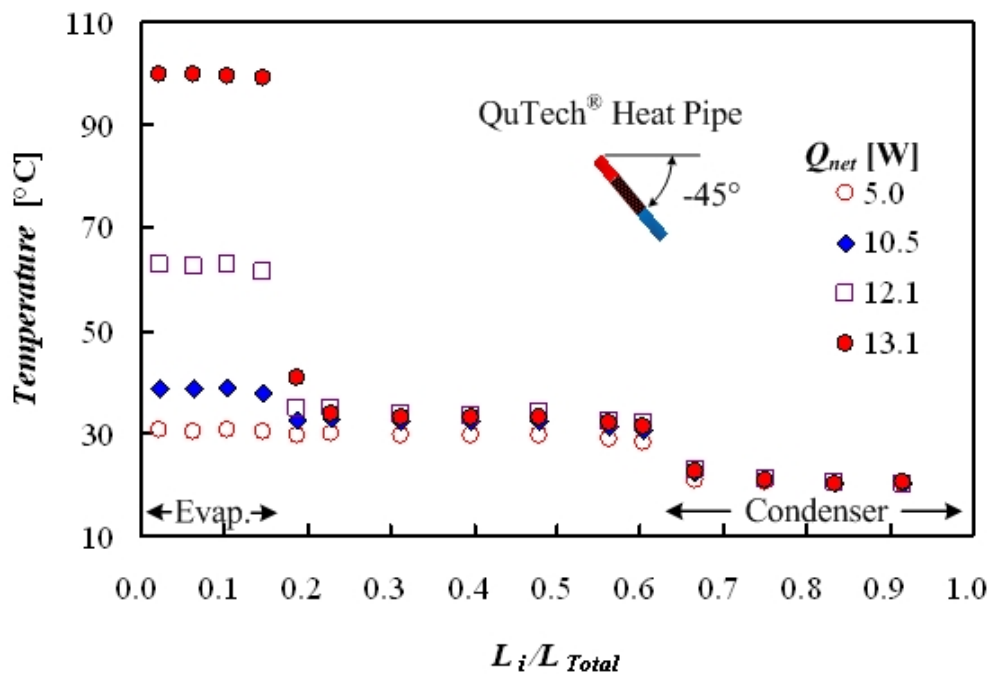
(d) An inclination angle of -45˚

Fig. 27 (continued)
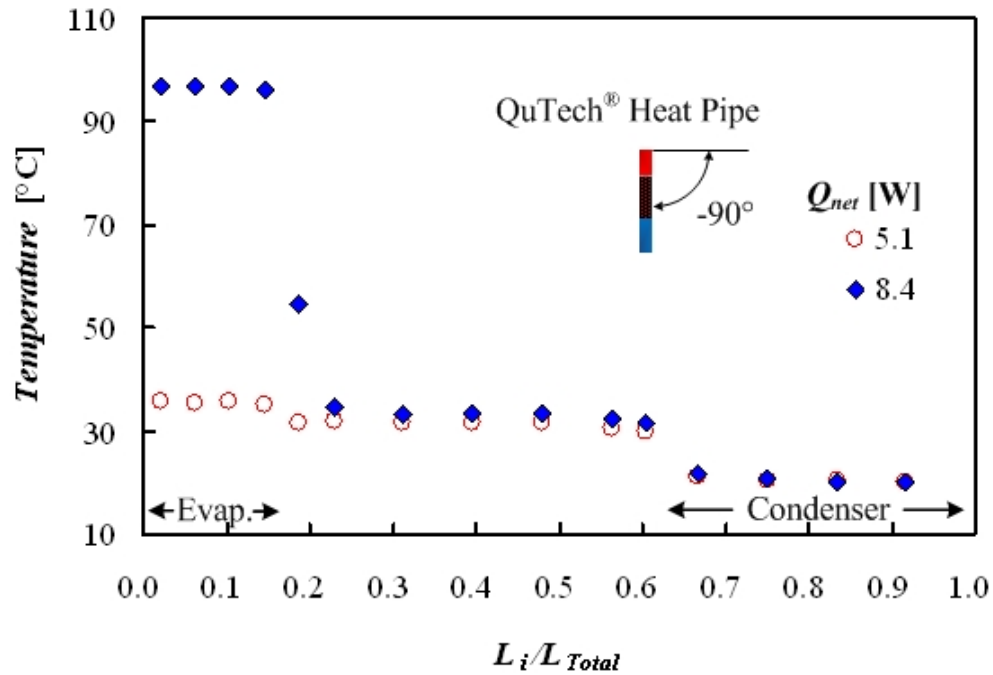
(e) An inclination angle of -90˚

Fig. 27 (continued)

maximum performance (before dry-out of the CWT), the temperatures in the evaporator

increase exponentially, as the net rate of heat transfer to the evaporator increases

linearly, as shown in Fig. 26(a) and 26(b). The CWT relies upon gravity to return the

condensed water from the condenser to the evaporator. Therefore, the performance

decreases dramatically as the gravitational force is less favorable at the inclination

angles of 45˚ and 0˚ [see Fig. 26(b) and 26(c)] [32, 33, and 34].

Fig. 27 shows the temperature distributions along the QTHP at various net rates

of heat transfer to the evaporator and at inclination angles of 90˚, 45˚, and 0˚, -45˚, and -

90˚. Temperature distributions are quite similar with those of the CWT that operates by phase change and utilizes the latent heat of vaporization of water. Temperature distributions of the QTHP also show the stiff increase of the evaporator temperatures, as it is close to failure at every tested inclination angle. The QTHP is considered to have failed even at very low net powers of 13.1W and 8.4W at inclination angles of -45˚ and -90˚, respectively [see Fig. 27(d) and 27(e)]. The results obviously show that gravity is one of the most important factors to determine the thermal performance of the QTHP. The fifth temperatures (L_i/L_{Total} = 0.19), that were next to the four evaporator temperatures, with net powers of 13.1 and 8.4W on Fig. 27(d) and 27(e), respectively, indicate that heat is conducted through the copper tube of the QTHP rather than by the thermal mechanism through the working medium inside of the tube. This is unlike the other temperature distributions of Fig. 27(a), 27(b), and 27(c). It seems that mass in the QTHP may be transporting thermal energy from the evaporator to the condenser in a similar fashion as working fluids in conventional heat pipes/thermosyphons. The QTHP should be positioned with the evaporator below the condenser. In other words, the QTHP requires gravity to function properly as does the CWT.

Figure 28 shows the average temperature differences between the evaporator and condenser of the CWT and the QTHP at various net powers and at an inclination of 90˚. As the net powers increase, the temperature differences increase. Fig. 28(a) shows a large scatter of the average temperature difference between the evaporator and condenser
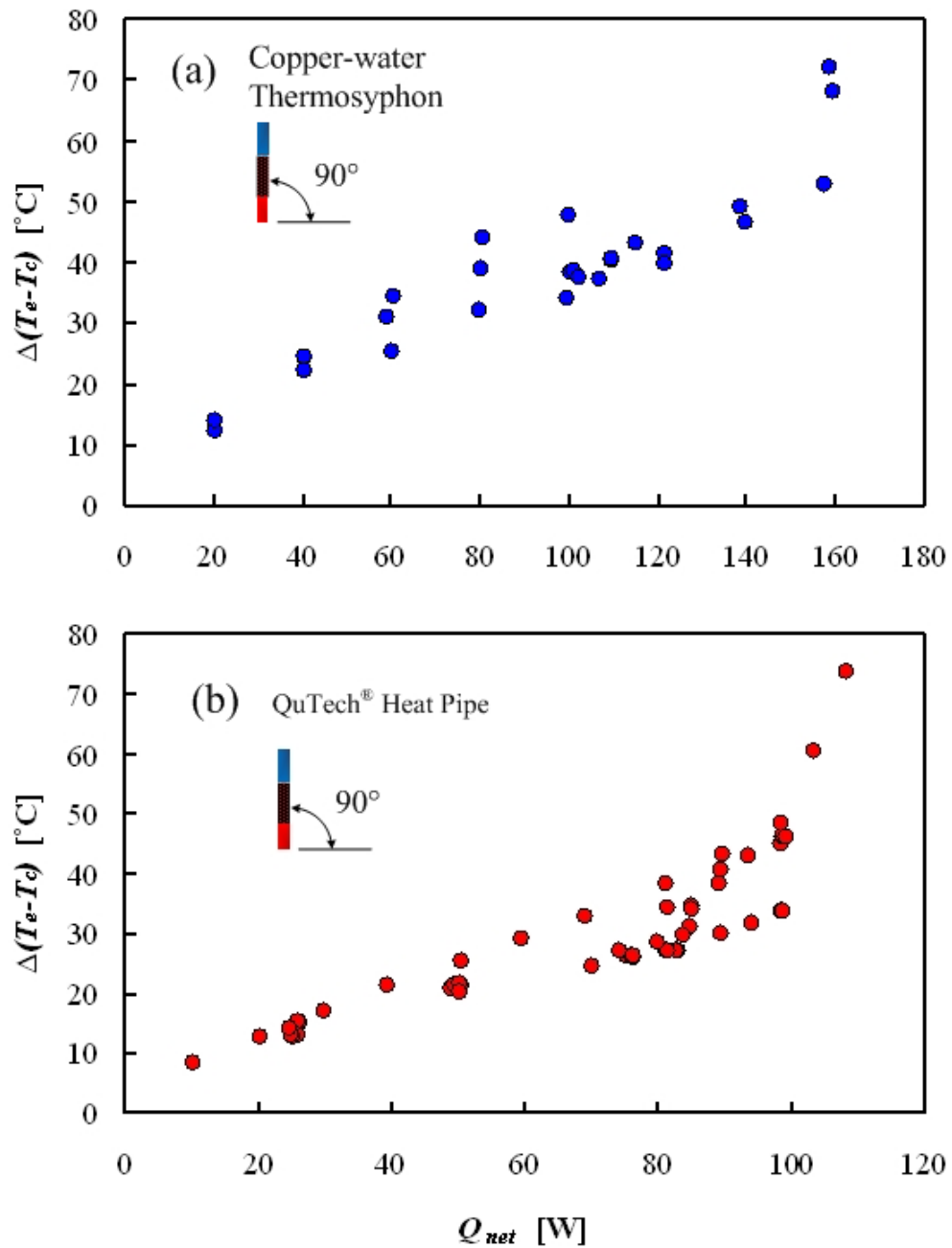
Fig. 28 Average temperature differences between the evaporator and condenser of (a) Noren® closed two-phase copper-water thermosyphon and (b) the QuTech® Heat Pipe at the various net rate of heat transfer to the evaporator and an inclination angle of 90˚

of the CWT at the supplied net powers of 60 ~ 100W. This instability is well known as the hysteresis or geyser effect of conventional heat pipes/thermosyphons which results from the "onset of nucleate boiling". As the net powers increase and thus the temperatures of the evaporator increase, nucleate boiling of the working fluid may start on the surface of the pipe where heat is applied. Since the onset of nucleate boiling is said to be a random phenomenon, especially for water as a working fluid, this results in the relative randomness of the average temperature differences between the evaporator and condenser and the thermal performance of the CWT, as shown in Fig. 28(a) [44 and 45]. A similar trend is not seen in the average temperature differences of the QTHP, as the net powers increase in Fig. 28(b). Unlike the CWT, the randomness of the average temperatures between the evaporator and the condenser of the QTHP occurs just prior to failure.

Rapid rises of the average temperature differences of the CWT and the QTHP at around 160W and around 100W, respectively, are observed at an inclination angle of 90˚. This is due to the dry-out conditions in the evaporators. Comparing the QTHP with the CWT, the QTHP has a more narrow range of operable net power levels up to 100W while the CWT has a wider range of operable net power levels up to 160W.

Fig. 29 shows the average results of the average temperature differences of operable net powers of the two QTHP and CWT. Prior to the QTHP reaching its maximum operable power level, it exhibits less temperature difference between the evaporator and the condenser when compared to the CWT. The temperature difference between the QTHP and the CWT is up to 15˚C at corresponding power levels and at the
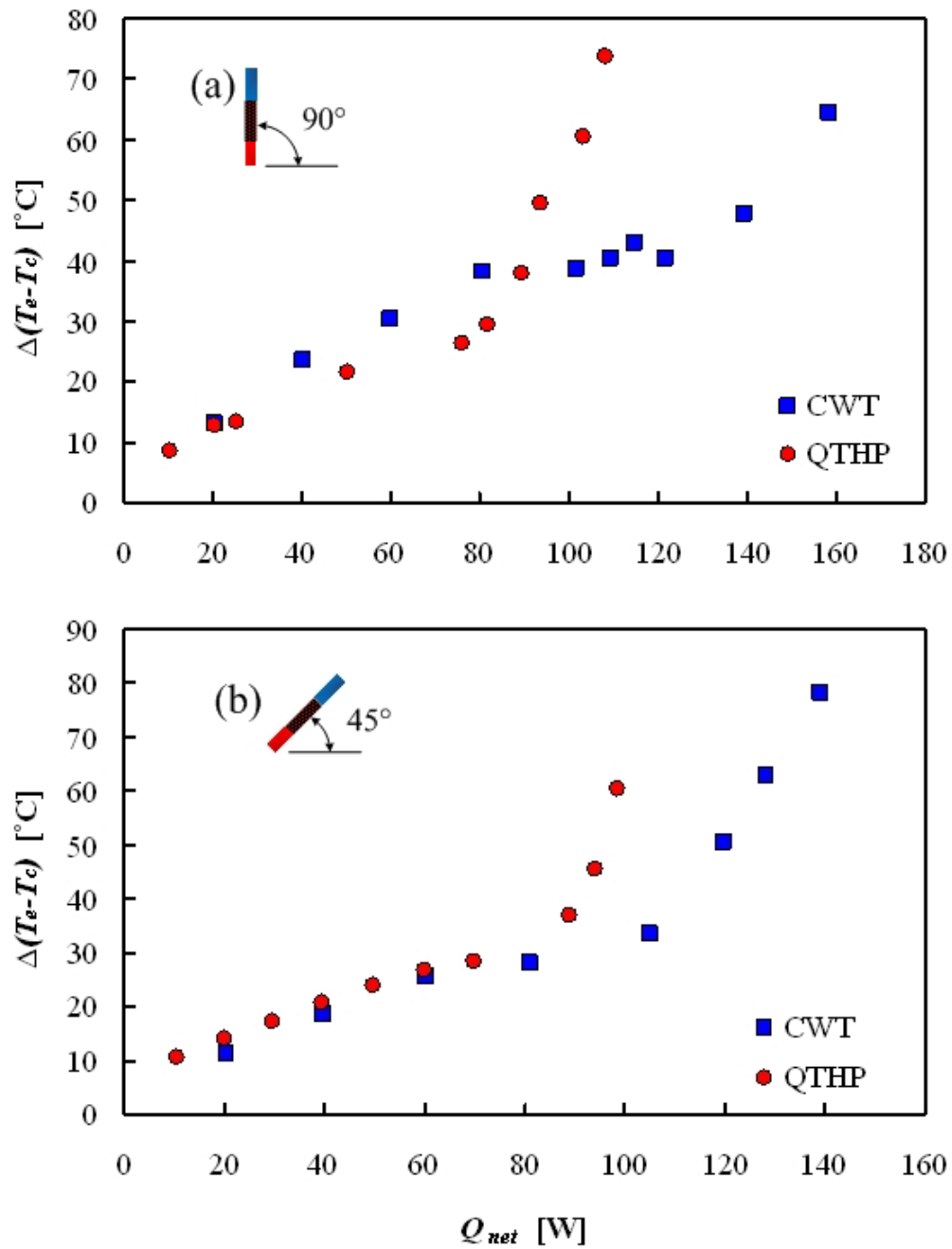
Fig. 29 Average results of the average temperature differences between the evaporator and condenser of the QTHP and CWT at the various net powers and inclination angles of (a) 90˚, (b) 45˚, and (c) 0˚.
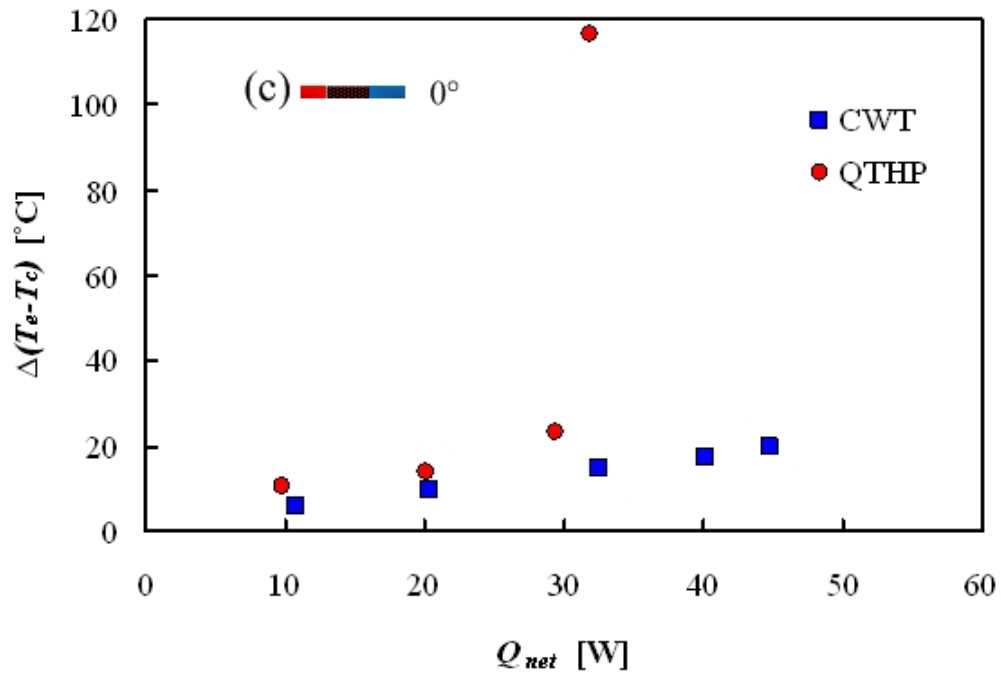
Fig. 29 (continued).

inclination angle of 90˚, as shown in Fig. 29(a). Unlike the results of the inclination angle of 90˚, the results of the QTHP at the inclination angles of 45˚ and 0˚ show the similar and slightly higher temperature differences for power levels up to 80W and 30W, respectively, as shown in Fig. 29(b) and 29(c). Even at the operating range of net rate of heat transfer of the evaporator, the thermal performance of the QTHP seems to be slightly more affected by the gravity than the CWT. Once the QTHP and the CWT start

to fail, the temperatures at the evaporator increase very rapidly, as the corresponding net

powers increase moderately.

Figure 30 shows the average temperature differences between the evaporator and

the condenser of the QTHP at the various net powers and inclination angles of 90˚, 45˚,

0˚, -45˚, and -90˚. As the QTHP is tilted, the operable average temperature difference

between the evaporator and condenser decreases rapidly. The excess supplied heat to the
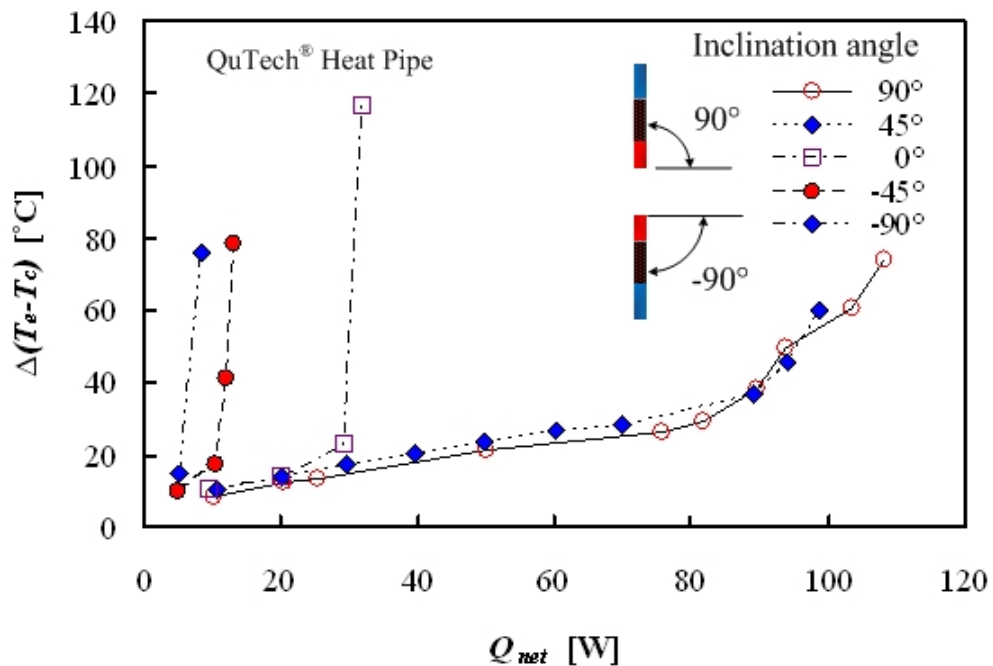
Fig. 30 Average temperature differences between the evaporator and the condenser of

the the QuTech[®] Heat Pipe at the various net rate of heat transfer to the evaporator and

inclination angles of 90˚, 45˚, 0˚, -45˚, and -90˚.

evaporator that is not transferred to the condenser, increases the temperatures of the evaporator in the QTHP. Eventually, the dry-out of the evaporator is shown as a rapid temperature increase in the evaporator.

Figure 31 shows the effective thermal conductivity ratios of the QTHP at various inclination angles of 90˚, 45˚, 0˚, -45˚, and -90˚. The maximum K_{eff}/K_{copper} of the QTHP is 70.4 times higher than the thermal conductivity of pure copper (391 *W/mK*) at the net rate of 75.8W and angle of 90˚. K_{eff}/K_{copper} and operable power ranges of the QTHP at the angles of 90˚ and 45˚ are similar. As the QTHP is tilted below an angle of 45˚, its thermal performance decreases rapidly. A maximum K_{eff}/K_{copper} of 34.9 at the angle of 0˚
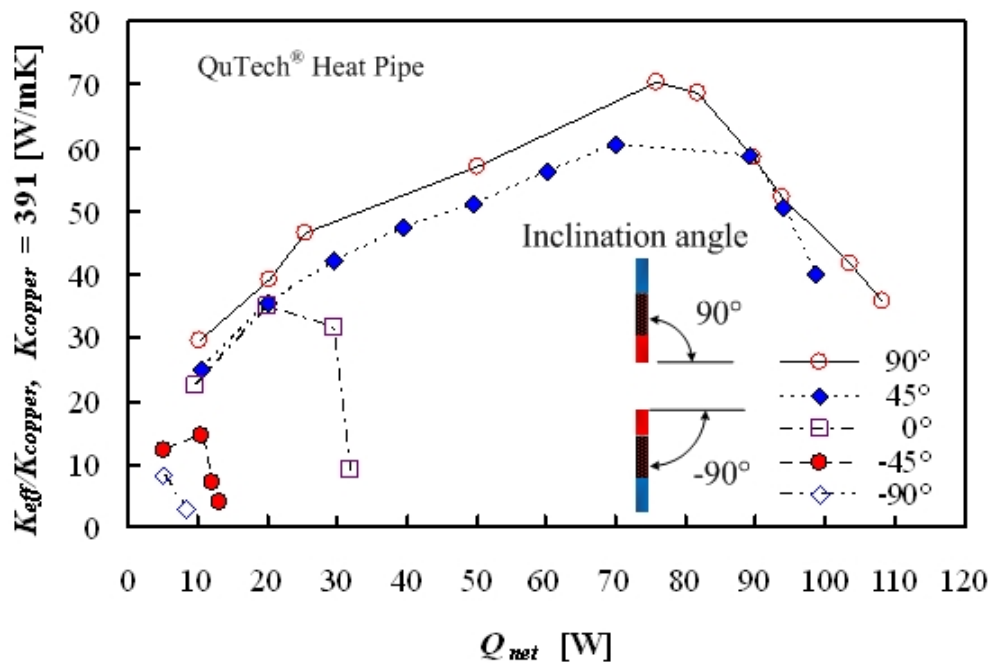
Fig. 31 Effective thermal conductivity ratios of the the QuTech[®] Heat Pipe at the various net rate of heat transfer to the evaporator and inclination angles of 90˚, 45˚, 0˚, -45˚, and -90˚.
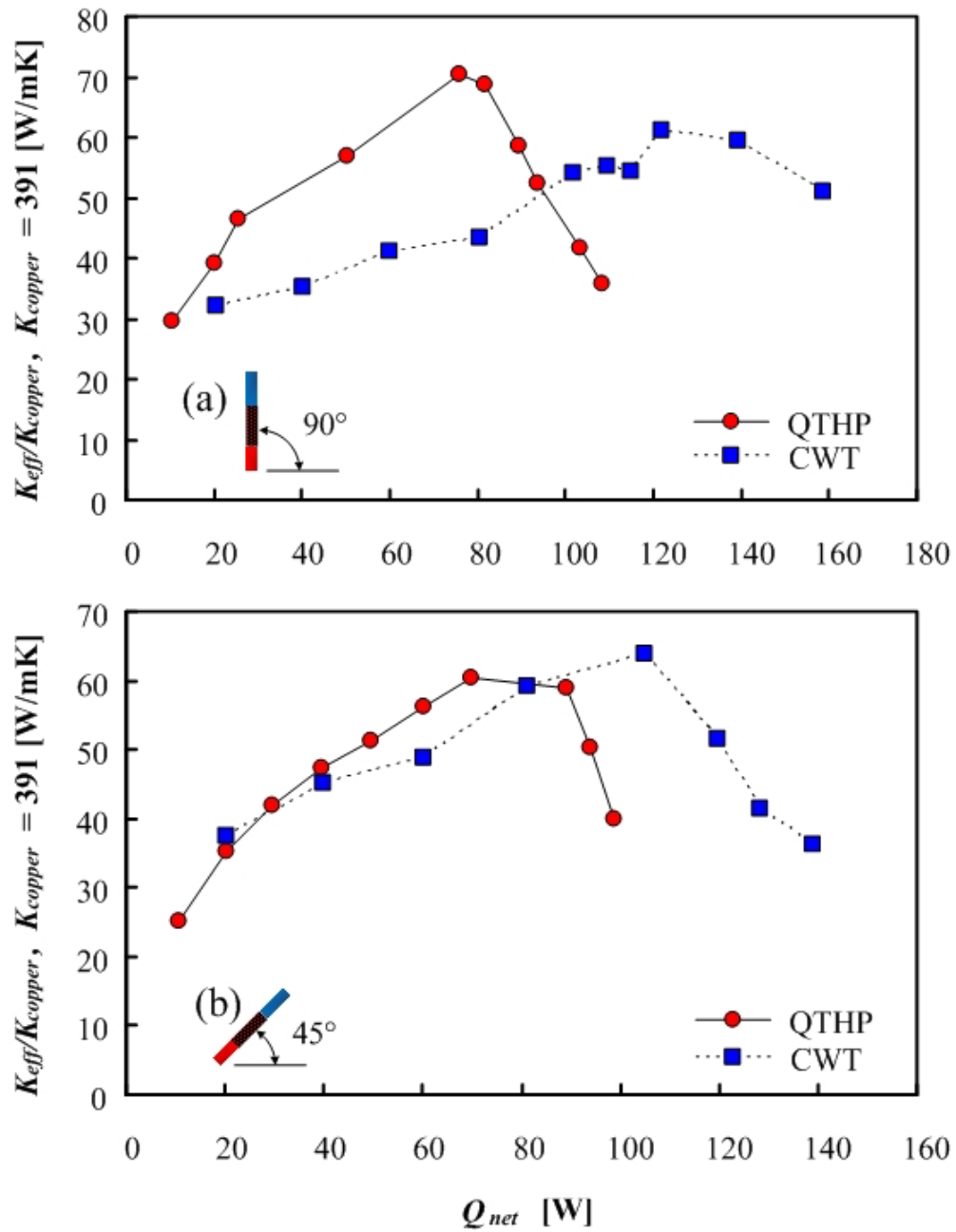
Fig. 32 Effective thermal conductivity ratios of the QuTech[®] Heat Pipe and the Noren[®] closed two-phase copper-water thermosyphon at various net powers and inclination angles of (a) 90˚, (b) 45˚, and 0˚.
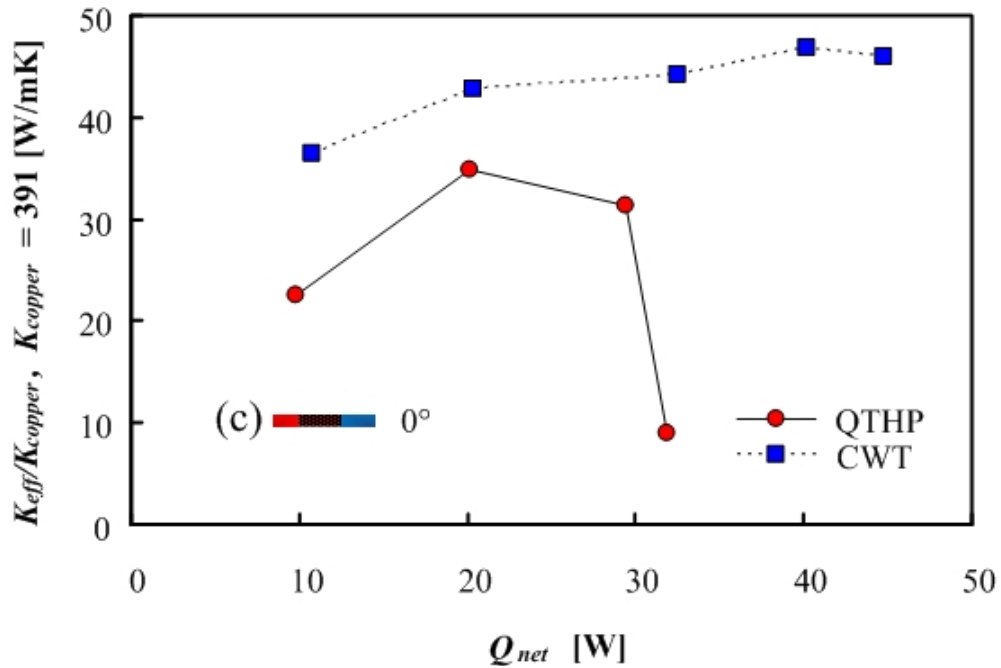
Fig. 32 (continued).

is two times lower than that of 70.4 at 90˚, at the corresponding net powers of 20.2W and 75.8W, respectively. At the angle of -90˚, the maximum operable power is only roughly 5W, achieving K_{eff}/K_{copper} of 8.3. However, unless the QTHP reaches its maximum thermal performance limit at a given angle, the QTHP seems to maintain its performance whether it is tilted or not, although its maximum limits of thermal performance and operable power range decrease dramatically as it is inclined against the gravity.

Figure 32 shows the comparison of K_{eff}/K_{copper} of the QTHP with K_{eff}/K_{copper} of the CWT at inclination angles of 90˚, 45˚, and 0˚. At the angle of 90˚, the QTHP has

maxima of 67% higher K_{eff}/K_{copper} than the CWT within the operating power range of up to 93.8W. Beyond 95W, K_{eff}/K_{copper} of the QTHP decreases rapidly while K_{eff}/K_{copper} of the CWT still increases up to the value of 61.2 at 121.8W. Notice that the peak performance of the QTHP is attained at 75.8W while that of the CWT at 128.1W, and the highest performance of the QTHP is 20% higher than that of the CWT. At the angle of 45°, the QTHP achieves very marginal performance over the CWT by up to 15% within the net powers of around 30 to 80W. At the angle of 0°, the CWT is superior to the QTHP regardless of the net powers. The comparison shows that the effect of the gravity on the QTHP is more severe than that on the CWT.

As mentioned earlier, "onset of nucleate boiling" in the CWT may occur in the net powers of 80W ~ 120W [see Fig. 29(a)]. Even when the operating power increases by 50%, the average temperature difference between the evaporator and the condenser of the CWT remains quite uniform. The results in Fig. 32(a) show a 41% enhancement of K_{eff}/K_{copper} of the CWT in the power range of 80 to 120W. In the case of the QTHP, on the contrary, the aforementioned randomness of the average temperature difference between the evaporator and the condenser does not seem to affect the thermal performance enhancement of the QTHP in the net powers of 80 to 100W. These random results of the average temperature difference might be instability of the QTHP before it fails unlike the instability of "onset of nucleate boiling" in the CWT.

3.2 THERMAL MECHANISMS OF A NOVEL HEAT PIPE

3.2.1 Presentation of Chemical Analysis Results

As mentioned earlier, the inside surface of the QuTech[®] Heat Pipe was claimed to be coated with three different layers with various combinations of inorganic materials [see Fig. 3]. Fig. 33 shows the actual solid compound that is coated on the entire inner surface of the QTHP and its Scanning Electron Microscopy (SEM) image that shows very high porosity. It is believed that the solid coatings inside the QTHP are not chemically adhered, but are physically adhered instead. Therefore, the adhesion among

(a) Macro view of Solid compound

(b) Scanning electron microscopy (SEM) image of solid compound (courtesy of the Center for Space Power)

Fig. 33 Solid compounds on the inner surface of the QuTech[®] Heat Pipe

chemical components in the coating would lead to weak bonding strengths among elements, which possibly leads to the high porosity condition.

When each QTHP was opened, a yellowish fluid (e.g., liquid) was observed. With the use of pH indicator test strips, the effluent in the QTHP was found to be a very strong base liquid of pH equal to 12 to 13. Upon further analysis on the yellow liquid with a Perkins Elmer Gas Chromatograph-Mass Spectrometry (GC-MS) instrument, by dissolving the effluent in methanol, CH_4O and injected into a GC-MS, the effluent was
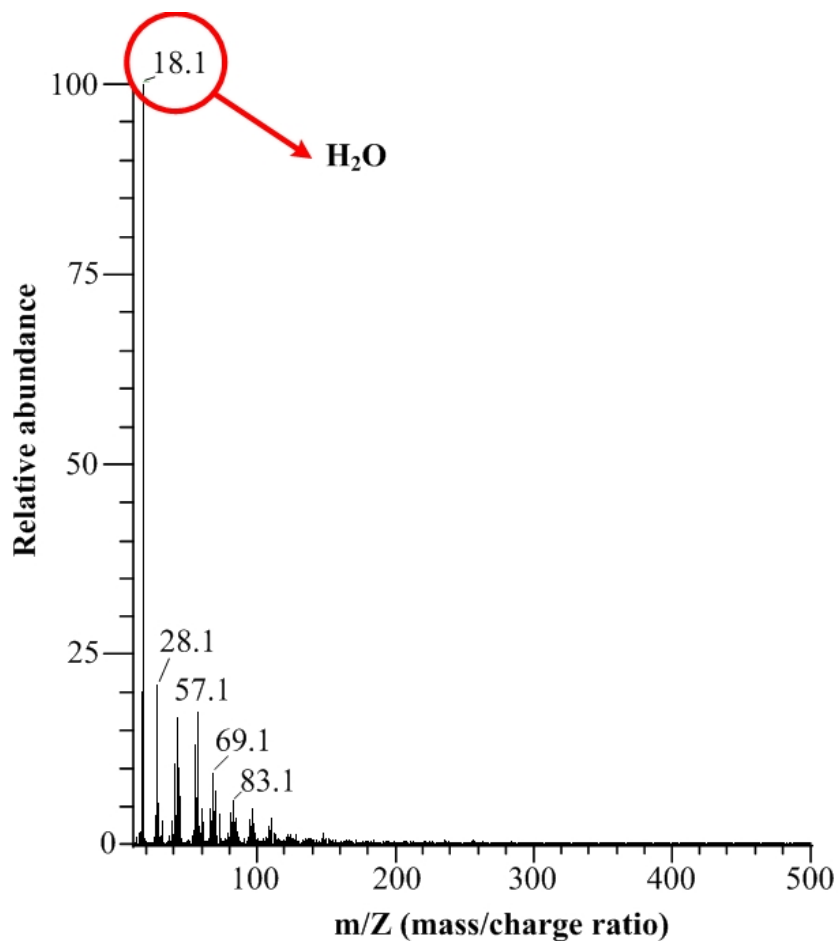
Fig. 34 Gas Chromatograph-Mass Spectrometry (GC-MS) results of the effluent in the QuTech® Heat Pipe

found to be mostly water, H_2O. In addition, several unidentified components that were not analyzable in GC-MS, as shown in Fig. 34, were observed.

In order to determine the unidentified components of the effluent from the GC-MS analysis, Inductively Coupled Plasma-Optical Emission Spectrometer (ICP-OES) was utilized. Table 5 shows the identified elements of the effluent with ICP-OES. All identified elements were inorganic elements that were not analyzable in the GC-MS. Most of the effluent was found to be water, H_2O which constituted 99.3 % of the sample's weight. Among other identified elements, potassium, K, phosphate, P, and

Table 5 Identified elements of the effluent in the QuTech® Heat Pipe with Inductively Coupled Plasma-Optical Emission Spectrometer (ICP-OES)

Element	K	P	Na	Cr	Cu	Si
M [g/mol]	39.098	30.974	22.990	51.996	63.546	28.086
[ppm]	2510.0	2530.0	1620.0	79.0	64.1	44.3
[weight %]	0.2510	0.2530	0.1620	0.0079	0.0064	0.0044
[mol %]	0.1160	0.1476	0.1273	0.0027	0.0018	0.0028

Element	Al	B	Ca	S	Zn
M [g/mol]	26.982	10.810	40.080	32.060	65.380
[ppm]	30.4	21.0	13.7	5.5	4.3
[weight %]	0.0030	0.0021	0.0014	0.0006	0.0004
[mol %]	0.0020	0.0035	0.0006	0.0003	0.0001

* ppm; micro-gram of elements per a gram of sample

sodium, Na, were the most abundant elements with the amount of 2510.0, 2530.0, and 1620.0 ppm (*µg* of element per *g* of sample), respectively. Also, other elements that were identified, but all were relatively small as compared to the amounts of the above mentioned three inorganic elements.

Based on the results obtained with GC-MS and ICP-OES, the effluent is believed to be an aqueous solution that contains dissolved inorganic ions, constituting 0.7 % by weight (0.4 % number of moles) of the sample. These inorganic ions were causing the pH value of 12 and 13 measured previously.

Table 6 Identified elements of the solid compounds in the QuTech® Heat Pipe with Inductively Coupled Plasma-Optical Emission Spectrometer (ICP-OES)

Element	Cu	Na	K	S	P	Fe	Ca
M [g/mol]	63.546	22.990	39.098	32.060	30.974	55.847	40.080
[ppm]	899000	98100	4900	4900	2450	2000	1160
[weight %]	88.3364	9.6394	0.4815	0.4815	0.2407	0.1965	0.1140
[mol %]	74.4461	22.4546	0.6595	0.8043	0.4162	0.1885	0.1523

Element	As	B	Pb	Cr	Mo	Al	Mg
M [g/mol]	74.922	10.810	207.200	51.996	95.940	26.982	24.305
[ppm]	981	981	981	777	490	490	490
[weight %]	0.0964	0.0964	0.0964	0.0763	0.0481	0.0481	0.0481
[mol %]	0.0689	0.4775	0.0249	0.0786	0.0269	0.0956	0.1061

* ppm; micro-gram of elements per a gram of sample

The QTHP's solid interior coating was also analyzed with ICP-OES. As shown in Table 6, the solid compound consisted mostly of copper, Cu, with the mole percentage of 74.45% of the total number of moles in the sample. Sodium, Na, constituted 22.45% of total number of moles in the sample. Other elements, as shown in Table 6, constituted a very small fraction of the sample. In summary, the results indicate that the solid compound of the inner wall of the QTHP consists mainly of copper, Cu, and sodium, Na.

In analyzing the solid compound with ICP-OES, the compound first needed to be decomposed into ions so that they could be detected and identified. In other words, the analysis of possible elements that might exist only on the surface could not be conducted with ICP-OES. The process of decomposition of the sample prevented it. To identify elements on the surface of the coating in contact with the QTHP's effluent, the Kratos
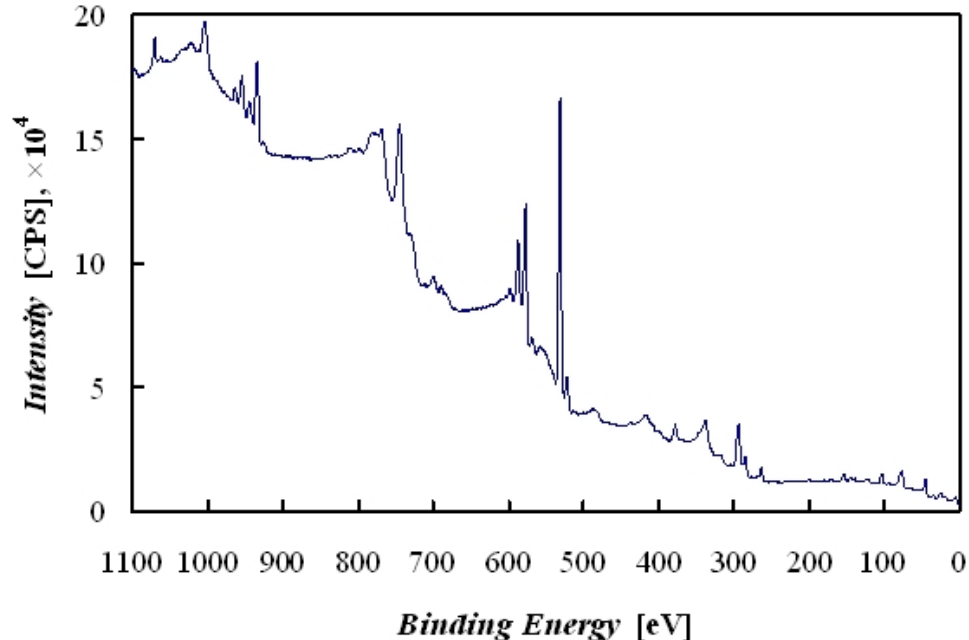
Fig. 35 Spectra of the elements on the surface of the solid compounds in the QuTech[®] Heat Pipe with X-Ray Photoelectron Spectroscopy (XPS)
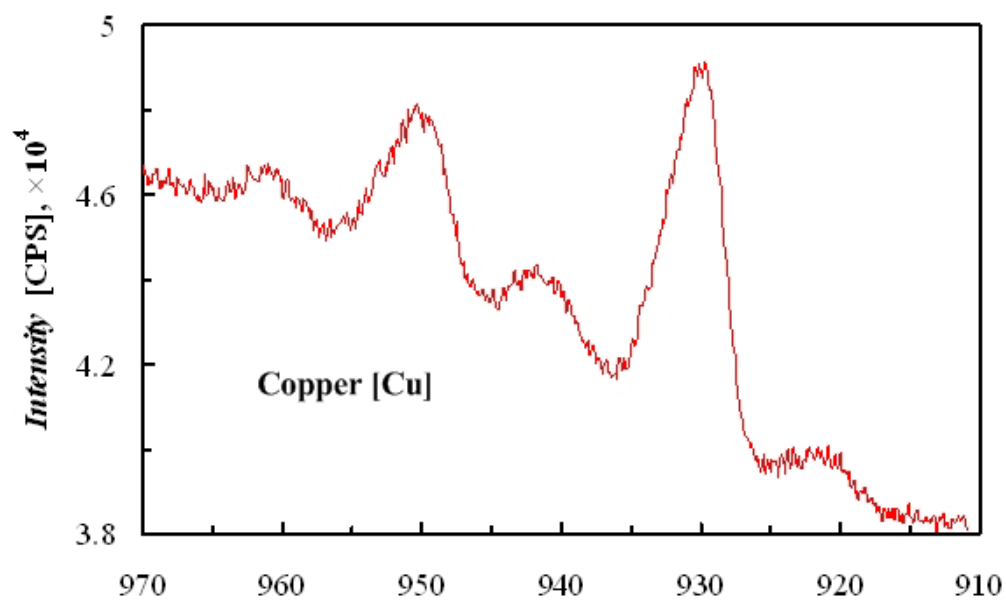
(a) Spectra of copper, Cu, on the surface
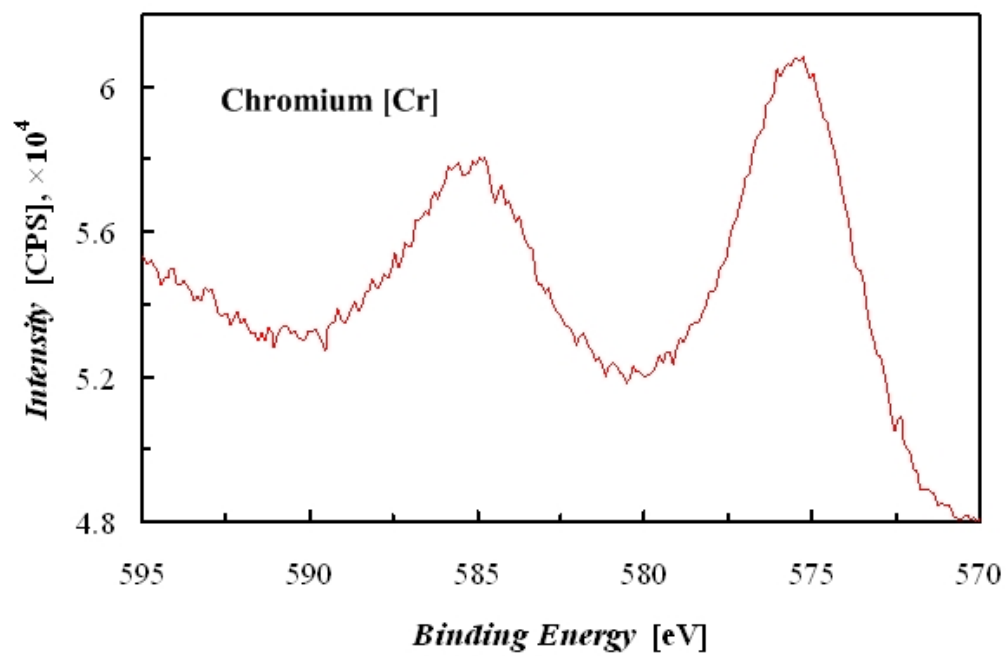
(b) Spectra of chromium, Cr, on the surface

Fig. 36 Spectra of the specific elements on the surface of the solid compounds in the

QuTech® Heat Pipe with X-Ray Photoelectron Spectroscopy (XPS)
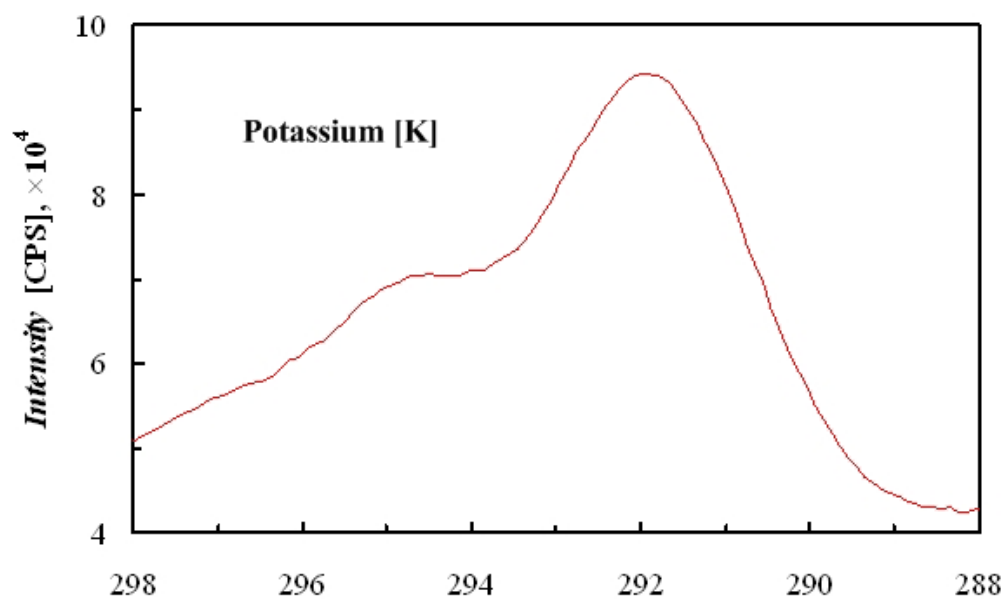
(c) Spectra of potassium, K, on the surface
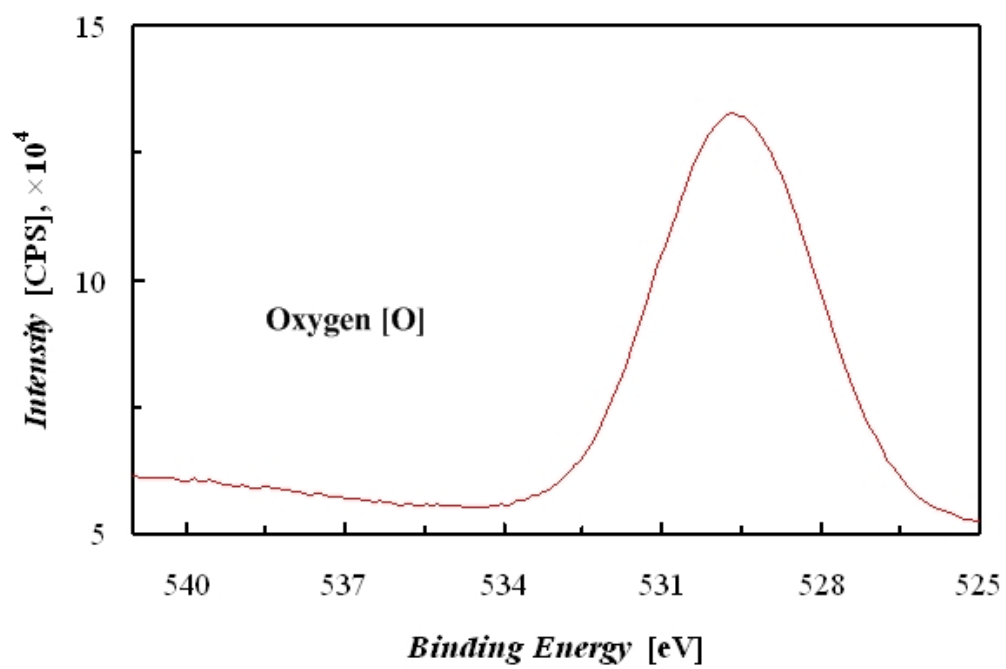
(d) Spectra of oxygen, O, on the surface

Fig. 36 (continued)
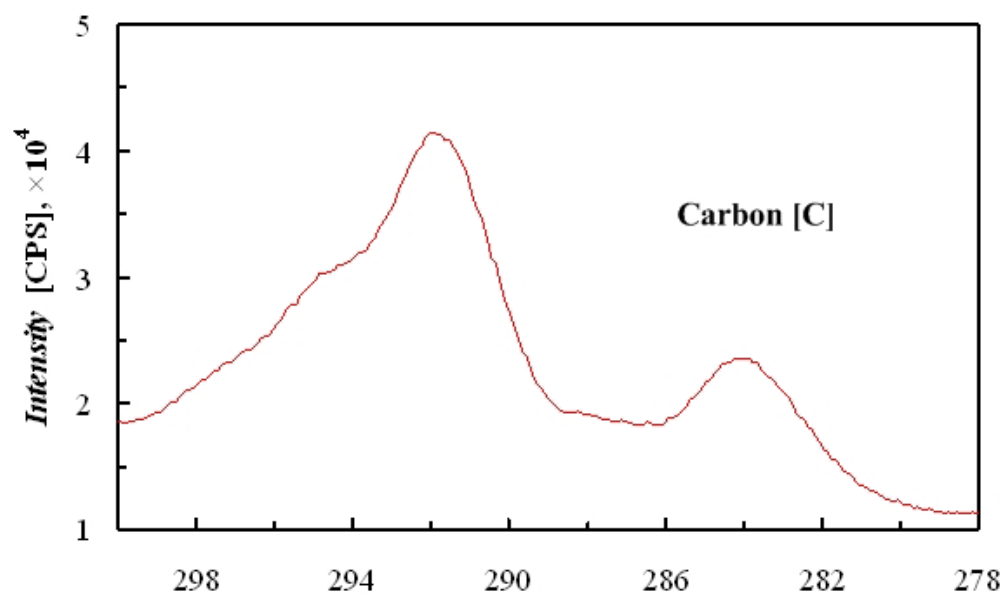
(e) Spectra of carbon, C, on the surface
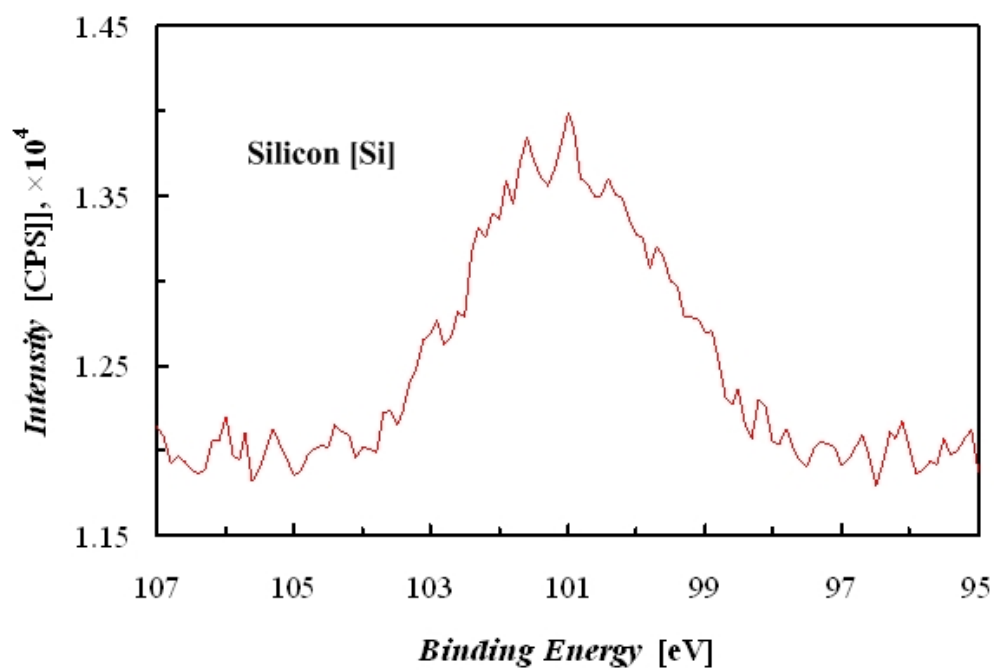
(f) Spectra of silicon, Si, on the surface

Fig. 36 (continued)

Axis Ultra X-Ray Photoelectron Spectroscopy (XPS) with magnesium, Mg, as an anode was used. Figures 35 and 36 show the overall and specific spectra of the identified elements on the surface of the solid compound in the QTHP respectively. The spectra are based on the strengths of intensities of the X-ray and are related to the binding energies of electrons of each element.

Table 7 shows the estimated atomic concentration of each element based on the spectra [Fig. 35 and 36]. The most abundant element is oxygen, O, with the amount of 54.56%, followed by carbon, C, potassium, K, chromium, Cr, and copper, Cu, in the amounts of 13.89, 10.30, 10.27, and 5.58%, respectively. Even though carbon, C, occupies 13.89% of the surface elements of the sample, it could be easily varied. This is because carbon can be easily attached onto the sample from the atmosphere during a preparation of the sample.

X-ray powder Diffraction (XRD) was utilized to obtain the structural information of the crystalline solid compounds of the QTHP. Fig. 37 shows the X-ray pattern of the solid compound powder. This is clearly a pattern of copper oxide, Cu_2O. From the analysis, the major component of the solid compound is Cu_2O, containing other inorganic elements such as Na, P, K, etc. [see Table 6]

Table 7 Concentration of the identified elements on the surface of the solid compounds in the QuTech® Heat Pipe with X-Ray Photoelectron Spectroscopy (XPS)

Peak	Position BE [eV]	Atomic Mass [g/mol]	Atomic Concentration [%]	Mass Concentration [%]
Cu 2p	932.233	63.549	5.58	14.33
Cr 2p	576.317	51.996	10.27	21.51
O 1s	530.400	15.999	54.56	35.32
K 2p	295.233	39.102	10.30	16.34
Na 1s	1069.567	22.990	1.88	1.76
C 1s	284.733	12.011	13.89	6.75
Si 2p	101.650	28.086	3.53	4.00
Total			100.00	100.00
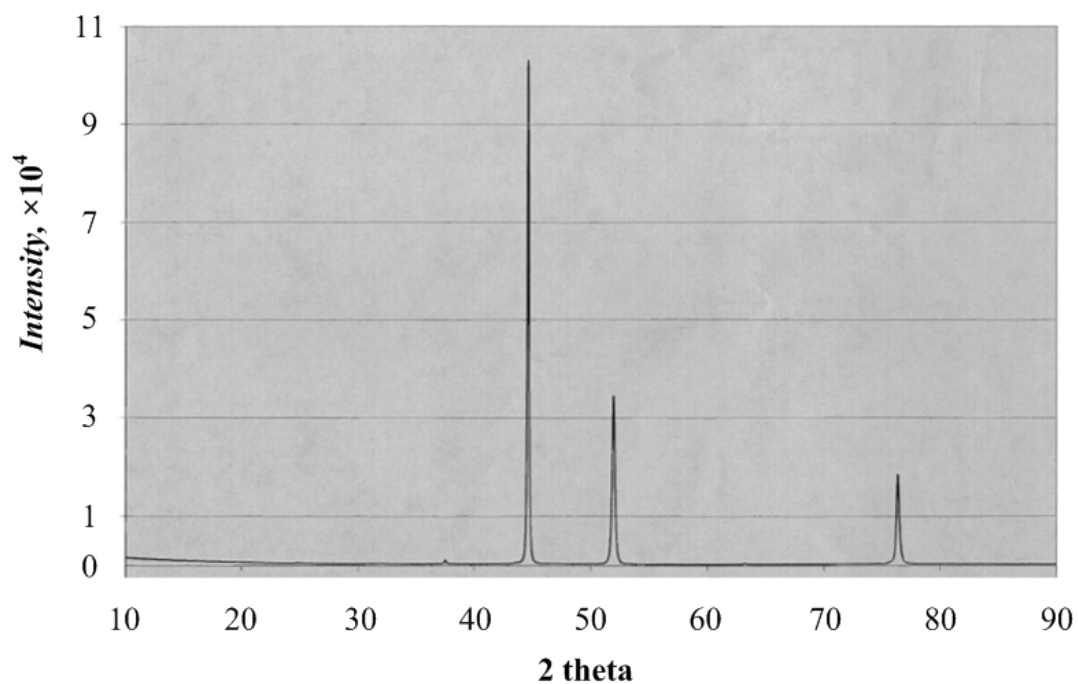
Fig. 37 X-ray powder diffraction (XRD) pattern of the solid compound powder in the QuTech® Heat Pipe with X-ray diffractometry

3.2.2 Presentation of Thermal Analysis Results

To investigate the thermal characteristics of the QTHP's solid coating and its aqueous effluent, which were analyzed for their elemental composition, a Differential Scanning Calorimetry (DSC) was employed in an attempt to gain insight into possible thermal transport mechanisms. Fig. 38 shows the results of the thermal analysis conducted on the QTHP's coating samples from 25˚C to 500˚C in steps of 5 and 10˚C/min for the heating and cooling stage, respectively. Hydrated samples (coating samples that were in contact with the tube's effluent) were prepared to minimize evaporation losses in the air. The hydrated samples were either tested immediately or placed in glass containers to minimize exposure to air. The solid samples taken from the QTHP were hydrated in the yellowish aqueous solution, which is mostly water as seen in Fig. 34 and Table 5. The result of the hydrated sample with an initial weight of 48.90 *mg* is shown in Fig. 38(a). The results from DSC indicates that an endothermic reaction or phase change phenomena occurred at a peak temperature of about 92˚C, when the sample was heated from room temperature (25˚C) to 500˚C in steps of 5˚C/min. Once the maximum temperature of 500˚C was achieved, the sample was allowed to cool from 500˚C to room temperature in steps of 10˚C/min. During the cool down phase, no chemical reaction or phase change phenomena was observed. After the test, the sample lost 6.40 mg, or 13% of its initial weight. A second sample with an initial weight of 71.90 *mg* was prepared. The sample was initially exposed to air for five hours. Afterwards, the sample was tested in the DSC with the same testing temperature
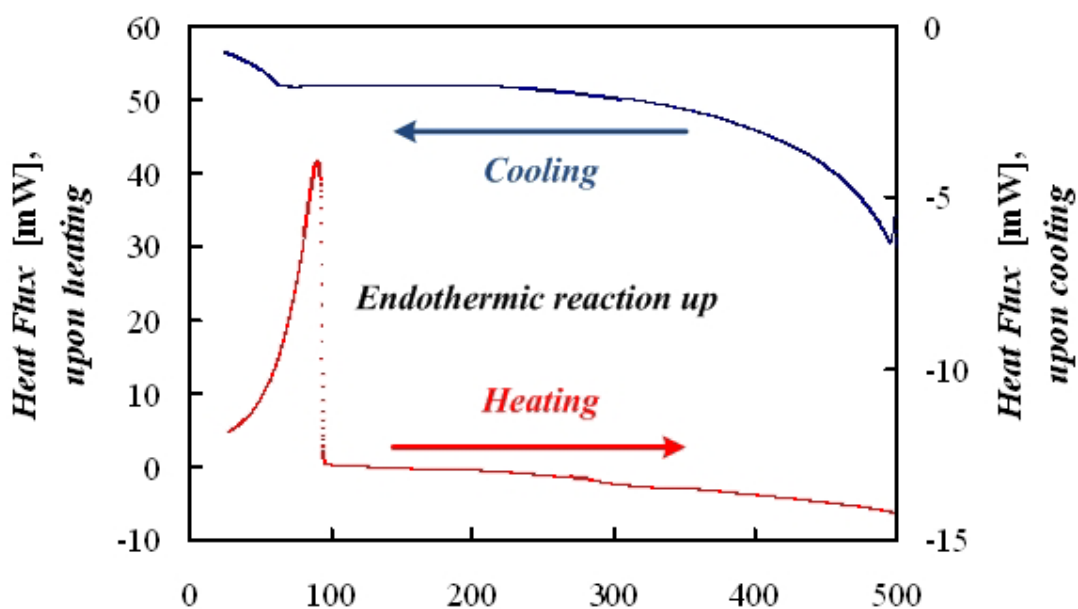
(a) Sample of solid coating wet with the effuent
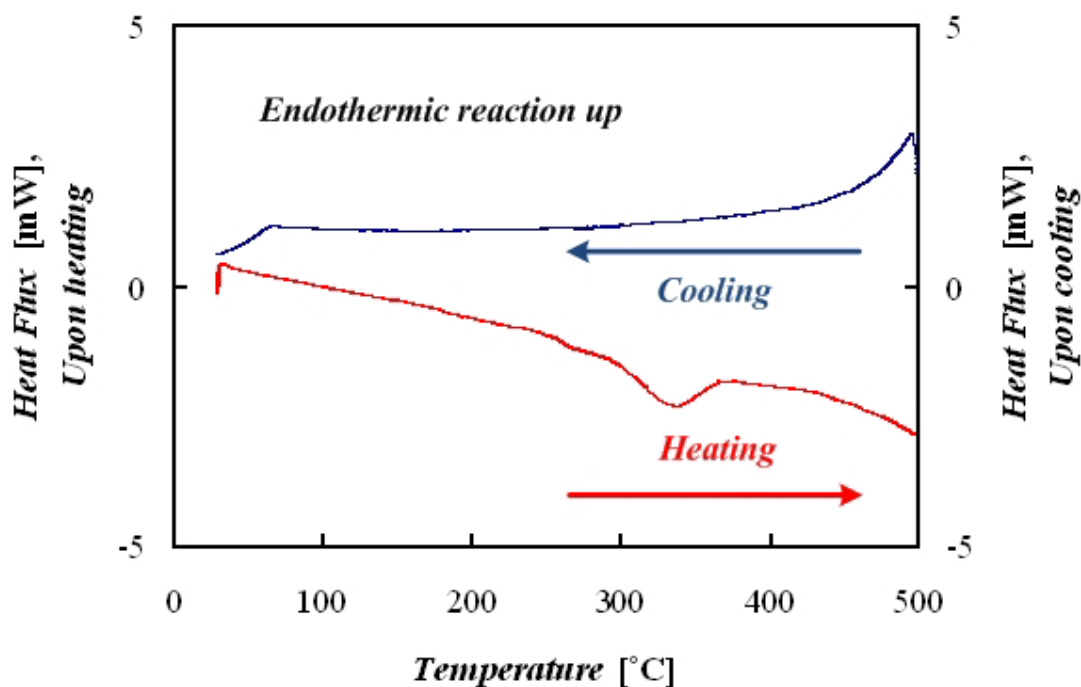
(b) Sample of solid coating exposed in air

Fig. 38   Thermal analysis on solid compounds and the effluent of the QuTech® Heat
Pipe with Differential Scanning Calorimetry (DSC)

between 25 and 500˚C, as shown in Fig. 38(b). When the sample was heated in steps of 5˚C/min, there was no endothermic reaction or phase change that was observed in the first sample (the hydrated solid compounds with the effluent). However, an exothermic reaction at around 340˚C was observed, indicating that chemical compositions of the solid compounds were permanently altered. When the sample was cooled down to 25˚C from 500˚C in steps of 10˚C/min, there was no reaction or phase change observed. After the test, no weight loss was observed for the second sample (the solid compounds exposed in air for five hours).

From the observed results as seen in Fig. 38, for the QTHP to work properly, an aqueous solution must be present. An interaction may exist between the solid coating compound and the aqueous solution.

With the thermal analysis data presented in Fig. 38(a), an attempt was made to determine the magnitude of the rate of heat transfer had been generated during the chemical reaction or phase change portion of the curve between 25˚C and 100˚C, with MATLAB. The calculated result gives a rough estimation of the required enthalpy related to the reaction or phase change since the results didn't fully cover the entire reaction or phase change from the beginning at 25˚C. The enthalpy change associated with the chemical reaction or phase change phenomena was calculated to be 14.4 J. This is very similar to the enthalpy change required for pure water, i.e., 14.0 J, assuming that pure water was fully responsible for the 6.40 mg weight loss. This gives further evidence that a phase change phenomena that involves an aqueous solution is the heat transfer mechanism for this device.

To further investigate thermal characteristics of the solid compounds and the effluent, four different samples (Cases S1~S4), of solid compounds of the QTHP, were prepared and tested with a DSC, as shown in Table 8. Case S1 was prepared with the solid compounds containing the effluent and was tested immediately after cutting of the QTHP. Case S2 allowed the sample to be exposed in air for two hours. Cases S3 and S4 were prepared such that after being exposed in air for several hours, the samples were soaked in the effluent and distilled water, respectively.

Table 8 Results of changes of weight and phase change temperatures of four different samples, Case S1~S4, tested in DSC

Case		S1	S2	S3	S4
Sample preparation		Hydrated in the effluent	Dehydrated	Re-hydrated in the effluent	Re-hydrated in pure water
Initial weight [mg]		17.16	16.29	13.73	15.75
Final weight [*mg*]		15.30	16.27	11.72	10.46
Weight loss [*mg*]		1.86	0.02	2.01	5.29
Weight Loss [%]		10.84	0.12	14.64	33.59
Melting	Onset	-1.0		-0.6	0.2
[˚C]	Peak	2.2		2.5	5.7
Evaporation	Onset	44.9		49.2	58.8
[˚C]	Peak	68.0		73.0	89.7

Fig. 39 shows the results of each case listed in Table 8 with a temperature range between -40˚C to 200˚C in steps of 5˚C/min for heating. Although thermal analysis upon cooling was conducted in steps of 5˚C/min, there were no observed chemical reactions or phase changes, which were observed in the previous thermal analysis [see Fig. 38]. On the basis of prior DSC test runs, the starting temperature was chosen so that the full chemical reaction or phase change portion could be captured. In Cases S1 and S3, the onset and peak temperatures of evaporation were similar. The onset temperature for evaporation for Cases S1 and S3 with the QTHP effluent began at 44.9˚C and 49.2˚C,
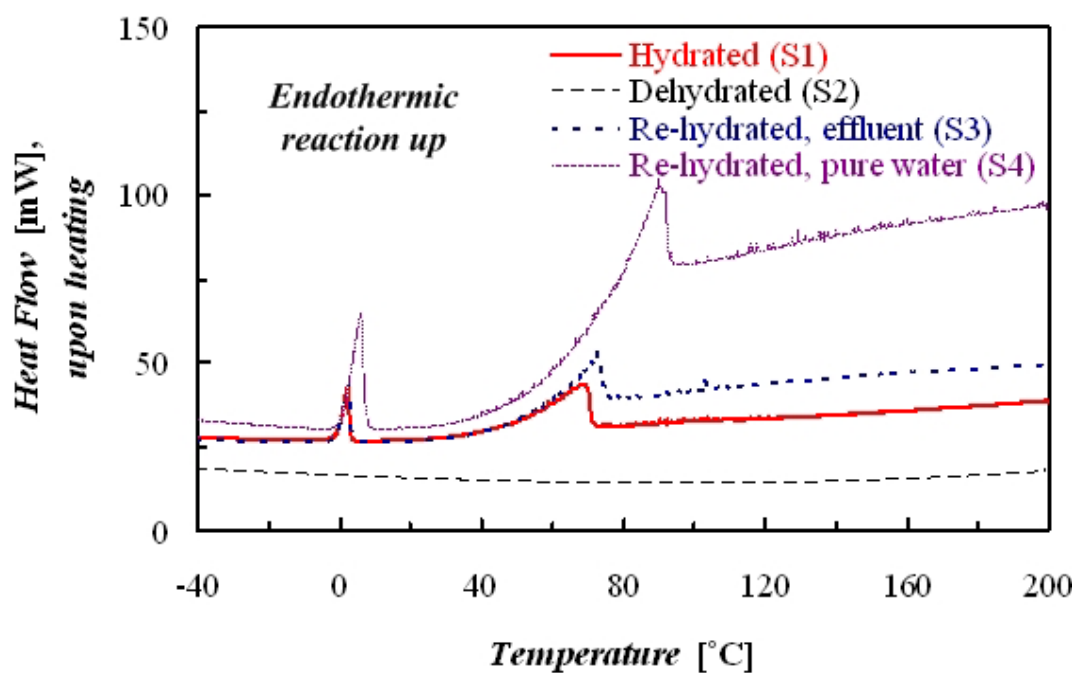
Fig. 39 Thermal analysis on the solid compounds and the effluent of the QuTech[®] Heat Pipe with Differential Scanning Calorimetry (DSC), as tabulated in Table 8

respectively, as shown in Table 8. On the contrary, Case S4, which was prepared with re-hydrated QTHP coating sample by being soaked in distilled water, showed an onset temperature of evaporation of 58.8°C. By replacing the QTHP effluent with distilled water, the onset of evaporation occurred at a higher temperature.

One possible thermal mechanism to shift the onset and peak temperature of evaporation might be the interaction between the solid compounds and the effluent of the QTHP. The re-hydrated sample of the solid compounds with distilled water (Case S4) showed the delay of the onset and peak temperatures of the evaporation of distilled water of 58.8 and 89.7°C, respectively. The onset and peak temperatures of the hydrated (Case S1) and re-hydrated sample (Case S3) with the effluent were 44.9 and 68.0°C and 49.2 and 73.0°C, respectively. On the other hand, considering the weight loss of each case, which water in the effluent (Case S1 and S3) and distilled water (Case S4) were responsible for, it was possible to have a 'smearing effect' (thermal response lag between heating rates and temperatures of samples) [46] during DSC tests due to the different amount of water in the samples; Case S1 that was originally wet with the effluent in the QTHP had the lowest onset and peak temperatures, while the sample had smallest amount of water of 10.84% of the initial weight. Case S2 that was soaked in the effluent had a slight higher onset and peak temperatures than those of Case S1, with the initial water amount of 14.64% of the initial weight. Case S4 that was soaked in distilled water had the highest onset and peak temperatures than any other cases with the initial water amount of 33.59% of the initial weight. Case S3, however, was prepared with the same procedure as Case S4, which was fully soaked in the effluent for several hours.

Although the solid compounds should absorb approximately the same amount of water compared with the sample soaked in distilled water (Case S4), weight losses of Case S3 and S4 were 14.64 and 33.59%, respectively. This is 2.3 times higher water absorption of the sample than the effluent absorption of the sample. From the observation, the interaction between the elements of the effluent and the solid compounds (see Tables 5 and 7) might prevent absorption of water into the solid compounds. In other words, when dissipated heat is applied into the solid compounds through the outer surface of QTHP, vaporization of water, due to the absorbed thermal energy, might occur easily. This is because less water molecules are packed into the solid compounds.

3.2.3 Discussion on Results of Chemical/Thermal Analysis

For the QTHP to run properly, it has to contain effluent which was mostly water, H_2O. In order to transport the thermal energy, which was applied to the evaporator, to the condenser of the QTHP, vapor flow is first generated from the vaporization of liquid. It is driven by a pressure difference between the evaporator and the condenser. This is similar to the transport mechanism for conventional heat pipes or closed two-phase thermosyphons. As tabulated in Tables 5, 6, and 7, and shown in Fig. 35 and 36, however, the QTHP contains various elements other than copper, Cu, and water, H_2O. These are not used in conventional heat pipes and closed two-phase thermosyphons. Although the elemental information obtained with GC-MS, ICP-OES, and XPS is not

enough to determine the exact chemical compositions, but all identified elements are mostly inorganic (metallic) elements that can be ionized in aqueous solution, especially water, H_2O. All these elements in the effluent of the QTHP act as salts (mostly inorganic salts) in the aqueous solution. When salts are dissolved in water, non-volatile salts cause the vapor pressure of the solution to be lower than that of pure water. This lowered vapor pressure of the solution delays vaporization (boiling) of water until the vapor pressure of the solution reaches the ambient pressure. This causes the solution to vaporize (boil) at a higher temperature than the boiling temperature of pure water upon heating. The results of the solid compounds and the effluent in the QTHP with DSC, however, show that the vaporization of water molecules on the solid compounds along with the elements other than water in the effluent of the QTHP may occur at lower temperature than vaporization of pure water molecules [see Table 8 and Fig. 39]. The paradox between the inorganic salts in the effluent and the results of DSC may lead to a conclusion that inorganic salt hydrates were placed in the QTHP device.

Inorganic salt hydrates have been widely used as latent heat storage materials. They have been used as phase change materials (PCM) that utilize phase change between solid and liquid state to absorb thermal energy and release their stored energy. A few applications are solar energy, industrial waste heat, etc. Advantage of phase change materials to store thermal energy is that they require relatively small volume, compared to non-phase-change materials, at specific temperature regions. Sharma and Sagara [47] reviewed possible materials of PCMs as latent heat storage materials and systems that use latent heat storage materials at relatively low temperatures between 0˚C

and 200°C, especially up to 100°C such as paraffins (C_nH_{2n+2}), fatty acids ($CH_3(CH_2)_{2n}COOH$), salt hydrates, and eutectics. In those selected PCMs, salt hydrates are inorganic compounds that are loosely bonded to a specific amount of water, depending on kinds of inorganic salt. Advantage of salt hydrates is that they have a relatively sharp melting point and high thermal conductivity, compared with other PCMs. This allows for the storage volume to be minimized to store thermal energy. Disadvantage of salt hydrates is that most of salt hydrates melt and solidify incongruently, which means that dehydrated salt can be segregated by density difference between hydrated salt and dehydrated salt, preventing dehydrated salt from being hydrated salt [47]. Abhat [48] tested thermal characteristics and cycles of PCMs with Thermal Analysis (TA) and Differential Scanning Calorimetry (DSC). He tested inorganic salt hydrates such as $Na_2HPO_4 \cdot 12H_2O$, $Na_2S_2O_3 \cdot 5H_2O$, and $CaCl_2 \cdot 6H_2O$. He reported all tested inorganic salt hydrates suffered from supercooling (freezing at several degrees below thermodynamic freezing point) and degradation of capability as a latent heat storage material upon several thermal cycles due to segregation of salts by density difference, as mentioned earlier. Mu and Perimutter [49] analyzed thermal decomposition of inorganic sulfates hydrates, $M_x(SO_4)_y \cdot nH_2O$ (M and n denotes inorganic elements and number of water molecules per 1 molecule of inorganic salt, respectively), with a thermogravimetric analyzer (TGA), a differential scanning calorimetry (DSC), and a differential thermal analyzer (DTA). They tabulated initial and final decomposition temperatures of each tested inorganic salt hydrates. For example, $Al_2(SO_4)_3 \cdot 16H_2O$ started to decompose at 25°C and ended at 70°C.

Table 9 Thermal and physical properties of inorganic salt hydrates [52]

Formula	Mol. weight	M. P. [°C]	Density [g/cm^3]
$Na_2SO_4 \cdot 10H_2O$	322.196	32.0	1.46
$Na_2CO_3 \cdot 10H_2O$	286.142	34.0	1.46
$Na_2HPO_4 \cdot 12H_2O$	358.143	35.0	1.50
$FeCl_3 \cdot 6H_2O$	270.295	37.0	1.82
$CaS_2O_3 \cdot 6H_2O$	260.298	45.0	1.87
$Na_2S \cdot 9H_2O$	240.183	50.0	1.43
$Na_3(PO_3)_3 \cdot 6H_2O$	413.976	53.0	1.79
$NaAl(SO_4)_2 \cdot 12H_2O$	458.281	60.0	1.61
$NaH_2PO_4 \cdot 2H_2O$	156.008	60.0	1.91
$Cr(NO_3)_3 \cdot 9H_2O$	400.148	66.3	1.80
$Al(NO_3)_3 \cdot 9H_2O$	375.134	73.0	1.72
$Na_3PO_4 \cdot 12H_2O$	380.124	75.0	1.62
$Al(ClO_4)_3 \cdot 9H_2O$	487.471	82.0	2.00
$Na_2Cr_2O_7 \cdot 2H_2O$	297.999	85.0	2.35
$Al_2(SO_4)_3 \cdot 18H_2O$	666.426	86.0	1.69
$CrK(SO4)_2 \cdot 12H_2O$	499.403	89.0	1.83
$AlBr_3 \cdot 6H_2O$	374.785	93.0	2.54
$KAl(SO_4)_2 \cdot 12H_2O$	474.389	100.0	1.72
$(NH_4)2Fe(SO_4)_2 \cdot 6H_2O$	392.139	100.0	1.86
$AlCl_3 \cdot 6H_2O$	241.432	100.0	2.40
$NH_4MgCl_3 \cdot 6H_2O$	256.794	100.0	1.46

Table 10 Estimated amount of inorganic salt hydrates to release $1ml$ H_2O as working

fluid based on densities that tabulated in Table 9

Formula	M. P. [°C]	Mol. Hydrate/ Mol. H_2O	[g] per Mol. H_2O	[g] per 1 ml H_2O	[ml] per 1 ml H_2O
$Na_2SO_4 \cdot 10H_2O$	32.0	0.10	32.22	1.78	1.22
$Na_2CO_3 \cdot 10H_2O$	34.0	0.10	28.61	1.58	1.08
$Na_2HPO_4 \cdot 12H_2O$	35.0	0.08	29.85	1.65	1.10
$FeCl_3 \cdot 6H_2O$	37.0	0.17	45.05	2.49	1.37
$CaS_2O_3 \cdot 6H_2O$	45.0	0.17	43.38	2.40	1.28
$Na_2S \cdot 9H_2O$	50.0	0.11	26.69	1.48	1.03
$Na_3(PO_3)_3 \cdot 6H_2O$	53.0	0.17	69.00	3.81	2.14
$NaAl(SO_4)_2 \cdot 12H_2O$	60.0	0.08	38.19	2.11	1.31
$NaH_2PO_4 \cdot 2H_2O$	60.0	0.50	78.00	4.31	2.26
$Cr(NO_3)_3 \cdot 9H_2O$	66.3	0.11	44.46	2.46	1.37
$Al(NO_3)_3 \cdot 9H_2O$	73.0	0.11	41.68	2.30	1.34
$Na_3PO_4 \cdot 12H_2O$	75.0	0.08	31.68	1.75	1.08
$Al(ClO_4)_3 \cdot 9H_2O$	82.0	0.11	54.16	2.99	1.50
$Na_2Cr_2O_7 \cdot 2H_2O$	85.0	0.50	149.00	8.24	3.51
$Al_2(SO_4)_3 \cdot 18H_2O$	86.0	0.06	37.02	2.05	1.21
$CrK(SO4)_2 \cdot 12H_2O$	89.0	0.08	41.62	2.30	1.26
$AlBr_3 \cdot 6H_2O$	93.0	0.17	62.46	3.45	1.36
$KAl(SO_4)_2 \cdot 12H_2O$	100.0	0.08	39.53	2.19	1.27
$AlCl_3 \cdot 6H_2O$	100.0	0.17	40.24	2.22	0.93
$(NH_4)2Fe(SO_4)_2 \cdot 6H_2O$	100.0	0.17	65.36	3.61	1.94
$NH_4MgCl_3 \cdot 6H_2O$	100.0	0.17	42.80	2.37	1.62

Ghule et al. [50 and 51] studied dehydration of $Na_3PO_4 \cdot 12H_2O$ and $Na_2HPO_4 \cdot 12H_2O$, respectively. They observed that the two inorganic salt hydrates were gone through decomposition by releasing fraction of total water molecules that the salts were bonded to at the specific several different temperature ranges upon heating, before the salt were totally anhydrous. Sharma et al. [53 and 54] also reported thermal decompositions of various sodium salt hydrates.

With the thermal analysis of the solid compounds and the effluent of the QTHP, as tabulated in Table 8 and shown in Fig. 38 and 39, and the identified inorganic salt on the solid compounds and in the effluent of the QTHP, as tabulated in Tables 5, 6, and 7 and shown in Fig. 35 and 36, it might be possibly drawn that inorganic salt hydrates were involved in thermal transport mechanism as well as water itself, as mentioned earlier. All identified elements were mostly inorganic salt that were easily dissolved in water. Moreover, vaporization of water might have occurred below thermodynamic boiling temperature of water when possibly involved inorganic salts were anhydrous at the melting temperature.

When inorganic salt hydrates are involved in heat pipes/thermosyphons, thermal performance of heat pipes/thermosyphons might increase with additional latent heat of fusion energy of salt hydrates and energy required to release water molecules from salt hydrates by the presence of inorganic salt hydrates in heat pipes. Upon the examination of the QTHP, more conclusions could not be easily drawn since it was impossible to know the exact manufacturing process and elements that were placed in the QTHP.

Selected inorganic salt hydrates are tabulated in Table 9 with their melting temperatures and densities based on their melting temperatures. Inorganic salt hydrates with low melting temperatures within 0°C and 100°C are suitable for applications of electronics cooling. The amount of inorganic salt hydrates required to release 1 *ml* of water as working fluid is calculated and tabulated in Table 10, when these inorganic salt hydrates are used for working medium to generate water to transport thermal energy from an evaporator to a condenser of heat pipes and thermosyphons.

CHAPTER IV

SUMMARY AND CONCLUSIONS

In order to meet ever-increasing thermal dissipation requirements of gas turbine airfoils and CPUs, an internal cooling channel for gas turbine airfoils and a novel heat pipe for electronic cooling application were studied. First, heat (mass) transfer distributions in a two-pass trapezoidal channel with a 180-degree turn were obtained. The two-pass trapezoidal channels modeled internal cooling channels of gas turbine airfoils. Second, a novel heat pipe was studied as an alternative to current heat pipes/thermosyphons, in order to dissipate thermal energy from smaller and higher-powered CPUs.

4.1 HEAT (MASS) TRANSFER DISTRIBUTIONS IN A TWO-PASS TRAPEZOIDAL CHANNEL WITH A 180-DEGREE TURN

Naphthalene sublimation experiments were conducted and the heat and mass transfer analogy was used to study the local heat transfer distributions on one of the two primary walls of a trapezoidal channel with a 180° turn. Results were obtained for turbulent air flow through the channel with smooth walls, and with ribs on one wall and

on two opposite walls, over a range of Reynolds numbers between about 10,000 and 60,000. Based on the geometries of the test channel and the conditions of the experiments, the results may be summarized as follows:

1. The effect of ribs on the average heat (mass) transfer is higher when air enters larger straight section of the trapezoidal channel than when air enters smaller straight section of the channel. Whether ribs are installed on one wall or two walls and with air entering larger or smaller straight section of the channel, the enhancement of the average heat (mass) transfer at the turn region is lower than the enhancement of the average heat (mass) transfer at the straight section of the channel.

2. There was a very large variation of the local heat (mass) transfer distribution in the turn and downstream of the turn. In all cases studied, the average heat (mass) transfer was higher on the downstream half of the turn than on the upstream half of the turn.

3. In the smooth wall case, the heat (mass) transfer was high near the end wall and the downstream outer wall in the turn, and was relatively low in two regions near the upstream outer wall and the downstream edge of the divider wall in the turn.

4. With ribs on two opposite walls, the variation of the local heat (mass) transfer was larger than in the smooth wall case, especially in the turn and downstream of the turn. The regional average heat (mass) transfer was higher in the turn of the trapezoidal channel with a smaller inlet section

than in the turn of the channel with a larger inlet section. Immediately downstream of the turn, the regional average heat (mass) transfer in the larger exit section decreased abruptly, while the regional average heat (mass) transfer in the smaller exit section continued to increase and reached a maximum value before it decreased as the flow redeveloped. Immediately downstream of the turn, the regional average heat (mass) transfer was lower in the larger exit section of the channel with ribs than in the exit section of the channel with smooth walls for air flow in either direction.

5. The shape of the local heat (mass) transfer distribution at the turn was not significantly affected by varying the air mass flow rate. The average heat (mass) transfer enhancement in the turn was always higher when the Reynolds number was smaller.

6. The pressure drop across the turn was higher in the case of the flow entering the channel through the larger straight section than when the flow was reversed. As expected, the ribs increased the pressure drop across the turn.

The results of this study show that there is a large variation of the local heat (mass) transfer in the turn and immediately downstream of the turn for air flow through a two-pass trapezoidal channel with smooth walls or with ribs on the walls. The large variation is caused by a very complex flow field with secondary flows, separated and

reattached flows, and flow recirculation in the turn and near the ribs on the walls. To fully understand the effects of the geometries of the channel, the turn, and the ribs, or turbulence promoters, on the flow distribution in the channel, and the effect of the flow field on the local heat (mass) transfer distributions on the channel walls, parametric experimental and numerical studies must be continued to accurately measure or predict the flow fields near the turns in multi-pass channels of various geometries and the heat (mass) transfer distributions on the channel walls. These results are needed in the design of serpentine cooling passages in gas turbine airfoils.

4.2 THERMAL CHARACTERISTICS AND MECHANISMS OF A NOVEL HEAT PIPE

The thermal performance and mechanisms of a novel heat pipe, the QuTech[®] Heat Pipe, were characterized with an experimental apparatus and with chemical and thermal analysis instruments such as GC-MS, ICP-OES, XPS, XRD, and DSC, respectively. Results of the thermal performance were obtained at inclination angles of 90˚, 45˚, 0˚, -45˚, and -90˚, and compared with results of a conventional heat pipe, Noren[®], which is a closed two-phase copper-water thermosyphon. The results of the thermal performance and chemical/thermal analyses of the QuTech[®] Heat Pipe may be summarized as follows:

1. Maximum and minimum effective thermal conductivities were 70.4 and 8.3 times higher than the thermal conductivity of pure copper (391 *W/mK*) at 75.8W and 5W and at an angle between 90˚ and -90˚, respectively. The results show that gravity was one of the most important factors in determining the thermal performance of the QuTech® Heat Pipe.

2. Temperature distributions along the QuTech® Heat Pipe were quite similar with those of the conventional heat pipe that operates by phase change and utilizes latent heat of vaporization of water.

3. A similar phenomenon, with respect to the hysteresis or geyser effect of conventional heat pipes/thermosyphons that results from the "onset of nucleate boiling" was seen from the results of the QuTech® Heat Pipe. The heat pipe exhibited large variations in the average temperature differences, between the evaporator and the condenser seemed to occur, prior to experiencing failure. This variation was shifted to higher heat rates for the conventional heat pipe, Noren® (e.g., this was shown by Fig. 28).

4. Results of chemical analyses showed that QuTech® Heat Pipe contained water as working fluid and inorganic and organic components like sodium, potassium, phosphate, sulfur, and chromium, etc were present.

5. Results of thermal analyses showed that the interaction between the elements of the effluent and the solid compound might prevent absorption

of water into the solid compound. When thermal energy is applied to the solid compound through the outer surface of QTHP, vaporization of water due to the absorbed energy may occur more easily, since fewer water molecules are packed into the solid compound.

The results of this study show that the QuTech[®] Heat Pipe is operated by the same thermal mechanism as conventional heat pipes/thermosyphons. That is, phase change (vaporization of working fluid) and pressure difference between an evaporator and a condenser. Based on the results of chemical and thermal analyses, nevertheless, thermal performance of heat pipes/thermosyphons might increase with additional latent heat of fusion energy of salt hydrates and energy required to release water molecules from salt hydrates by the presence of inorganic salt hydrates in heat pipes/thermosyphons.

REFERENCES

1. Han, J.C., Dutta, S., and Ekkad, S.V., 2000, *Gas Turbine Heat Transfer and Cooling Technology*, Taylor and Francis, New York, NY, pp. 287-370 and pp. 439-497.

2. Burggraf, F., 1970, "Experimental Heat Transfer and Pressure Drop with Two Dimensional Turbulence Promoters Applied to Two Opposite Walls of a Square Tube," *Augmentation of Convective Heat and Mass Transfer*, A.E. Bergles and R.L. Webb, eds., ASME, New York, NY, pp. 70-79.

3. Han, J.C., Glicksman, L.R., and Rohsenow, W.M., 1978, "An Investigation of Heat Transfer and Friction for Rib Roughened Surfaces," Int. J. Heat and Mass Transfer **21**, pp. 1143-1156.

4. Boyle, R.J., 1984, "Heat Transfer in Serpentine Passages with Turbulence Promoters," ASME Paper No. 84-HT-24.

5. Han, J.C., Chandra, P.R., and Lau, S.C., 1988, "Local Heat/Mass Transfer Distributions around Sharp 180 Turns in Two-Pass Smooth and Rib-Roughened Channels," ASME J. Heat Transfer **110**, pp. 91-98.

6. Lau, S.C., Kukreja, R.T., and McMillin, R.D., 1991, "Effects of V-Shaped Rib Arrays on Turbulent Heat Transfer and Friction of Fully Developed Flow in a Square Channel," Int. J. Heat and Mass Transfer **34**, pp. 1605-1616.

7. Acharya, S., Dutta, S., Myrum, T.A., and Baker, R.S., 1993, "Periodically Developed Flow and Heat Transfer in a Ribbed Duct," Int. J. Heat and Mass Transfer **36**, pp. 2069-2082.

8. Ekkad, S.V. and Han, J.C., 1997, "Detail Heat Transfer Distributions in Two-Pass Square Channels with Rib Turbulators," Int. J. Heat and Mass Transfer **40**, pp. 2525-2537.

9. Rhee, D.H., Lee, D.H., Cho, H.H., and Moon, H.K., 2003, "Effects of Duct Aspect Ratios on Heat/Mass Transfer with Discrete V-Shaped Ribs," ASME Paper No. GT2003-38622.

10. Johnson, B.V., Wagner, J.H., Steuber, G.D., and Yeh, F.C., 1994, "Heat Transfer in Rotating Serpentine Passages with Trips Skewed to the Flow," ASME J. Turbomachinery **116**, pp. 113-123.

11. Johnson, B.V., Wagner, J.H., Steuber, G.D., and Yeh, F.C., 1994, "Heat Transfer in Rotating Serpentine Passages with Selected Model Orientations for Smooth or Skewed Trip Walls," ASME J. Turbomachinery **116**, pp. 738-744.

12. Park, C.W. and Lau, S.C., 1998, "Effect of Channel Orientation on Local Heat (Mass) Transfer Distributions in a Rotating Two-Pass Square Channel with Smooth Walls," ASME J. Heat Transfer **120**, pp. 624-632.

13. Park, C.W., Yoon, C., and Lau, S.C., 2000, "Local Heat (Mass) Transfer in a Diagonally-Oriented Rotating Two-Pass Channel with Rib-Roughened Walls," ASME J. Heat Transfer **122**, pp. 208-211.

14. Lee, E., Wright, L.M., and Han, J.C., 2003, "Heat Transfer in Rotating Rectangular Channel (AR = 4:1) with V-Shaped and Angled Rib Turbulators with and without Gaps," ASME Paper No. GT2003-38900.

15. Cho, H.H., Kim, Y.Y., Kim, K.M., and Rhee, D.H., 2003, "Effects of Rib Arrangements and Rotation Speed on Heat Transfer in a Two-Pass Duct," ASME Paper No. GT2003-38609.

16. Liu, Y.H., Wright, L.M. Fu, W.L., and Han, J.C., 2006, "Rib Spacing Effect on Heat Transfer and Pressure Loss in a Rotating Two-Pass Rectangular Channel (AR=1:2) with 45-Degree Angled Ribs," ASME Paper No. GT2006-90368.

17. Zhou, F. and Acharya, S., 2006, "Heat Transfer at High Rotation Numbers in a Two-Pass 4:1 Aspect Ratio Rectangular Channel with 45-Degree Skewed Ribs," ASME Paper No, GT2006-90391.

18. Ekkad, S.V., Huang, Y., and Han, J.C., 1996, "Detailed Heat Transfer Distributions in Two-Pass Smooth and Turbulated Square Channels with Bleed Holes," *presented at the 1996 National Heat Transfer Conference*, Houston, Texas, pp. 133-140.

19. Taslim, M.E., Li, T., and Spring, S.D., 1995, "Experimental Study of the Effects of Bleed Holes on Heat Transfer and Pressure Drop in Trapezoidal Passages with Tapered Turbulators," ASME J. Turbomachinery **117**, pp. 281-289.

20. Taslim, M.E., Li, T., and Spring, S.D., 1998, "Measurements of Heat Transfer Coefficients and Friction Factors in Passages Rib-Roughened on All Walls," ASME J. Turbomachinery **120**, pp. 564-570.

21. Li, L., Ding, S.T., Xu, G.Q., Tao, Z., and Deng, H.W., 2006, "Experimental Study on the Heat Transfer in the Compound Cooling Passage," ASME Paper No. GT2006-90250.

22. Moon, S.W., Endley, S., and Lau, S.C., 2002, "Local Heat Transfer Distribution in a Two-Pass Trapezoidal Channel with a 180° Turn via the Transient Liquid Crystal Technique," J. Energy, Heat and Mass Transfer **24**, pp. 103-121.

23. Perkins, L.P. and Buck, W.E., 1892, "Improvements in Devices for the Diffusion or Transference of Heat," U.K. Patent 22,272, London, England.

24. Gay, F.W., 1929, "Heat Transfer Means," U.S. Patent 1,725,906.

25. Gaugler, R.S., 1944, "Heat Transfer Devices," U.S. Patent 2,350,348.

26. Grover, G.M., Cotter, T.P., and Erikson, G.F., 1964, "Structures of Very High Thermal Conductivity," Journal of Applied Physics **35**, pp. 1190-1191.

27. Peterson, G.P., 1994, *An Introduction to Heat Pipes Modeling, Testing, and Applications*, John Wiley and Sons, New York, NY, pp.1-17.

28. Dobran, F., 1989, "Heat Pipe Research and Development in The Americas," Heat Recovery Systems & CHP **9**, No. 1, pp. 67-100.

29. Reid, R.S. and Merrigan, M.A., *Heat Pipe Activity in the Americas – 1990 to 1995*, Los Alamos National Laboratory, Los Alamos, NM.

30. Eastman, G.Y, 1968, "The Heat Pipe," Scientific American **218**, No. 12, pp.38-46.

31. Palm, B. and Tengblad, N., 1996, "Cooling of Electronics by Heat Pipes and Thermosyphons – A Review of Methods and Possibilities," HTD-Vol. 329 National Heat Transfer Conference, Vol. 7, pp. 97-108.

32. Hahne, E. and Gross, U., 1981, "The Influence of the Inclination Angle on the Performance of a Closed Two-Phase Thermosyphon," Heat Recovery Systems **1**, pp. 267-274.

33. Gurses, A.C., Cannistraro, C., and Tezcan, L., 1991, "The Inclination Effect on the Performance of Water-Filled Heat Pipes," Renewable Energy **1**, No. 5/6, pp. 667-674.

34. Bilegan, I.C. and Fetcu, D., 1982, "Performance Characteristics of Gravity-Assisted Aluminum Extruded Heat Pipes," Heat Recovery Systems **2**, No. 2, pp. 159-163.

35. Park, Y,J., Kang, H.K., and Kim, C.J., 2002, "Heat Transfer Characteristics of a Two-Phase Closed Thermosyphon to the Fill Charge Ratio," Int. J. Heat and Mass Transfer **45**, pp. 4655-4661.

36. Noie, S.H., 2005, "Heat Transfer Characteristics of a Two-Phase Closed Thermosyphon," Applied Thermal Engineering **25**, pp. 495-506.

37. El-Genk, M.S. and Saber, H.H., 1999, "Determination of Operation Envelopes for Closed, Two-Phase Thermosyphons," Int. J. Heat and Mass Transfer **42**, pp. 889-903.

38. Qu, Y., 2000, "Superconducting Heat Transfer Medium," U.S. Patent 6,132,823.

39. Ambrose, D., Lawrenson, I.J., and Sprake, C.H.S., 1975, "The Vapor Pressure of Naphthalene," J. Chemical Thermodynamics **7**, pp. 1172-1176.

40. Goldstein, R.J. and Cho, H.H., 1995, "A Review of Mass Transfer Measurements Using Naphthalene Sublimation," Experimental Thermal and Fluid Science **10**, pp. 416-434.

41. Eckert, E.R.G., 1976, "Analogies to Heat Transfer Processes," *Measurements in Heat Transfer*, E.R.G. Eckert and R.J. Goldstein, eds., Hemisphere Publishing Corp., New York, NY, pp. 397-423.

42. Incropera, F.P. and DeWitt, D.P., 2002, *Fundamentals of Heat and Mass Transfer*, 5th ed., John Wiley & Sons, New York, NY.

43. Coleman, H.W. and Steele, W.G., 1989, *Experimentation and Uncertainty Analysis for Engineers*, John Wiley & Sons, New York, NY.

44. Ong, K.S. and Haider-E-Alalhi, Md., 1999, "Experimental Investigation on the Hysteresis Effect in Vertical Two-phase Closed Thermosyphons," Applied Thermal Engineering **19**, pp. 399-408.

45. Li, H., Akabarzadeh, A., and Johnson, P., 1991, "The Thermal Characteristics of a Closed Two-phase Thermosyphon at Low Temperature Difference," *Heat Recovery Systems & CHP* **11**, pp. 533-540.

46. Hohne, G.W.H., Hemminger, W.F., and Flammersheim, H.-J., 2003, *Differential Scanning Calorimetry*, 2nd ed., Springer, New York, NY.

47. Sharma, S.D., and Sagara, K., 2005, "Latent Heat Storage Materials and Systems: A Review," *Int. J. Green Energy* **2**, pp. 1-56.

48. Abhat, A., 1983, "Low Temperature Latent Heat Thermal Energy Storage: Heat Storage Materials," *Solar Energy* **30**, pp. 313-332.

49. Mu, J. and Perimutter, D.D., 1981, "Thermal Decomposition of Inorganic Sulfates and Their Hydrates, Ind. Eng. Chem. Process Des. Dev. **20**, pp. 640-646.

50. Ghule, A., Murugan, R., and Chang, H., 2001, "Thermo-Raman Studies on Dehydration of $Na_3PO_4 \cdot 12H_2O$," Thermochimica Acta **371**, pp. 127-135

51. Ghule, A., Bhongale, C., and Chang, H., 2003, "Monitoring dehydration and Condensation Processes of $Na_2HPO_4 \cdot 12H_2O$ Using Thermo-Raman Spectroscopy," Spectrochimica Acta Part A **59**, pp. 1529-1539.

52. Lide, D.R., 2006, *CRC Handbook of Chemistry and Physics*, CRC Press, LLC, Boca Raton, FL, pp. section 4-43–section 4-101

53. Sharma, S.K., Jotshi, C.K., and Kumar, S., 1990, "Thermal Stability of Sodium Salt Hydrates for Solar Energy Storage Applications," Solar Energy **45**, pp. 177-181

54. Sharma, S.K., Jotshi, C.K., and Kumar, S., 1991, "Kinetics of Dehydration of Sodium Salt Hydrates," Thermochimica Acta **184**, pp. 9-23.

APPENDIX A

MATLAB Codes to Reduce Raw Data for Local Mass Transfer Experiments

MATLAB Code 1 - Raw Data Converter

```
clear;
clc;
%%%%%%%%%%%%%%%%%%%%%%%%%%%%%%%%%%%%%%%%%%%%%%%%%%%%%%%%%%%%%%%%%%%%%%%%%
% Raw Data Aquisition from text files generated by LABVIEW
%%% 1st text file aquisition-Before a Run for a Main Experiment
[FileNameA,PathNameA]=uigetfile('*.txt','Enter filename of 1st-
MEASUREMENT to read');
[FileIdA]=fopen(FileNameA,'rt');
[RDataA EA]=fscanf(FileIdA,'%e %e %e',[3,inf]);
TRDataA=RDataA';
IdA=input('Name of 1st output sheet: ','s');
%%% 2nd text file aquisition-After a Run for a Main Experiment
[FileNameB,PathNameB]=uigetfile('*.txt','Enter filename of 2nd-
MEASUREMENT to read');
[FileIdB]=fopen(FileNameB,'rt');
[RDataB EB]=fscanf(FileIdB,'%e %e %e',[3,inf]);
TRDataB=RDataB';
IdB=input('Name of 2nd output sheet: ','s');
%%%%%%%%%%%%%%%%%%%%%%%%%%%%%%%%%%%%%%%%%%%%%%%%%%%%%%%%%%%%%%%%%%%%%%%%%
% Converting of Raw Data File into Formatted EXCEL File
N=[82 22; 21 8; 82 22]; % N # and Dimension of Part 1, 2, and 3
SN=sum(N);
dx=0.0746;
dy=0.075;
for i=2:N(1,1)+1; % x location from #0 to #81 of DAQ
    DataA(1,i)=(i-5/2)*dx; % x= -0.0373" ~ 6.0053"
    DataB(1,i)=(i-5/2)*dx;
end;
m=0;
n=0;
y=-0.1115;
for i=1:3;
    if i~=1; n=N(i-1,1)*N(i-1,2)+n; end;
    for j=2:N(i,2)+1;
        y=y+dy;
        DataA(j+m,1)=y;
        DataB(j+m,1)=y;
        tMxA=transpose(TRDataA(1+(j-2)*N(i,1)+n:(j-1)*N(i,1)+n,3));
        tMxB=transpose(TRDataB(1+(j-2)*N(i,1)+n:(j-1)*N(i,1)+n,3));
        if mod(j,2)~=0;
            DataA(j+m,2:N(i,1)+1)=fliplr(tMxA);
            DataB(j+m,2:N(i,1)+1)=fliplr(tMxB);
        else
            DataA(j+m,2:N(i,1)+1)=tMxA;
            DataB(j+m,2:N(i,1)+1)=tMxB;
        end
    end;
    m=N(i,2)+m;
end;
tA=DataA(2:SN(2)+1,1);
DataA(2:SN(2)+1,1)=flipud(tA);
```

```
tB=DataB(2:SN(2)+1,1);
DataB(2:SN(2)+1,1)=flipud(tB);
xlswrite('D:\----\Raw Data 1', DataA, IdA);
xlswrite('D:\----\Raw Data 1', DataB, IdB);
```

MATLAB Code 2 – Height Correctioner

```matlab
clear;
clc;
%%%%%%%%%%%%%%%%%%%%%%%%%%%%%%%%%%%%%%%%%%%%%%%%%%%%%%%%%%%%%%%%%%%%%%%%%
% Raw Data Aquisition from text files generated by LABVIEW
[type, sheets] = xlsfinfo('Correction of Data 2')
A=input('1st sheet to read: ','s');
DA=xlsread('Correction of Data 2',A);
B=input('2nd sheet to read: ','s');
DB=xlsread('Correction of Data 2',B);
%%%%%%%%%%%%%%%%%%%%%%%%%%%%%%%%%%%%%%%%%%%%%%%%%%%%%%%%%%%%%%%%%%%%%%%%%
% Correction of Measured Heights with Heights of Rims using Least
% Square Curve Fitting
N=[82 22; 21 8; 82 22]; % Node # and Dimension of Part 1, 2, and 3
SN=sum(N);
pA1=polyfit(DA(1,2:N(1,1)),DA(2,2:N(1,1)),1); % Curve fitting of 1st
rim of DataA except the last point of #81 of DAQ
pA2=polyfit(DA(1,23:N(1,1)),DA(23,23:N(1,1)),1); % Curve fitting of 2nd
rim of DataA except the last point of #81 of DAQ
pA3=polyfit(DA(1,23:N(1,1)),DA(32,23:N(1,1)),1); % Curve fitting of 3rd
rim of DataA except the last point of #81 of DAQ
pA4=polyfit(DA(1,2:N(1,1)),DA(SN(2)+1,2:N(1,1)),1); % Curve fitting of
4th rim of DataA
pB1=polyfit(DB(1,2:N(1,1)),DB(2,2:N(1,1)),1);
pB2=polyfit(DB(1,23:N(1,1)),DB(23,23:N(1,1)),1);
pB3=polyfit(DB(1,23:N(1,1)),DB(32,23:N(1,1)),1);
pB4=polyfit(DB(1,2:N(1,1)),DB(SN(2)+1,2:N(1,1)),1);
pvA1=polyval(pA1,DA(1,3:N(1,1))); % Curve Fitted Values obtained on
Nodes of 1st Rim of DataA
pvA2=polyval(pA2,DA(1,3:N(1,1))); % Curve Fitted Values obtained on
Nodes of 2nd Rim of DataA
pvA3=polyval(pA3,DA(1,3:N(1,1))); % Curve Fitted Values obtained on
Nodes of 3rd Rim of DataA
pvA4=polyval(pA4,DA(1,3:N(1,1))); % Curve Fitted Values obtained on
Nodes of 4th Rim of DataA
pvB1=polyval(pB1,DB(1,3:N(1,1)));
pvB2=polyval(pB2,DB(1,3:N(1,1)));
pvB3=polyval(pB3,DB(1,3:N(1,1)));
pvB4=polyval(pB4,DB(1,3:N(1,1)));
pvBA1=pvB1-pvA1; % Difference of Curve Fitted Values of 1st Rims
between DataA and DataB
pvBA2=pvB2-pvA2;
pvBA3=pvB3-pvA3;
pvBA4=pvB4-pvA4;
pvBA14=pvBA1-pvBA4; % Difference of Curve Fitted Values between
Difference of Values of 1st Rims between DataA and DataB and Difference
of Values of 4th Rims between DataA and DataB
pvBA12=pvBA1-pvBA2;
pvBA34=pvBA3-pvBA4;
IpvBA(1:SN(2)+1,1:N(1,1)+1)=0;
for i=3:22;
```

```
    IpvBA(3:SN(2),i)=pvBA4(i-2)+pvBA14(i-2)*(DA(3:SN(2),1)-
DA(SN(2)+1,1))/(DA(2,1)-DA(SN(2)+1,1)); % Interpolation for Data with
the obtained Difference of Values of Rims between DataA and DataB
end;
for i=23:82;
    IpvBA(3:22,i)=pvBA2(i-2)+pvBA12(i-2)*(DA(3:22,1)-
DA(23,1))/(DA(2,1)-DA(23,1));
    IpvBA(33:52,i)=pvBA4(i-2)+pvBA34(i-2)*(DA(33:52,1)-
DA(53,1))/(DA(32,1)-DA(53,1));
end;
DAB=(DA-(DB-IpvBA));
FDAB(2:SN(2)-1,1)=DA(3:SN(2),1);
FDAB(1,2:N(1,1)-1)=DA(1,3:N(1,1));
FDAB(2:SN(2)-1,2:N(1,1)-1)=DAB(3:SN(2),3:N(1,1));
FDAB(22:31,22:N(1,1)-1)=0;
xlswrite('D:\----\Height Data 3', FDAB, A);
```

MATLAB Code 3 - Data Reducer

```matlab
clear;
clc;
% Data Reduction to Heat Transfer Coefficient
% Corrected Data Aquisition from EXCEL files generated by LABVIEW
[type, sheets] = xlsfinfo('Corrected Height Data 4')
D=input('1st sheet to read: ','s');
DD=xlsread('Corrected Height Data 4',D);
Height=DD*0.0254;
[type, sheets] = xlsfinfo('Local Measurement of U-turn Channel, Spring
2005')
fId=input('Flow Info to read: ','s');
fd=xlsread('Local Measurement of U-turn Channel, Spring
2005',fId,'B24:K25');
tC=fd(1,1); % running time with Correction
tnC=fd(2,1); % running time without Correction
ImassC=fd(1,2); % Upstream Mass Transfer Amount of #5 by Correction
ImassnC=fd(2,2); % Upstream Mass Transfer Amount of #5 by Calculation
W1=fd(1,3);
W2=fd(1,4);
W3C=fd(1,5); % Measured Mass after Correction Test
W3nC=fd(2,5); % Calculated Mass without Correction Test
Wd=fd(1,6); % wall density of naphthalene
Q=fd(1,7); % flow rate
Sigma=fd(1,8);
Sh0=fd(1,9);
Dh=fd(1,10);
Sd=1175; % solid density of naphthalene [kg/m3]
N=[82 22; 21 8; 82 22]; % N # and Dimension of Part 1, 2, and 3
dx=0.0746;
dy=0.0750;
SN=sum(N);
s=input('Enter 1 for LT or SQ case without ribs, 2 for ST case without
ribs, 3 for ST case with ribs, and 4 for LT case with ribs: ');

% Calculation of Area of Mesh
% Area without Ribs
Area(2:51,2:81)=dx*dy*0.0254^2;
Area(22:30,21)=(dx/2+0.0153)*dy*0.0254^2;
Area(31,21)=(dx/2+0.0153)*(dy/2+0.0385)*0.0254^2;
Area(31,2:20)=dx*(dy/2+0.0385)*0.0254^2;
Area(32,2:81)=dx*(dy/2+0.0365)*0.0254^2;
Area(51,2:81)=dx*(dy/2+0.0385)*0.0254^2;
Area(22:31,22:81)=0;

% Area with Virtual Segment Line
Area(2:21,62)=Area(2:21,62)-0.0120*dy*0.0254^2;
Area(2:21,61)=Area(2:21,61)+0.0120*dy*0.0254^2;
Area(32,61)=Area(32,61)+0.0120*(dy/2+0.0365)*0.0254^2;
Area(32,62)=Area(32,62)-0.0120*(dy/2+0.0365)*0.0254^2;
Area(33:50,61)=Area(33:50,61)+0.0120*dy*0.0254^2;
Area(33:50,62)=Area(33:50,62)-0.0120*dy*0.0254^2;
```

```matlab
Area(51,61)=Area(51,61)+0.0120*(dy/2+0.0385)*0.0254^2;
Area(51,62)=Area(51,62)-0.0120*(dy/2+0.0385)*0.0254^2;


Area(2:21,41)=Area(2:21,41)-0.0050*dy*0.0254^2;
Area(2:21,42)=Area(2:21,42)+0.0050*dy*0.0254^2;
Area(32,41)=Area(32,41)-0.0050*(dy/2+0.0365)*0.0254^2;
Area(32,42)=Area(32,42)+0.0050*(dy/2+0.0365)*0.0254^2;
Area(33:50,41)=Area(33:50,41)-0.0050*dy*0.0254^2;
Area(33:50,42)=Area(33:50,42)+0.0050*dy*0.0254^2;
Area(51,41)=Area(51,41)-0.0050*(dy/2+0.0385)*0.0254^2;
Area(51,42)=Area(51,42)+0.0050*(dy/2+0.0385)*0.0254^2;


Area(2:21,21)=Area(2:21,21)-0.0220*dy*0.0254^2;
Area(2:21,22)=Area(2:21,22)+0.0220*dy*0.0254^2;
Area(32,21)=Area(32,21)-0.0220*(dy/2+0.0365)*0.0254^2;
Area(32,22)=Area(32,22)+0.0220*(dy/2+0.0365)*0.0254^2;
Area(33:50,21)=Area(33:50,21)-0.0220*dy*0.0254^2;
Area(33:50,22)=Area(33:50,22)+0.0220*dy*0.0254^2;
Area(51,21)=Area(51,21)-0.0220*(dy/2+0.0385)*0.0254^2;
Area(51,22)=Area(51,22)+0.0220*(dy/2+0.0385)*0.0254^2;

% Area with Ribs
if s==3;
    % 1st Rib
    Area(2:21,80:81)=0;
    Area(2:21,79)=Area(2:21,79)+0.0242*dy*0.0254^2;
    % 2nd Rib
    Area(2:21,60:61)=0;
    Area(2:21,59)=Area(2:21,59)+0.0362*dy*0.0254^2;
    % 3rd Rib
    Area(2:21,40:41)=0;
    Area(2:21,39)=Area(2:21,39)+0.0192*dy*0.0254^2;
    % 4th Rib
    Area(2:21,20:21)=0;
    % 5th Rib
    Area(27:28,2:21)=0;
    Area(29,2:20)=Area(29,2:20)+dx*0.0250*0.0254^2;
    Area(29,21)=Area(29,21)+(dx/2+0.0153)*0.0250*0.0254^2;
    % 6th Rib
    Area(32:51,22:23)=0;
    Area(33:50,24)=Area(33:50,24)+dx/2*dy*0.0254^2;
    Area(32,24)=Area(32,24)+dx/2*(dy/2+0.0365)*0.0254^2;
    Area(51,24)=Area(51,24)+dx/2*(dy/2+0.0385)*0.0254^2;
    % 7th Rib
    Area(32:51,42:43)=0;
    Area(33:50,44)=Area(33:50,44)+0.0292*dy*0.0254^2;
    Area(32,44)=Area(32,44)+0.0292*(dy/2+0.0365)*0.0254^2;
    Area(51,44)=Area(51,44)+0.0292*(dy/2+0.0385)*0.0254^2;
    % 8th Rib
    Area(32:51,62:63)=0;
    Area(33:50,64)=Area(33:50,64)+0.0122*dy*0.0254^2;
    Area(32,64)=Area(32,64)+0.0122*(dy/2+0.0365)*0.0254^2;
    Area(51,64)=Area(51,64)+0.0122*(dy/2+0.0385)*0.0254^2;
```

```matlab
elseif s==4;
    % 1st Rib
    Area(32:51,80:81)=0;
    Area(33:50,79)=Area(33:50,79)+0.0242*dy*0.0254^2;
    Area(32,79)=Area(32,79)+0.0242*(dy/2+0.0365)*0.0254^2;
    Area(51,79)=Area(51,79)+0.0242*(dy/2+0.0385)*0.0254^2;
    % 2nd Rib
    Area(32:51,60:61)=0;
    Area(33:50,59)=Area(33:50,59)+0.0362*dy*0.0254^2;
    Area(32,59)=Area(32,59)+0.0362*(dy/2+0.0365)*0.0254^2;
    Area(51,59)=Area(51,59)+0.0362*(dy/2+0.0385)*0.0254^2;
    % 3rd Rib
    Area(32:51,40:41)=0;
    Area(33:50,39)=Area(33:50,39)+0.0192*dy*0.0254^2;
    Area(32,39)=Area(32,39)+0.0192*(dy/2+0.0365)*0.0254^2;
    Area(51,39)=Area(51,39)+0.0192*(dy/2+0.0385)*0.0254^2;
    % 4th Rib
    Area(32:51,20:21)=0;
    % 5th Rib
    Area(25:26,2:21)=0;
    Area(24,2:20)=Area(24,2:20)+dx*0.0250*0.0254^2;
    Area(24,21)=Area(24,21)+(dx/2+0.0153)*0.0250*0.0254^2;
    % 6th Rib
    Area(2:21,22:23)=0;
    Area(2:21,24)=Area(2:21,24)+dx/2*dy*0.0254^2;
    % 7th Rib
    Area(2:21,42:43)=0;
    Area(2:21,44)=Area(2:21,44)+0.0292*dy*0.0254^2;
    % 8th Rib
    Area(2:21,62:63)=0;
    Area(2:21,64)=Area(2:21,64)+0.0122*dy*0.0254^2;
end;

% Checking and Correction of Height
dM1=Sd*sum(sum(Height.*Area));
dW1=W1-W2;
Error=abs(dM1-dW1)/dW1*100;
if tC==tnC; % without Correction Test
    t=tnC;
    Imass=ImassnC;
    W3=W3nC;
else; % with Correction Test
    t=tC;
    Imass=ImassC;
    W3=W3C;
end;
dW2=W2-W3;
cHeight=Height-dW2/sum(sum(Area))/Sd;
switch s;
    case {1,4};
        % Calculation of Bulk Density of Naphthalene
        Bd(1:51,1:81)=0;
        for i=2:21;
            Bd(i,81)=(Imass/20+Sd*cHeight(i,81)*Area(i,81)/t/2)/Q;
```

```matlab
        end;
        for i=80:-1:22;
            for j=2:21;

Bd(j,i)=Bd(j,i+1)+Sd*(cHeight(j,i+1)*Area(j,i+1)+cHeight(j,i)*Area(j,i)
)/t/Q/2;
            end;
        end;
        M=Sd*cHeight.*Area./t/Q/2;
        Bd(2:26,2:21)=mean(Bd(2:21,22))+mean2(M(2:26,2:21));
        Bd(27:51,2:21)=mean2(Bd(2:26,2:21))+mean2(M(27:51,2:21));
        for i=22:81;
            for j=32:51;
                Bd(j,i)=Bd(j,i-1)+Sd*cHeight(j,i)*Area(j,i)/t/Q/2;
            end;
        end;
    case {2,3};
        % Calculation of Bulk Density of Naphthalene
        Bd(1:51,1:81)=0;
        for i=32:51;
            Bd(i,81)=(Imass/20+Sd*cHeight(i,81)*Area(i,81)/t/2)/Q;
        end;
        for i=80:-1:22;
            for j=32:51;

Bd(j,i)=Bd(j,i+1)+Sd*(cHeight(j,i+1)*Area(j,i+1)+cHeight(j,i)*Area(j,i)
)/t/Q/2;
            end;
        end;
        M=Sd*cHeight.*Area./t/Q/2;
        Bd(27:51,2:21)=mean(Bd(32:51,22))+mean2(M(27:51,2:21));
        Bd(2:26,2:21)=mean2(Bd(27:51,2:21))+mean2(M(2:26,2:21));
        for i=22:81;
            for j=2:21;
                Bd(j,i)=Bd(j,i-1)+Sd*cHeight(j,i)*Area(j,i)/t/Q/2;
            end;
        end;
end;
% Calculation of Local Heat Transfer Coefficients
Pck0=cHeight.*Area;
for j=2:81;
    for i=2:51;
        if Pck0(i,j)==0;
            cHeight(i,j)=Pck0(i,j);
        end;
    end;
end;
loh=Sd*cHeight./(Wd-Bd)./t;
loh(1,:)=Height(1,:);
loh(:,1)=Height(:,1);
loSh=loh.*Dh/Sigma;
loSh(1,:)=Height(1,:);
loSh(:,1)=Height(:,1);
loP=loSh./Sh0;
```

```matlab
loP(1,:)=Height(1,:);
loP(:,1)=Height(:,1);
loPm(1:21,:)=loP(1:21,:); % Converting Single-Zone Data Format into
Multi-Zone Data Format
loPm(23,1:21)=loP(1,1:21);
loPm(24:35,1:21)=loP(21:32,1:21);
loPm(37,:)=loP(1,:);
loPm(38:57,:)=loP(32:51,:);
% Calculation of Total Averaged Heat Transfer Coefficients
aveh(1)=sum(sum(loh(2:51,2:81).*Area(2:51,2:81)))/sum(sum(Area(2:51,2:8
1)));
% Calculation of Regional Averaged Heat Transfer Coefficients
aveh(2)=sum(sum(loh(2:21,62:81).*Area(2:21,62:81)))/sum(sum(Area(2:21,6
2:81)));
aveh(3)=sum(sum(loh(2:21,42:61).*Area(2:21,42:61)))/sum(sum(Area(2:21,4
2:61)));
aveh(4)=sum(sum(loh(2:21,22:41).*Area(2:21,22:41)))/sum(sum(Area(2:21,2
2:41)));
aveh(5)=sum(sum(loh(2:26,2:21).*Area(2:26,2:21)))/sum(sum(Area(2:26,2:2
1)));
aveh(6)=sum(sum(loh(27:51,2:21).*Area(27:51,2:21)))/sum(sum(Area(27:51,
2:21)));
aveh(7)=sum(sum(loh(32:51,22:41).*Area(32:51,22:41)))/sum(sum(Area(32:5
1,22:41)));
aveh(8)=sum(sum(loh(32:51,42:61).*Area(32:51,42:61)))/sum(sum(Area(32:5
1,42:61)));
aveh(9)=sum(sum(loh(32:51,62:81).*Area(32:51,62:81)))/sum(sum(Area(32:5
1,62:81)));
aveP=aveh.*Dh/Sigma/Sh0;
%%%%%%%%%%%%%%%%%%%%%%%%%%%%%%%%%%%%%%%%%%%%%%%%%%%%%%%%%%%%%%%%%%%%%%%%%
value={'Total' '5' '6' '7' '8' '9' '10' '11' '12' 'Error' 'Measured'
'Weighed' 'Time' 'Dh'; aveP(1) aveP(2) aveP(3) aveP(4) aveP(5) aveP(6)
aveP(7) aveP(8) aveP(9) Error dM1 dW1 t Dh};
xlswrite('D:\----\LocalValues', loPm, D);
xlswrite('D:\----\AverageValues', value', D);
```

VITA

Sang Won Lee received his B.En., in mechanical engineering from Inha University, Incheon, Korea, in February 1998. He worked for Hyundai Space and Aircraft Co. (currently Korea Aerospace Industries, Ltd.) from January 1998 to January 1999. He received his M.S. in mechanical engineering from Texas A&M University, College Station, TX, in December 2002. He attended the Ph.D. program from January 2003 to August 2007 in the Department of Mechanical Engineering at Texas A&M University where he received a Ph.D. degree in mechanical engineering.

His permanent address is:

> 603-901 BYUKSAN BLOOMING APT
>
> ILSANSEO-GU KOYANG
>
> KYUNGKI-DO, 411-440
>
> REPUBLIC OF KOREA